Study of magnetoelectronic devices based on Co-HfO_2 granular films

By

Shyamsunder Regunathan

M.Sc (IT), Multimedia University, Malaysia

B.E, University of Madras, India

A Thesis submitted for the degree of

Doctor of Philosophy

Department of Electrical and Computer Engineering

National University of Singapore

Singapore

2012

Acknowledgment

I would like to thank my whole family in India for all their support, faith and guidance during my stay abroad all these years.

I would like to show my gratitude to my supervisor, Assoc. Prof. Vivian Ng for giving me the chance to work on this research topic. Her patience, support and guidance in both research and personal aspects of my work have made this journey a memorable one.

I would also like to thank Assoc. Prof. Adekunle Adeyeye, Assoc. Prof. Teo Kie Leong and Prof. Wu Yihong for the support in terms of using their equipments whenever we requested for the same. I extend my thanks to Prof. Roy Chantrell (from University of York) for his ideas and lively discussions. His humility, energy and thought processes are quite inspiring.

My friends have also been a major support for me and I am grateful to them. I would like to express my gratitude to all the ISML staff and students. I would like to especially mention Dr. Shika Jain and Dr. Naganivetha Thiyagarajah, as both of them had to bear with me for all these years and listen to my ranting about equipment and my life going in all directions in my research.

A special acknowledgment to my cousins and little nieces in Singapore, who made me realize that research is a part of life and never greater than life itself.

Dedication

To the lotus feet of the Lord...

Contents

Summary

Granular films are useful because of ease of preparation as well potential applications in sensors and storage media. The grain sizes in granular films are dependent on the volume fraction and thickness of the ferromagnetic material used. Other than magnetoresistance (MR), these films show interesting properties such as Coulomb Blockade. In this thesis, two device structure for Co-HfO_2 granular films have been implemented and discussed.

The first structure consists of inserting the HfO_2 in between a granular film having 20 bilayers of Co-HfO_2. The thickness of insert was varied from 1.5 nm to 15 nm and initially the current in plane properties (CIP) are studied. The purpose of this structure was to obtain better grain size control using roughness as well as to understand the effect of parallel paths on the MR in CIP conduction.The structure with the 1.5 nm of HfO_2 insert had grain sizes with largest spread induced by the roughness of the insert. It showed Coulomb Blockade characteristic at 10.6 K accompanied by anomalous increase in MR. As the thickness was increased beyond 5nm, the inserted films were observed to be continuous helping to form larger grains in the top of the structure. For these structures, the major conduction was through the top granular film. The samples with 5 nm and 1.5 nm insert gave improved MR at temperatures above and below 15 K respectively .

A simulation model was developed for the above proposed CIP structure using Monte Carlo method where the physical grain sizes and locations were generated

using the experimental M-H loop. It was found that there was good agreement between the experimental and simulated MR curves.

Current perpendicular plane (CPP) devices based on oxide insert were also studied in thesis and compared with their CIP counterparts. The CPP devices showed decrease in MR as compared to CIP devices because of the high field induced tunneling effect. The CPP device based on granular film having 20 bilayers of Co-HfO_2 was least affected by the field induced tunneling. This indicated that higher thickness of granular film without the insert would reduce high field tunneling effect and improve MR in the case of CPP devices.

The second structure consisted of inserting NiFe soft magnetic layer in CPP granular film devices. The Py layer acted as flux enhancer and thus influenced the MR. The idea of the experiment was to counter the high field effect induced tunneling in CPP devices and improve MR. This single layer of NiFe was inserted in between the granular film and again the thickness was varied between 1.5 nm and 35 nm. Finite Elements Magnetic Modeling was used understand the magnetic flux distribution in such systems. It was found that MR improved with increasing thickness of Py layer as compared to 10 bilayer Co-HfO_2 film. The MR improvement was due to the field enhancement at the edges of the NiFe films.

List of Tables

List of Figures

List of Symbols

AMR Anisotropic Magnetoresistance

CB Coulomb Blockade

CIP Current in Plane

CPP Current perpendicular plane

FC Field Cooling

GMR Giant Magneto Resistance

MR Magnetoresistance

MTJ Magnetic Tunneling Junction

SAXS Small Angle X-ray Scattering

SDT Spin Dependent Tunneling

T_B Blocking temperature

TEM Transmission Electron microscopy

TMR Tunneling Magnetoresistance

ZFC Zero Field Cooling

Chapter 1

Introduction

Currently, we live in a digital era wherein the amount of information in terms of audio, video and other sensory information in digital form are of pure essence. This has driven the field of data storage and recording technology to come a long way with the help of scaling of devices. However as the device sizes approach atomic scales, it becomes difficult to implement the physical scaling. In order to help alleviate the problem, other natural degrees of freedom, such as spin have been explored. This was suggested by visionaries such as Feyman and Launder in the 1970's [1, 2]. The field of spintronics(spin electronics) has developed over the past few few decades. Since the discovery of giant magneto resistance (GMR) in Fe/Cr super lattices by Fert [3] and Grunberg [4] numerous researches have been conducted in the areas of large magneto resistance (MR) effects due to spin-dependent scattering [5] or spin-dependent tunneling in magnetic nanostructures [6, 7].

The concept of magnetoresistance (MR) is what makes these devices and films very useful for practical applications. This area of research is a combination of two branches of physics: magnetism and electronics. The whole idea of this approach is to manipulate the electron spin in transport processes. Charge based devices have already been implemented in systems such as the vacuum tube to transistor

technology in microchips. These devices rely on the movement of electric charges and do not make use of the extra degree of freedom namely electron spin, which is inherent to every electron. Under normal condition without application of magnetic field in an electric circuit, the spins are randomly oriented and have no effect on current flow. But in the presence of the magnetic field the spin-up and spin-down electrons, have different energies depending on their orientation with respect to the applied field. In today's world, the spin dependent electronics have played a major role in fabrication of the vastly used hard-drive magnetic discs and sensors.

Granular systems based on magnetic nano particles embedded in an immiscible insulating matrix have been an important part of research on magnetic films [8, 9]. The conduction in these systems is because of tunneling between magnetic grains. However, the tunneling between the grains is spin dependent. Based on the magnetic orientation of the grain, the resistance of tunneling can vary. Same orientation grains have higher probability and lower resistance and vice-versa. The advantages of granular film is that their magnetic particles can be tailored i.e. the coercivity and interactions in these grains are a function of grain size and this can be controlled by controlling the grain size [9, 10] .

The TMR effect in granular films finds application as a magnetic sensor in various fields such as read-heads of hard disk drives [9, 11, 12] and biosensors in diagnostic and therapeutic tools in life sciences [13]. They also find applications in high frequency RF (radio frequency) devices [14, 15] and Hall effect sensors [16]. The following section discusses the various kinds of MR effects.

1.1 Theory of Magnetoresistance(MR)

As mentioned earlier, the underlying concept behind spintronics devices is that of magnetoresistance (MR) which is change in resistance of any material in the

presence of a magnetic field [12] and is defined as

$$MR(H) = \frac{R(H) - R(0)}{R(0)} \times 100\% \tag{1.1}$$

where R(H) is the resistance of the material subject to a magnetic field H. Various researchers around the world are trying to improve this factor by changing materials, structures, deposition techniques etc. This effect constitutes the fundamental property studied in this thesis and can be classified as :

1. **Anisotropic Magnetoresistance (AMR)** - This phenomenon was discovered by Lord Kelvin in 1857 [12]. AMR is based on the fact that in the absence of a magnetic field, magnetization M would normally line up parallel to the easy axis of a FM material. When an external magnetic field H is applied, M rotates to an angle θ with respect to the easy axis, and the current flowing through will experience a change in resistivity as compared to without applying any external field. This change in resistivity depends on the angle θ between the current direction and the orientation of magnetization leading to AMR.

2. **Giant Magnetoresistance (GMR)** - The GMR effect is a property of multilayer structures consisting of alternate layers of magnetic and non-magnetic metallic materials which was discovered in the later 80's [3, 4]. In order to observe the GMR effect, there are two requirements : First, there must be a mechanism to change the relative orientation of magnetization in the adjacent magnetic layers and second, the spacer layer thickness should be less than the mean free path of the conduction electrons (~10 nm). The GMR effect relies much on the spin-dependent scattering mechanism which is more likely to occur when an electron of one spin encounters a layer having an opposite spin. Thus for an antiferromagnetically coupled multilayer, electrons of either

spin will encounter a series of strong and weak scattering as they drift along the electric field direction from one magnetic layer to the next, thus resulting in electrons of either spins having comparable mean free paths and resistivity. As for a ferromagnetically coupled multilayer structure, electrons having the same spin direction as that of the magnetic layers will encounter a series of weak-scattering in the parallel-spin layers. Their resistivity is smaller and mean free path is longer compared to electrons of opposite spin leading to the GMR effect [12].

3. **Tunneling Magnetoresistance (TMR)** - While GMR is due to spin-dependent scattering, TMR is the result of spin-dependent tunneling (SDT) which will be elaborately discussed in the next section. TMR is observed in Magnetic Tunnel Junctions and granular films.

    - *Magnetic Tunnel Junction (MTJ)* - The MTJ, which comprises of a sandwich of two ferromagnetic (FM) layers separated by a thin insulating layer, acting as a tunnel barrier was suggested in 1975 by Julliere [17]. The electrons tunnel through the insulating layer and hence exhibit the TMR Effect. It was shown that current flow across the insulating material was dependent on the relative orientation of the magnetization of the two FM layers. When their magnetization are in anti-parallel configuration, the resistance across the junction is high and tunneling did not occur. However, when an external magnetic field is applied, the magnetic domains of the two electrodes become parallel and results in a lower junction resistance. This change in resistance gives rise to tunneling magnetoresistance. Pinholes in the insulating layer of MTJs cause breakdown in tunneling. Properties such as smoothness of tunnel oxide layer play an important role in enhancing the TMR ratio of MTJs [18].

- *Granular films* - The TMR effect is also observed in highly resistive films known as granular systems, which are relatively easier to fabricate compared to MTJ systems. The problem of pinhole in the barrier does not affect the performance of such films. Granular thin films consist of nanometer size magnetic particles dispersed in a non-magnetic insulating material (fig. 1.1). These films have wide range applications because of their unique magnetic and transport properties, mainly controlled by the variation of concentration (x) or nominal thickness (t) of the magnetic materials. .

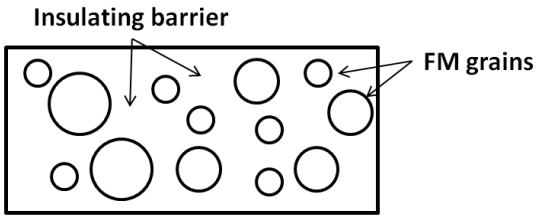

Figure 1.1: Schematic of granular film showing FM grains separated by insulating barrier

1.1.1 Basis of TMR in granular films: Spin Dependent Tunneling and Coulomb Blockade

Spin dependent tunneling (SDT) is an imbalance in the electric current carried by spin-up and spin-down electrons tunneling from one ferromagnetic layer to another through a tunneling barrier [19]. It is based on the fact that the probability for an electron to tunnel through the barrier depends on its Fermi wave vector. The existence of different Fermi wave vectors for spin up and spin down electrons in ferromagnetic material leads to the tunneling probability depending on spin. Magnetoresistance is a direct consequence of SDT. In granular film, electron tunneling depends on the relative orientation of the magnetic moments between magnetic grains

and hence exhibiting SDT(fig. 1.2). The tunneling resistance decreases when the magnetic moments of the granular are aligned in parallel to the applied magnetic field. In addition, the tunneling of electric charge into a small granule increases the coulomb energy by the charging effect, which opens the coulomb gap and strongly enhances the tunnel resistance because of coulomb blockade.

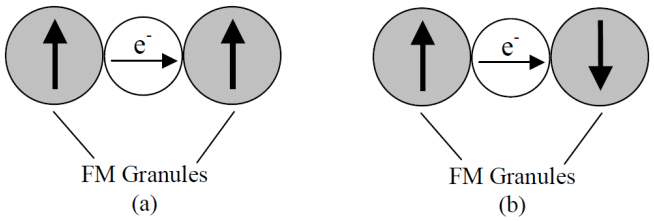

Figure 1.2: Schematic of SDT in granular film a) Lower resistance b) Higher Resistance

One of the most important energy parameters of the granular system is the single-grain Coulomb charging energy

$$E_C = \frac{e^2}{2C} \tag{1.2}$$

.

This energy is equal to the change in energy of the grain when adding or removing one electron and it plays a crucial role in the transport properties [9]. This charging energy introduces a gap for electron tunneling and gives rise to the coulomb blockade effect and therefore, tunneling is blocked unless the barrier presented by the charging energy is overcome by a bias voltage or thermal energy. When the applied voltage V and the thermal energy k_BT is much smaller than Ec, only electrons at Ec above the Fermi level can tunnel thus increasing the tunneling resistance by a factor of order of $e^{\frac{Ec}{2K_BT}}$. Hence, this suppression of electron tunneling when the bias voltage is below the threshold voltage is known as Coulomb blockade. The two important requirements for occurrence of Coulomb blockade(CB) are [20]:

1. The islands must be small enough and the temperature should be low enough so that the charging energy $E_c = \frac{e^2}{2C}$, required to add an electron to the island exceeds the available energy of thermal fluctuation i.e

$$Ec \gg k_B T \tag{1.3}$$

This condition prevents electrons from overcoming the Coulomb energy barrier due to thermal fluctuations.

2. The systems must have metallic islands that are connected to other metallic region only via tunneling barriers with a tunneling resistance R_T exceeding the resistance quantum R_K. This ensures that the island electrodes are weakly coupled to the rest of the circuit i.e. electrons cannot freely travel onto the island. The tunnel junctions must have a sufficiently large tunneling

$$R_T \gg R_K \tag{1.4}$$

where $R_K = \frac{h}{e^2} = 25.8 kOhms$ is the resistance quantum.

Therefore, it is understood that the basis of TMR in granular films are SDT and CB. In the following section we discuss the various research work done on granular films.

1.2 Granular films: Literature review

One of the earliest reports on granular films was in 1972 by Glittleman et al. [21], wherein they analyzed granular films prepared by co-sputtering nickel and quartz. They found that the Ni-SiO_2 system exists in 3 phases: paramagnetic at high temperatures, superparamagnetic at room temperature and ferromagnetic at low tem-

peratures. With the help of MR measurements, they were able to establish that the electron tunneling probability is spin dependent . In the following year, Sheng et al., published an article on temperature dependence of low-field conductivity in Ni-SiO_2 granular films. They varied the volume fraction of Ni and reported that the generation of the electrons for hopping conductance was due to the electric field and thermal effects. At higher fields, they found the thermal generation to be negligible whereas at the lower fields, thermally activated electrons were major contributors to the conduction. The authors arrived at the well-known equation for conductivity

$$\sigma \sim \exp(-\frac{b}{T^{\alpha}}) \tag{1.5}$$

with $\alpha = \frac{1}{2}$ at low electric fields based on the assumption that $sE_c = constant$ where s is the metal grain separation and E_c is the charging energy [22]. The first use of hard magnetic material for granular films was done in 1981 by Barzilai et al. from Hebrew university of Jerusalem [23]. Their research was based on Co-SiO_2 films wherein they confirmed the theory of spin-dependent tunneling in granular films and found that $JP = 1 \pm 0.3$ meV for cobalt, where P is the spin polarization and J is the exchange-coupling constant. They found that the dominant contribution to conductivity at high temperatures is due to tunneling between small grains separated by thin barriers, whereas at lower temperatures due to tunneling between larger grains with thicker barrier separation.

Around the past decade, there was a renewed interest in field of granular film research. Morawe and Zabel [24] succeeded in preparing discontinuous metal/insulator multilayer (DMIM) Co-Al-O granular film systems which presented similar magnetic properties. They grew Co/Al_2O_3 multilayer on sapphire substrates by RF sputtering techniques and they found that the Co percolation threshold was between 1.5 and 2.5 nm. The Co film was continuous for thicknesses greater than 3 nm. The

growth of Co was in a polycrystalline manner, whereas Al_2O_3 was amorphous. They suggested that the oxidation rate of Co was very low and the films can be used for high heat loads of up to 800°C. The following year (1996), Inoue and Maekawa proposed a simple yet effective law to describe MR performance in such films valid only at room temperature [25]. Their explanation accounted for the weak temperature dependence of MR ratio in Co-Al-O granular films unlike the previous theory of Helman and Abeles [26]. According to them, the tunneling mechanism for MTJ (FM/I/FM) could be applied to barriers between grains in the granular films, provided the magnetic orientation of the particles (θ) and the separation (s) between the grains are averaged. The conductance equation that they obtained was

$$G = Go(1 + P^2 m^2) \exp(-2\sqrt{2\kappa c/K_B T}) \tag{1.6}$$

where P-Polarization factor , G_0- Conductance when $P = 0$, $\kappa = \sqrt{\frac{2m_e\phi}{\hbar}}$ where ϕ is the barrier height, $c = \kappa s E_c$ where $E_c = e^2/4\pi\varepsilon\varepsilon_0 d$ is the charging energy and s is the thickness of the barrier and d is the grain size, $m^2 =< cos\theta >= L^2\left\{\frac{\mu H}{K_B T}\right\}$ and θ is the relative angle between the magnetization of adjacent super paramagnetic grains.

From experimental analysis point of view, one of the first comprehensive reports was published by Maurice et al. based on their investigation of Co-Al-O films [27]. They had sputtered Co cluster films embedded in alumina sandwiches at room temperature and found that the crystal structure of the Co grains was size dependent. The complete growth process includes the sequential deposition by sputtering of a first alumina layer, that of the metallic layer itself and that of a covering alumina layer. The latter is typically 4 nm thick, the overall alumina thickness being about 7 nm. As the nominal thickness of Co increased so did the grain size. It was HCP in larger bean-shaped clusters (greater than 3 nm) and often

fcc in the smaller, almost spherical clusters (fig. 1.3). The percolation threshold was for 2 nm of nominal Co thickness. They also found presence of Co clusters in their films, which are independent of the magnetic field [27].

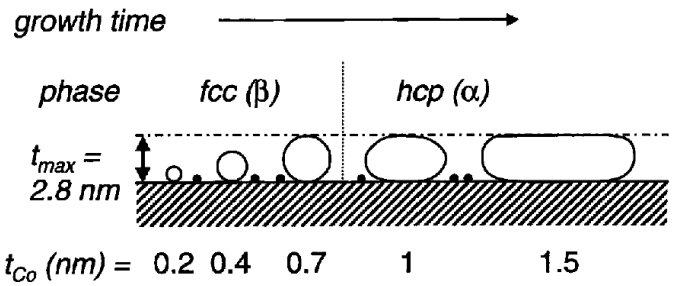

Figure 1.3: Schematic representation of growth as deduced from the TEM snapshots at t_{Co}. (There is a distance d between cluster edges, constant throughout the growth process) [27]

Takeno et al. [28] compared Co-Al-O with Co-Si-O and showed that Co-Si-O had MR ratios of around 4% while Co-Al-O had MR ratios of 7 – 8%. They concluded that that such differences could be attributed to different granular structures formed because of the change in insulating material as well as the change in dielectric properties of these oxides and hence Al-O dielectric gave better MR than Si-O based systems.

In 1997, Mitani et al. studied the spin dependent tunneling phenomenon in Co-Al-O films made by reactive sputtering. One of the most important things they noticed was that the GMR was a function of oxygen content i.e the quality of Al-O formed. They were able to achieve a maximum of 8 % MR at room temperature and 17 % at 4.2 K for Co-Al-O bulk films [29]. In the following year, they published an article on the temperature and bias-voltage dependence of MR in insulating current-perpendicular-to-plane (CPP) Co-Al-O granular films. They found that the MR showed strong temperature dependence and was enhanced by more than 20% at low temperatures. This anomalous increase of the MR at low temperatures was

attributed to the successive onset of higher-order processes of spin-dependent tunneling between large granules through intervening small ones with strong Coulomb blockade (shown in fig. 1.4) [30]. Therefore, the MR ratio can be increased by fabricating particles showing strong CB along the conduction path.

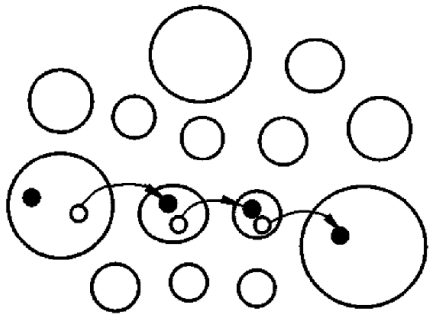

Figure 1.4: Higher-order tunneling process:Charge carrier transferred from the charged large granule (left) to the neutral large one (right) via the two small ones [30]

Honda et al. studied properties of Fe-SiO_2 granular films [6] by changing the volume fraction of Fe and analyzed its effect on grain size and MR ratio. They attributed the dependance of MR ratio and Fe volume fraction on the distance between the nearest neighbor grain surface. The M-H loop and magnetoresistance curve were fitted using a summation of Langevin functions which accounted for two distributions - one for smaller and the other for larger grains. It was also reported that the rate of saturation was faster for films with larger grains. They found that the anomalous behaviour of resistivity with temperature could be fit to $T^{-\frac{1}{2}}$ as predicted by Sheng et al. [22]. Their conductivity equation was given by

$$1/\rho(0) = 1/\rho_t \times exp(-2\sqrt{c/kT}) + 1/\rho_c \tag{1.7}$$

where $1/\rho_t, 1/\rho_c$ are constants and the latter is related to leakage conductivity due to field induced tunneling.

In 1999, Honda et al. reported a paper based on CPP Fe-SiO_2 granular devices

and found that the Fe grain size was dependent on the Argon (Ar) pressure used during sputtering and it decreases with increasing Ar pressure. It was shown that the grain size varies with volume fraction as well as thickness. Increasing volume fraction as well as thickness gives rise to larger grain size distribution.

In the year 2000, Yakushiji et al. investigated the particle size distributions in Co-Al-O insulating granular films with various Co concentrations and found that Single Electron Tunneling (SET) characteristic such as well-defined Coulomb threshold and Coulomb staircases were absent in the I-V characteristic of such films [31]. They attributed this to the wide distribution of Co cluster sizes and inter particle distances. Therefore, in order to observe the typical SET phenomenon, the tunneling paths must be restricted to a single path or a small number of paths. So Mitani et al. came up with the idea of granular nanobridge structure and observed clear Coulomb blockade and clear threshold (V_{th}). The nanobridge was made by FIB etching and consisted of a small piece of Co–Al–O granular film between a couple of point-shaped Nb–Zr–Si electrodes(fig. 1.5), [32]. The Coulomb blockade with a clear threshold voltage V_{th} and an enhanced TMR of about 30% at a voltage slightly above V_{th} was observed. The STM studies were also performed to clarify the topographic feature and the Coulomb blockade on the surface of Co–Al–O granular films.

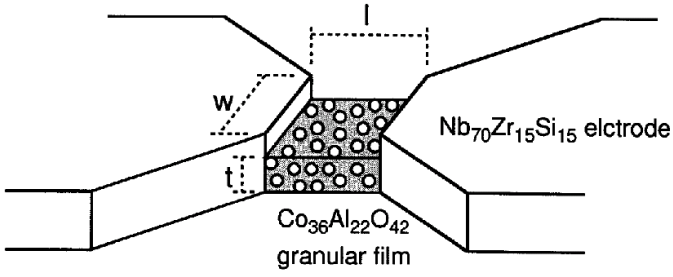

Figure 1.5: Schematic illustrations of a granular nanobridge [32]

In the year 2002, the same group led by Yakushiji experimented with the spin-dependent SET phenomena in CPP geometry for insulating granular systems. Their sample structure consisted of a 7-12 nm thick Co–Al–O granular film sandwiched by the top and bottom electrodes. A very thin Al–O layer was fabricated between the bottom electrode and the granular film as a bottleneck of conductance, leading to the successful observation of Coulomb staircases in the current–bias voltage I–V characteristics. The bias voltage dependence of tunnel magnetoresistance (TMR) shows clear oscillatory behaviour associated with the Coulomb staircase. The TMR oscillation is interpreted as a phenomenal characteristic of spin-dependent single-electron tunneling. They utilized two different types of electrode: ferromagnetic and non-ferromagnetic, and still observed the same phenomenon [33, 34].

Asami et al. [35] who worked on preparation of Co-Al-O films using R.F. sputtering in Ar + O2 atmospheres observed from XRD measurements that there was presence of CoO in the granular film. Actually, the oxygen affinity for Al is higher than that of Co and Al should be preferentially oxidized because of bond enthalpy values of Co-O[1] and Al-O[2], which are 384.5±13.4 $\frac{KJ}{mol}$ and 511±3 $\frac{KJ}{mol}$ respectively. However, even other researchers have found traces of Co oxides (CoO and Co_3O_4) in Co-Al-O films prepared by co-sputtering of Co and Al_2O_3 targets in Argon ambient [10]. Fujimori et al. [36] reported that on increasing the oxygen concentration during reactive sputtering, the width of the tunneling barrier in the film decreases instead of increasing. They also observed a marked decrease in MR with increasing oxygen content and attributed both these findings to the presence of Co oxides .

Kakazei et al. have studied the properties of discontinuous multilayers of $Co_{80}80_{80}$ deposited by Ion Beam sputtering [37]. They measured TMR in both CIP and CPP geometries and were able to achieve up to 6.5% at room temperature and 11% at 15

[1]http://www.webelements.com/webelements/elements/text/Co/enth.html
[2]http://www.webelements.com/webelements/elements/text/Al/enth.html

K for as-deposited films in CIP geometry. However they were unable to obtain high MR for CPP devices. They attributed this difference to the large voltage applied in CPP between consecutive layers and hence leading to high electrical field regime which is magnetic field independent. The temperature dependence of MR was also quite different for the two geometries. CIP showed a stronger dependance compared to CPP geometry. This dissimilarity was explained based on different short-range magnetic correlations between neighbor granules in the same layer and in adjacent layers.

1.2.1 Materials used for fabrication of granular films

Research has been carried out on the fabrication and analysis of granular films made using different combinations of ferromagnetic materials (Ni, Co, CoFe, Co-Pt etc) and insulators (Al-O, Ta-O, Al-N, TiO_2,ZrO_2, SiO_2, MgF_2 etc) and their properties are being extensively explored up to the present [6,8,22,25,27,30,32–34,38–57]. Most of the research work focus on Al-O because it gives higher TMR ratios compared to other oxides [6, 8, 58, 59]. The oxide serves as a barrier to separate ferromagnet particles and it is expected that TMR ratio and other magnetic properties should be independent of the type of oxide. However, research articles have shown that magnetic properties change with choice of oxide material [8]. This is possibly due to FM metal-oxides formed during the deposition and various articles have shown the presence of cobalt-oxide [10,35,58,60,61] and iron-oxide [62] in Co and Fe based systems respectively. This FM metal-oxide are anti-ferromagnetic(AFM) in nature and lead to spin flip scattering which in turn reduces the TMR ratio. Fujimori et al. did a study on Co-Al-O films with change in oxygen concentration [36]. They also showed calculations of MR based on Fe, Co, Ni based systems. Although the actual polarization factors (P) for Fe, Co and Ni are 0.44, 0.34 and 0.2 respectively

the MR obtained did not reflect this trend. The Co based systems gave the highest magnitude of MR as compared to Fe based systems. So, they concluded that the effective values of spin polarization factor should be considered and Co has a better effective spin polarization than Fe [36].

1.2.2 Interactions in granular films

Granular films consist of super paramagnetic particles and the magnetic properties of the film are supposed to be obtained from the individual contribution of FM granules. But experimental results by various researchers have shown that it is not that simple because of two facts: a) Interaction between the granules b) Grain size distribution [48].

In 1990, Berkov and Meshkov published a theoretical paper on how hysteresis can be observed in an assembly of chaotic distributed particles without intrinsic magnetic anisotropy due to inter particle magnetostatic interaction [63]. In 1999, Allia et al. made use of this theory to explain the characteristics of their metallic Cu-Co granular film and how the magnetic contribution was a result of both FM particle distribution and inter particle interactions [64]. In the year 2001, Allia et al. came up with the concept of interacting superparamagnetic particles (ISP) to explain the anomaly in the M-H loops and their fitting for CoCu films. In 2002, Kechrakos and Trohidou suggested that intergranular interactions play an important role in the magnetic configuration of the film [65]. They found that the uniaxial anisotropy energy of the granules and their dipolar interaction determined the magnetic property of the film. In another paper by the same authors published in the same year, they showed with the help of simulations that magnetostatic interactions between nanoparticles in magnetic granular films are responsible for flattening of

the MR parabola at weak fields. The flattening is enhanced by the presence of a size distribution of nanoparticles or clusters of nanoparticles in samples close to percolation [66].

In 2005, Brandl et al. studied the effects of dipolar interaction in insulating granular film with the help of the ISP model. They studied the behaviour of Co particles dispersed in an amorphous insulating SiO_2 matrix and explained the magnetic behavior using the ISP model . An almost constant behavior of mean magnetic moments is expected at low T and the decrease in their contribution is supposed to occur only when T approaches the Curie temperature T_c (1404K for Co), owing to the corresponding reduction of M_s. But from their experimental results they found that the mean magnetic moment was found to increase with T for their samples. This according to them, was due to the inadequacy of the conventional super paramagnetic model and that the mean magnetic moment is in fact an apparent moment, generated due to magnetic interactions [45]. According to Denardin et al., the interparticle interactions compete with the magnetic anisotropy in determining the orientation of the particle moments. If they are strong enough, the interactions can make a collection of individual superparamagnetic moments that behaves like a collective magnetic system. A disordered collective state, or spin cluster glass, is expected when the system is dominated by dipolar interactions. Also, a ferromagnetic state can be formed in the case that the interactions are dominated by exchange coupling [43].

In a very recent paper by Mao et al., they have reported results based on Co-ZrO_2 films. According to their research article, the interparticle interactions cause the magnetization of the particles in the range of correlation length to align ferro-

magnetically and fluctuate collectively as a ‘‘superparticle’’ under the applied field. As the field increases, it overcomes the interactions and pulls the magnetic moments to fluctuate individually along the field direction, leading to the reduction of correlated particles. Therefore, the correlation length decreases with the increasing applied field. The applied field plays two roles in the magnetization process: destroying the interparticle ferromagnetic correlation and magnetizing the system at the same time [67].

1.2.3 Devices based on granular films

In 1998, Kobayashi et al. successfully demonstrated the application of granular in gap (GIG) structure to enhance the low field MR response of granular films (fig. 1.6). Permalloy($Fe_{66}Ni_{34}$) and Co_{39} $Y_{14}O_{47}$ nano-granular materials were selected as soft magnetic and TMR materials respectively as Fe-rich permalloy has a large saturation magnetization, while the Co_{39} $Y_{14}O_{47}$ film has a higher thermal stability than other TMR granular films. The researchers found that the MR of a GIG films exhibited a huge field response at low magnetic fields and the MR ratio at 2 Oe was more than 2.5%, which was approximately 250 times larger than that of a Co_{39} $Y_{14}O_{47}$ single layered film with no permalloy layer. They inferred that the huge field response was due to the effect of strong magnetic flux from the $Fe_{66}Ni_{34}$ film passing through the Co_{39} $Y_{14}O_{47}$ layer in the structure and the MR of the GIG film was dependent on the the magnetization of the $Fe_{66}Ni_{34}$ layer [7]. Most of the research on GIG is based on CIP devices and there are no CPP based structures in literature utilizing the effect of soft magnetic materials to enhance the magnetic field.

In the year 1999, Fukumoto et al. fabricated a hybrid MTJ device which utilized

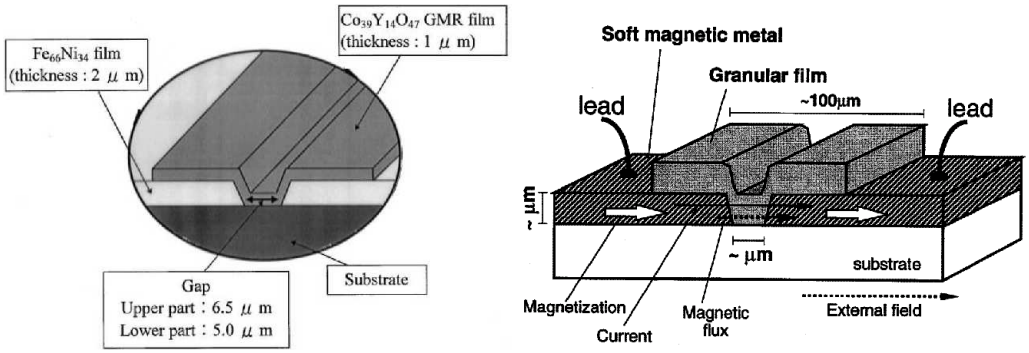

(a) (b)

Figure 1.6: a) schematic diagram of the GIG structure consisting of $Fe_{66}Ni_{34}$ and $Co_{39}Y_{14}O_{47}$ films by Kobayashi [7] b) GIG representation by Fujimori et al. [8]

the concept of granular films. The fabricated structure consisted of FM/Granular/FM multilayer where the granular film consisted of either

- **First device:** Al-O/Co/Al-Co
- **Second device:** Al-O/Co/Al-Co/Co/Al-O (fig. 1.7).

They carried out four probe dc measurements for temperatures between 2K-300K with a maximum field of 3 Tesla. The MR and the resistance for both the devices were found to increase with decreasing bias voltage at low temperatures. But the increase was smaller for the first device (fig. 1.7(a)) as compared to the second device (fig. 1.7(b)). In other words, the first device reached resistance saturation at very low temperatures. The authors have explained this taking into account the leakage current due to direct tunneling between the electrode in the first device, which is not so viable in case of the second device [68].

In 2005, Sukegawa et al. fabricated a similar device structure- CoFe/ AlOx /CoFe /AlOx /CoFe ferromagnetic double tunnel junctions (fig. 1.8) and studied the spin dependent tunneling phenomena. The middle layer CoFe layer was fabricated in a discontinuous manner, the average diameter being 2.0–4.5 nm (from cross-

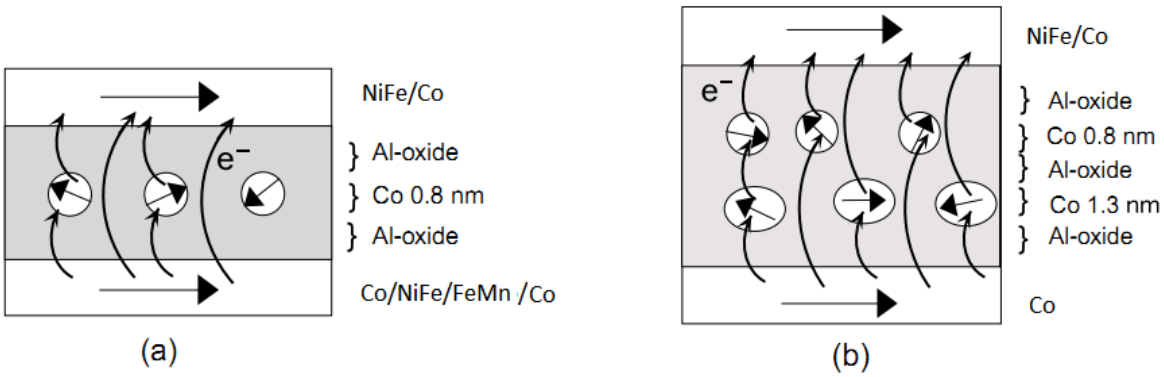

Figure 1.7: The fabricated devices by Fukumoto et al. a)NiFe/Co/Al-O/Co/Al-O/Co/NiFe/FeMn/Co b)NiFe/Co/ Al-O/Co/Al-O/Co/Al-O/Co [68]

sectional TEM images). For temperatures below 50 K, a Coulomb gap was observed in current-voltage curves and both MR ratios and resistances were found to increase significantly with decreasing temperatures. This indicated that the co-tunneling process was dominant within the gap and they have also proved it theoretically [69].

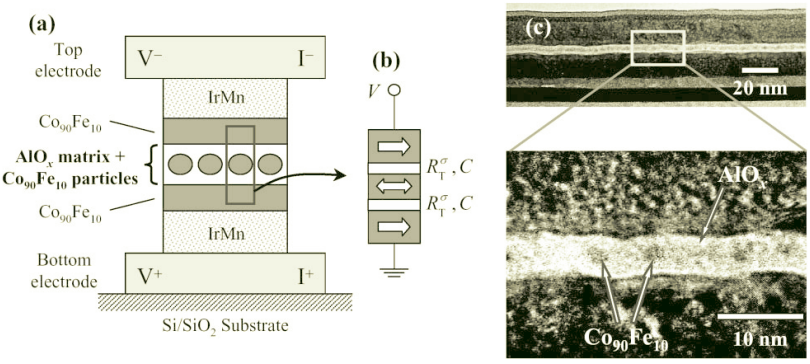

Figure 1.8: Schematic illustrations of (a) the symmetric DTJ and (b) the hybrid junction. The arrows indicate the magnetization of the electrodes. (c) Cross-sectional TEM image of the $Co_{90}Fe_{10}$/AlOx/$Co_{90}Fe_{10}$/AlOx/$Co_{90}Fe_{10}$ DTJ region [69].

1.2.4 Grain size distribution measurement

For granular films, the grain size distribution governs the magnetic and magneto-transport properties of granular films.There are different techniques used for obtain-

ing the grain size for such films namely TEM, SAXS, Langevin fitting and blocking temperature. Each of these techniques are discussed below.

Transmission electron microscopy (TEM) : For viewing features of the order of a few nanometers, a TEM is employed. Samples that are thinner than 100 nm will have, on an average, one scattering event for electrons accelerated to ~100 keV. Grain size can be determined either from bright field images or by dark field imaging [70,71]. In bright field imaging, an unscattered electron beam is used for the imaging of the sample whereas the dark field image is formed using the electrons that have been scattered elastically. Since the number of electrons scattered inelastically is very small, these two images are essentially mirror images of each other. Since the amount of diffraction cross-section is primarily determined by the atomic number of the elements, a contrast across different materials is immediately obtained. In bright field images, high-Z (atomic mass) regions of a specimen scatter more electrons than low-Z regions of the same thickness. Similarly, thicker regions will scatter more electrons than thinner regions of the same average Z, all other factors being constant. Bright field imaging technique to determine grain size distribution in granular films has been used in various literature [6, 38, 45]. Yao et al. [72] and Denardin et al. [73] have made use of dark field imaging to determine the grain size distribution in their respective films. TEM sample preparation is a time consuming process and always has the possibility of altering the film microstructure of the film during grinding, polishing or heating steps involved [74]. Another drawback of TEM is that the grain size of such films is dependent on atomic size Z and hence becomes difficult to distinguish closer atomic size elements using TEM.

Langevin fit : The granular films have a distribution of grains and this information can be obtained from the M-H loop for the films. Various researchers have used Langevin function or rather summation of Langevin functions to fit the M-H

loop to obtain the grain sizes [6, 59, 75].

Scattering angle x-ray spectroscopy (SAXS) measurements: SAXS measurement can be performed to compute the grain size distribution as well as the intergranular distance [76]. Nunes et al. [77] and Ohnuma et al. [78] have employed this technique to determine the grain size distribution as well as the inter-particle distances. For performing measurements, special substrate such as kapton, mica etc is required so that the signal from the substrate does not interfere with the signal from the film. However, the thickness of the films have to be of the order of 100 nm to obtain any legible signal.

Field Cooling/Zero Field Cooling Measurement - Granular films are usually not mono-dispersive in nature and have particle size distributions. It has been found through various experimental analyses that they usually follow the log normal distribution. Each particle distribution gives rise to magnetic moment distribution. It is well know, that the magnetization is given by

$$M(H,T) = \int_0^\infty \mu L(\frac{\mu H}{K_B T}) f(\mu) d\mu \tag{1.8}$$

So, one of the basic magnetization techniques is the measurement of magnetization as a function of temperature. It is usually done by Zero-field-cooling (ZFC) and field-cooling (FC) measurements, which can provide information on mean blocking temperature (T_B) and particle size distribution. These measurements are carried out using magnetometers based on the Superconducting Quantum Interference Device (SQUID) and are the most sensitive instruments available for measuring magnetic field strength.The example of such a system is Quantum design's Magnetic Property Measurement System (MPMS®)[3]. A measurement is performed in the MPMS by moving a sample through the superconducting detection coils. As the

[3]http://www.qdusa.com/products/mpms.html

sample moves, the magnetic moment of the sample includes an electric current in the detection coils. As the detection coils, connecting wires, and the SQUID input coil form a closed superconducting loop, any change of magnetic flux in the detection coils produces a change in the persistent current in the detection circuit, which is proportional to the change in magnetic flux. Since the SQUID functions as a highly linear current-to-voltage convertor, the variations in the current in the detection coils produce corresponding variations in the SQUID output voltage which are proportional to the magnetic moment of the sample.

The ZFC curve is obtained by demagnetizing the sample at temperatures greater than the blocking one and afterward cooling it without applied field down to a temperature much lower than T_B, to finally apply a small field H_m to measure magnetization during the subsequent temperature rise. The FC curve is obtained in a similar manner except for the fact that a small magnetic field is applied even during the cooling process. In a superparamagnetic system of non-interacting identical particles, the peak of the MZFC curve is strongly related to T_B. In real systems, the distribution of T_B i.e $f(T_B)$ can be calculated as $\frac{d[M_{FC}-M_{ZFC}]}{dT}$ easily estimating the mean blocking temperature $\langle T_B \rangle \overline{T_B}$. [23,73,77,79]. From $f(T_B)$ the $f(diameter)$ the distribution of particle grain size can be easily estimated using the equation

$$T_B = \frac{KV}{25k_B} \tag{1.9}$$

where K is the anisotropy constant of Co, V is the volume of the FM grain and K_B is the Boltzmann constant. This method of fitting is shown in fig. 1.9 as described in ref [73].

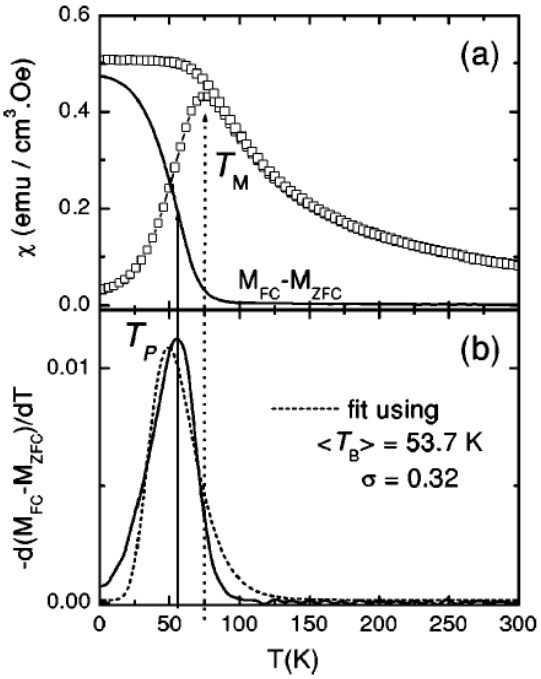

Figure 1.9: Grain size distribution measurement from FC/ZFC as in ref [73]

1.2.5 Theoretical models for granular films

In order to supplement the experimental work on granular films, theoretical models were developed for the same. One of the foremost models is the one suggested by J.Inoue and S.Maekawa in 1996 [25]. According to this model (eq.1.10), the thickness of the granular film does not affect the MR ratio. But this does not agree with experimental results which show that thickness of the granular film affects the MR ratio [75, 80]. This is because the Inoue model averages out the grain size and grain separation and is based on the modification of the MTJ equation. The conductance equation given by Inoue is given by

$$G_{ij} = Go(1 + P^2 cos\theta) \exp(-2\kappa s - c/sK_BT) \tag{1.10}$$

where P-polarization factor, G_0- Conductance when $P = 0$, $\kappa = \sqrt{\frac{2m_e\phi}{\hbar}}$ where ϕ is the barrier height, θ- Relative angle between the magnetization of adjacent super

paramagnetic grains, $c = \kappa s E_c$ where $E_c = e^2/4\pi\varepsilon\varepsilon_0 d$ is the charging energy and s is the thickness of the barrier and d is the grain size. This can be further simplified as $< cos\theta >= m^2 = L^2 \left\{ \frac{\mu H}{K_B T} \right\}$

Kakazei et al. [48] proposed a 2D model for CIP conduction in CoFe-Al_2O_3films. Granular film is visualized as 'n" stacked regular arrays of identical granules (fig. 1.10). The distance between the grains along the horizontal plane is smaller than that of the vertical plane. Kirchhoff voltage and current law equations are used to derive the resistance for each layer. However their model could not explain all their experimental results. They are attributed to random fluctuations of interlayer spacings and interlayer shortcuts (large metallic patches) which could exist in the experimental films.

1.3 Motivation for the current work

Granular films are an interesting topic for research because of their potential applications such as high coercivity films in information storage, bit writing at high frequencies and moderate MR elements for read heads and magnetic sensors. The major advantages of these films is that their magnetic properties such as coercivity and interactions etc can be tailored by controlling their grain size [9, 10] .

As described in the literature review, researchers have found that in the most commonly studied granular systems namely Co-Al-O, there is presence of Co oxides (CoO and Co_3O_4) in the granular films, which are anti-ferromagnetic in nature with Neel Temperatures of 293 K and 33 K respectively. Beyond the Neel temperature, the magnetic moments of the anti-ferromagnetic material become disordered and the Co phase no longer retain preferential direction of magnetization. Hence CoO causes strong spin flip scattering at room temperature and this scattering reduces the net polarization of the tunnel electrons leading to a decrease in MR. Hafnium

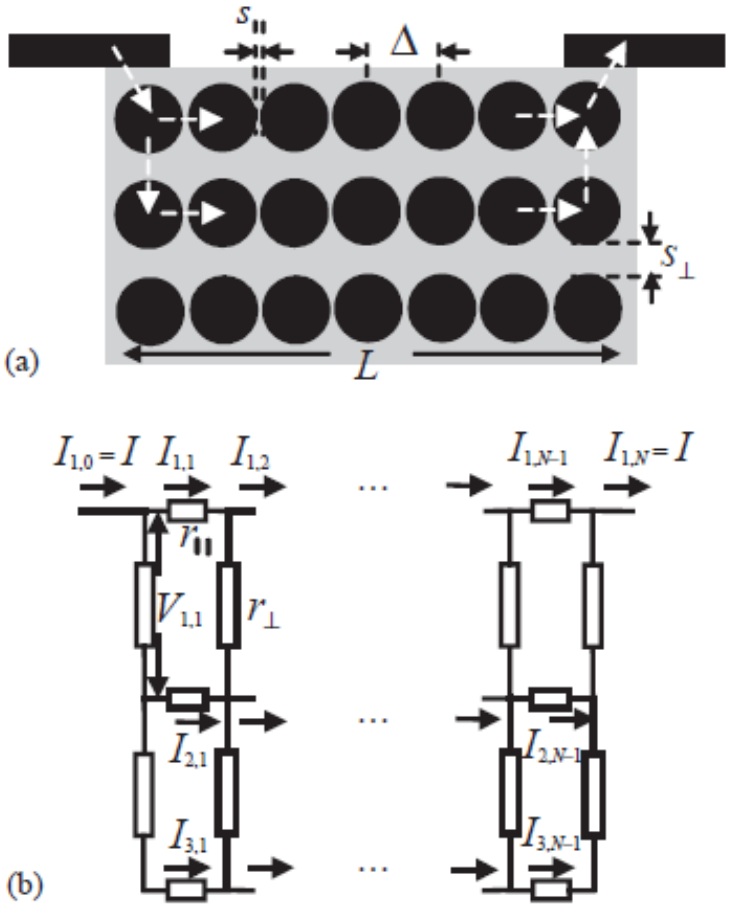

Figure 1.10: Model of tunnel conductance in a granular multilayered system under top electrodes (a) and the equivalent circuit (b) as per ref [48]

oxide is used for reducing/eliminating the CoO from such films. Hafnium oxide has a high bond enthalpy (801.75±13.4 $KJ.mol^{-1}$) as opposed to Co-O (384.5±13.4 $KJ.mol^{-1}$) and Al-O (511±3 $KJ.mol^{-1}$). This high heat of formation of HfO_2 implies that Co oxidation would be considerably reduced as the disassociation of the Hf-O bond is more improbable than the Al-O bond [36,81]. As presented in the literature review, Co has a higher effective polarization compared to Fe and hence it is chosen as the magnetic material for preparation of granular films. Some work on characterization and sputtering of Co-HfO_2 films have been carried out in our group.

Research articles on granular films make use of variation in materials, deposition conditions, dimensional control etc to improve the MR response and quality of the films. Flux enhancement techniques are also used to improve the MR ratio [7]. However, there are no research articles studying the modification of these structures by inserting oxide or metallic films into these system.

Simulation models for granular films show that the MR ratio remains the same in spite of the varying thickness of the films [25, 82]. However, experiments show that this is not the case and as the thickness of the granular films changes, so does the MR ratio [48, 80, 83]. This increase is attributed to change in grain size with thickness of the granular films [48, 64, 84]. It was observed in a paper by Mitani et al. on Co-Al_2O_3 films that smaller grains lead to CB and help in increasing the MR ratio at lower temperatures. Currently, there are no techniques to control grain size or engineer transport properties of granular films for a given volume fraction.

Both CIP and CPP devices based on granular films of different materials have been fabricated and their transport properties have been analyzed. However, it was found that CPP devices always have lower MR than their CIP counter part. Although there are methods to improve CIP MR using GIG like structures [7], the CPP devices have no such implementation.

Thus, this provides the motivation to fabricate various structures based in Co-HfO_2 with the objectives in the following section.

1.4 Objectives

The objectives of this research work are

- To study structures based on Co-HfO_2 films
- To make use of the effect of roughness to control grain sizes of granular films

and thus engineer different kinds of transport for the CIP devices. This is to be achieved by inserting an oxide layer in between the granular film. We intend to generate grain size small enough to observe CB regime and large enough to improve MR ratio.

- To modify existing simulation model and implement the same for CIP transport for the above roughness experiment
- Fabricate CIP and CPP structure with oxide insert and understand the difference in transport properties of the two geometries.
- To implement flux enhancement for CPP granular film devices by inserting a soft magnetic layer and study the transport properties

1.5 Organization of thesis

Chapter 1 introduces the research work and provides the literature review and motivation for the thesis.
Chapter 2 discusses the standard granular film structures consisting of 10 and 20 bilayers and Co and HfO_2 respectively.
Chapter 3 discusses the device properties using the proposed structure and provides in depth analysis for the results.
Chapter 4 discusses the simulation model implemented for the CIP conduction for the proposed structure.
Chapter 5 discusses the CIP vs CPP structure based on the proposed structure in chapter 3.
Chapter 6 discusses the CPP based Py layer structure.

Chapter 2

Granular films: Background and initial experiments

This chapter briefly describes the background work done on Co-HfO_2 granular films, followed by fabrication and characterization of these films. The final section of the chapter introduces bulk granular films and microdevices based on structures G and 2G. As described in the motivation, G and 2G are standard films which form the basis for comparison for the proposed structures in this thesis.

2.1 Summary of previous research carried out on Co-HfO_2 granular films in our research group

The summary described in this section is from ref [74]. Findings and experiments relevant to the background of this thesis have been explained in this section

Sputtering: Sputtering is employed for deposition of Co and HfO_2. The important sputtering parameters include a) sputtering gas partial pressure b) power of targets and c) base pressure. It is known that low Ar sputtering gas pressure

results in small plasma scattering and higher nucleation rate and hence preferable. However, lower deposition pressure leads to non-uniform target wear causing target wastage and non-reproducibility of sputtered films. Five mtorr was used to overcome non-uniform usage of target as well as triggering the oxide target and sustaining the plasma for longer periods of time. Lower power correlates to low sputtering rate and formation of smaller grains. Plasma sustenance over long periods of time became an issue for powers below 30 W and hence 30 W was chosen as the deposition power for both Co and HfO_2 targets. As far as the base pressure is concerned, the AJA sputtering system had a base pressure of 10^{-8} Torr for the deposition chamber.

Sequential sputtering of Co and HfO_2 was well researched and compared with other techniques such as co-sputtering and evaporation. This process has been optimized for Co and HfO_2 by our group [74] and its schematic representation is shown in fig. 2.1a. When a thin layer of Co of nominal thickness t(Co) is deposited say less than 1.2 nm, instead of forming a continuous layer it breaks up into small isolated Co islands. The Co layer splits up into discontinuous particles as the film growth proceeds via a three dimensional or Volmer–Weber mode. When we deposit a layer of HfO_2 having a nominal thickness t(HfO_2) , the HfO_2 layer follows the topography of the deposited Co particles and it gets deposited either in-between and/or above the Co granules. The joint growth model depends on the ratio of t(Co) and t(HfO_2) and can be analyzed based on two different regimes in terms of Co and HfO_2thickness as shown in fig. 2.1

1. t(Co)<=t(HfO2)

2. t(Co)>t(HfO2)

Characterization: As described in the motivation of this thesis, use of HfO_2 reduces the formation of CoO compared to other oxides used for granular films. Fig.2.2 shows the experimental X-ray photoelectron spectroscopy (XPS) analysis

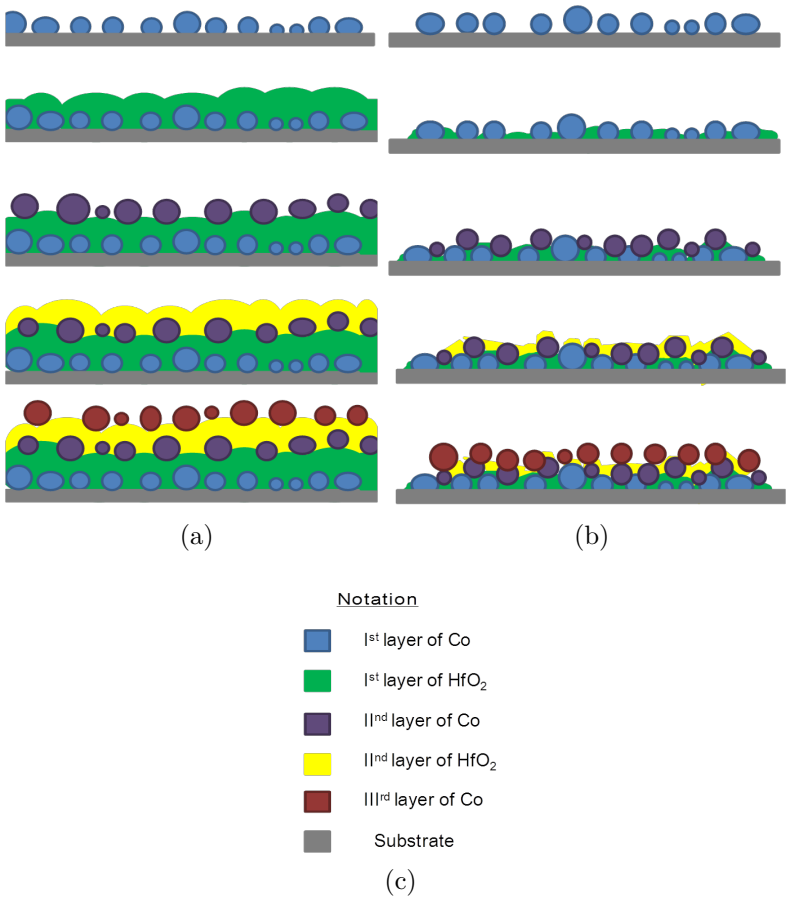

Figure 2.1: Schematic of sequential sputtering of Co and HfO_2 when a) t(Co) <= t(HfO_2) b) t(Co) > t(HfO_2) ref. [74]

done on Co-HfO_2 and Co-Al_2O_3 films prepared by sequential sputtering. The experimental details are in ref. [74]. A peak at a BE of 778.2 eV is observed for all the spectra, which corresponds to metallic Co. However Co-Al_2O_3 spectrum shows a small peak at higher BE. The spectrum (d) is obtained by subtracting (b) from (c), and it shows a broad peak centered at 781.0 eV along with a satellite structure $\sim$ 5 - 6 eV ahead of the main peak. As the residual spectrum shows broad peak with satellite structure, these features along with BE's matches with the cobalt oxide peaks. Hence this can be attributed to presence of cobalt oxide in Co-Al_2O_3 along with the elemental Co in this film. For Co-HfO_2 films only elemental Co can be found (fig.2.2). These observations are valid for Co-Al_2O_3 films prepared by co-sputtering [10] as well as sequential sputtered films as well [85]. The XPS scans of Co-HfO_2 of different compositions ranging from 27% to 55% were checked and an absence of cobalt oxide was confirmed in all samples. The above analysis shows successful reduction of cobalt oxide formation with the introduction of HfO_2 insulator. This can be explained based on the fact that the bond energy of HfO bond (801 $\pm$ 13 kJ/mole) is higher as compared to AlO (501.9 $\pm$ 10.6 kJ/mole) and CoO bond (397.4 $\pm$ 8.7 kJ/mole) [74, 86]. In the case of Co-Al_2O_3 films the comparable bond energies of AlO and CoO might lead to the formation of certain amount of CoO whereas for Co-HfO_2 films, the much higher difference between the insulator and the ferromagnet-oxide strongly discourages the possibility of CoO formation.

In order to understand the stoichiometry of Hafnium oxide, the chemical state of Hf was analyzed in the cap and the film regimes and it was found that Hf exists in +4 oxidation state [74, 87]. Detailed analysis and descriptions are available in ref. [74].

Grain size distribution (TEM) :

As described in Chapter 1 section 1.2.4, some of the techniques used to find

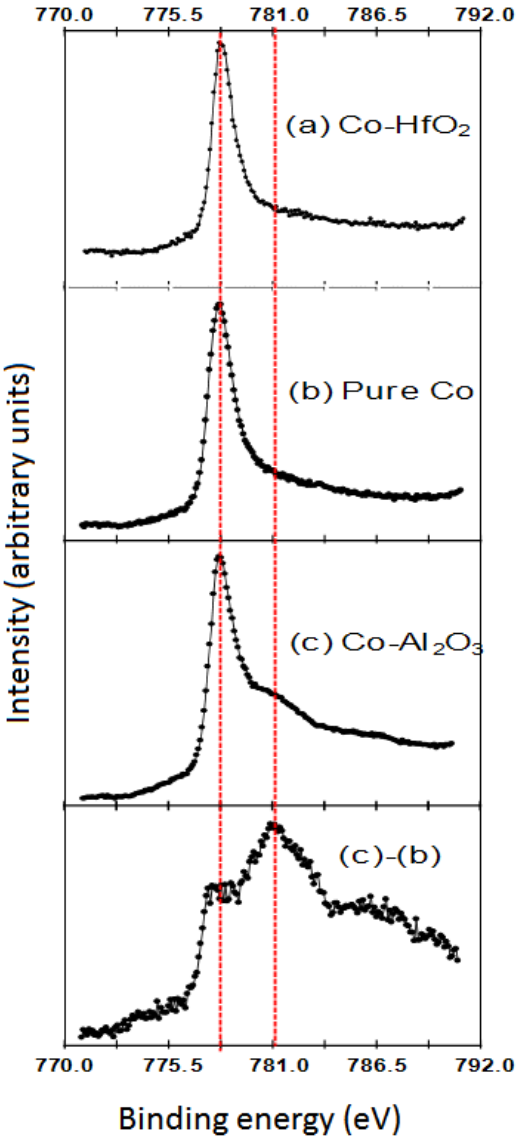

Figure 2.2: Co $2p_{3/2}$ spectrum for (a) Co-HfO_2 (b) pure Co film (c) Co-Al_2O_3 film and (d) amplified spectrum obtained from ((c) – (b)).ref. [74]

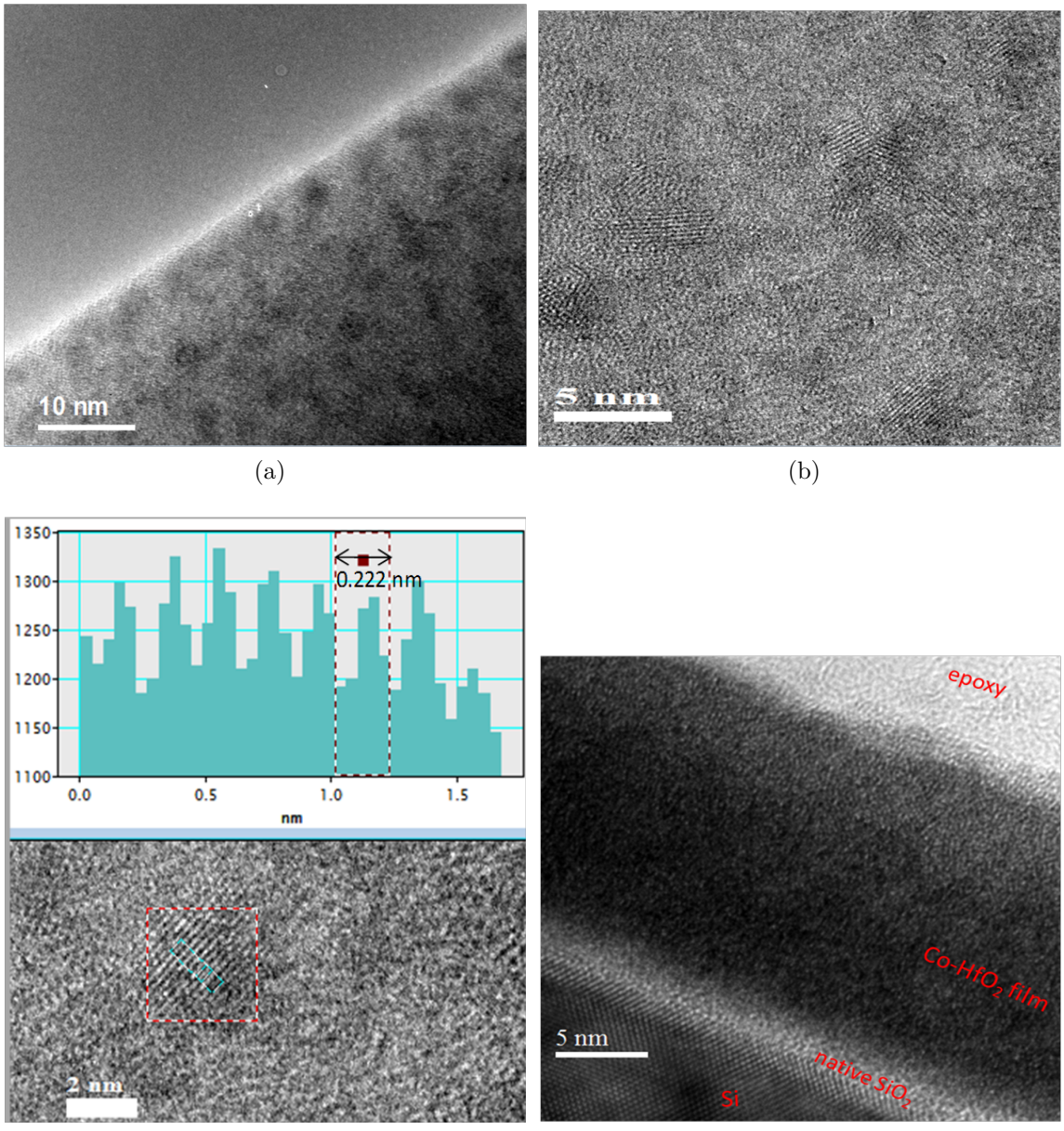

Figure 2.3: TEM of Co-HfO_2 granular films a) Planar-view b) HRTEM planar-view c) Lattice Fringes shows d-spacing of ~0.222 nm d) Cross sectional view ref. [74]

the particle size/distribution of granular films are TEM and SAXS. However, SAXS requires thicker samples of ~100 nm or greater to give consistent and reliable results. Our samples had a thickness of less than 40 nm for the active granular film layer and SAXS measurements were not successful. TEM which is based on atomic number (Z) contrast, failed to give any conclusive evidence for the samples because of the close atomic numbers (Z) of Co (Z=27) and HfO_2 (Z=29.33)[1]. Similar issue was reported by Kim et al. [88] for Co-Cu granular films because of the close atomic numbers of Co and Cu, and hence they employed alternative techniques based on M-H loop and ZFC/FC measurement to find the grain size distribution. In this thesis ZFC/FC measurements are used to find the grain size for the various samples as will be discussed in Chapter 3. The results are also corroborated using the simulation model discussed in chapter 4 which also helps in obtaining the relative grain size distribution for the samples.

Our group did make some TEM measurements [74] and the results have been discussed here for reference and understanding. Some of the bright field planar view TEM measurements for the Co-HfO_2 film is shown in fig.2.3. The film composition consists of 10 bilayers of Co and HfO_2 with a thickness of 0.9 nm each. Dark circular patches were seen in featureless light background as shown in fig.2.3a. However high resolution TEM in fig. 2.3b shows clear fringes. The fringe separation was calculated using digital micrograph software to be ~ 0.222 nm [74, 89]. Therefore for majority of fringes the spacing corresponds to HCP Co whereas for minority, it was difficult to distinguish whether the diffraction pattern corresponds to Co or HfO_2 due to the lack of contrast discussed earlier. To check the crystalline elements in Co and HfO_2, X-ray diffraction (XRD) was also performed on Co-HfO_2film. However no crystalline signal either for Co or HfO_2 was captured in XRD scan, possibly due to the small thickness of Co and HfO_2 present in the film (~ 20 nm). Thus it can be

[1]Avg Z (HfO_2)=[Hf(Z=72)+2×O(Z=8)]/3=29.33

concluded that Co mainly exists in HCP phase in the fabricated Co-HfO_2 films.

2.2 Fabrication methodology

2.2.1 Substrate Cleaning

In general, two types of substrate were used for fabrication of granular films

- Single side polished n-type Si (100) substrate with resistivity of 1-100 Ω-cm were used for non-electrical measurement e.g. M-H loop measurement, Rutherford Back Scattering (RBS)
- Double sided polished glass slides with resistivity of ~10^{10} to 10^{12} Ω-cm were used for electrical measurements.

Prior to lithography or deposition, the wafers were cleaned of impurities by first soaking in acetone for 25 minutes and agitating in an ultrasonic bath to remove any particles adsorbed onto it. The acetone is subsequently washed off by immersing the wafer in isopropanol for another 25 minutes with ultrasound agitation. Lastly, the wafer is blown dry with purified nitrogen gas.

2.2.2 Material Deposition

As described in section 2.1, sequential sputtering is employed for deposition of the Co and HfO_2 films. In this research work, AJA[2] sputtering tool with dc and rf sputtering capabilities is used for the deposition of the granular thin films. Co target with purity of 99.99 % and HfO_2 target with purity of 99.95 % are deposited using dc and rf power source respectively. Prior to the deposition of the films, pre-sputtering of each target was performed for ~15 minutes. No substrate bias,

[2]http://www.ajaint.com/

substrate heating or magnetic field was used during the deposition.The base pressure of the sputter system is 10^{-8} torr while the working pressure is 5 mtorr with a Ar flowrate of 20 sccm. Power of 30 W is used for sputtering Co and HfO_2 targets each. The sputtering rates were individually calibrated for Co and HfO_2 targets by plotting thickness vs. time of deposition. The thicknesses of the film were calculated based on deposition on lithography patterned sample. Sample of various thicknesses were sputtered and the resist was later lifted off in acetone. The film thickness was measured at various step height locations across the sample using atomic force microscope (AFM). The deposition rates are calculated for the films using thicknesses greater than 4 nm to ensure continuity of the films. The calculated deposition rate is used to sputter the Co and HfO_2 films of thickness less than 1 nm in this thesis. Though the films formed are discontinuous in nature, it is ensured that the volume of material deposited would be same as that of continuous films of equivalent thickness. The deposition rates for Co and HfO_2 targets were found to be ~0.25 $\dot{A}/s$ and ~0.1 $\dot{A}/s$ respectively(fig 2.4). Preliminary research showed that alternate sputtering of Co and HfO_2 for a total of 10 bilayers was optimum in terms of MR ratio and response [74].

2.2.3 Photolithography used for fabrication of granular film devices

Photolithography is utilized for fabricating the microdevices. Ultraviolet (UV) light of 365 nm wavelength is used to transfer patterns from photo mask to a light-sensitive chemical photoresist coated on a substrate. The steps involved in the process include photoresist application, soft baking, mask alignment (if any), exposure and development [90]. AZ 7220 positive photoresist is spun at 5000 rpm to obtain the desired resist thickness of ~2 μm and then baked at a temperature of

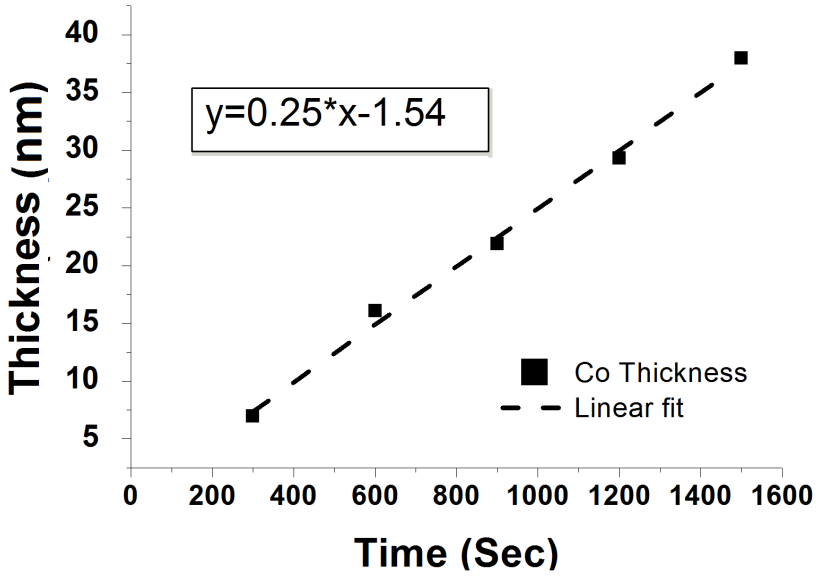

(a)

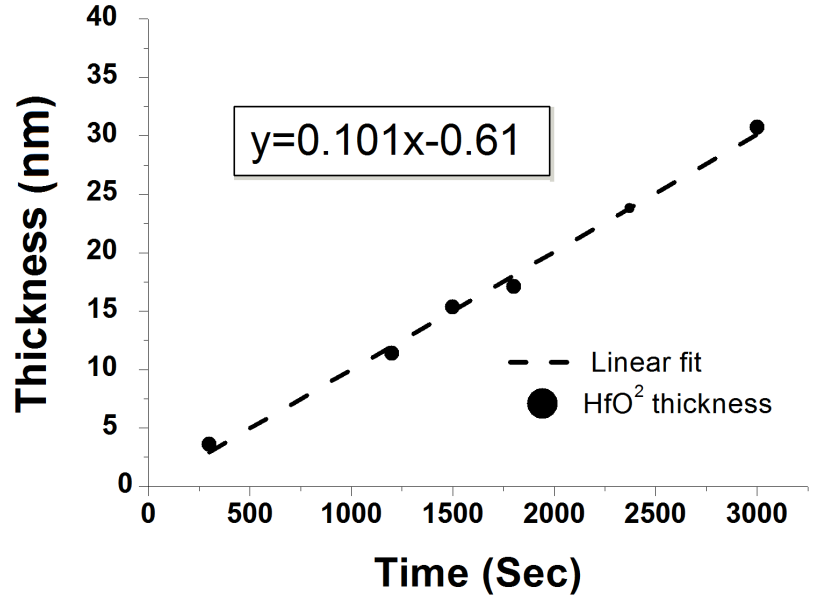

(b)

Figure 2.4: Sputter rates for a) Co and b) HfO_2(base pressure of 10^{-8} torr, working pressure of 5 mtorr , Ar flowrate of 20 sccm, power of 30 W for both the targets, working distance of 150 mm)

$90°C$ for 25 minutes. The sample is then exposed to UV light generated using a Hg source on Karl Suss MA6 system with an exposure dose of 110 $^{mJ}/_{cm^2}$.

The sputtered granular film was topped off with a cap to prevent Co particle oxidation on the top of the film. As a result, if the electrodes are deposited on top of the films, the resistance is very high and the contact area is only on the side of the films through which current can pass. The bottom electrode thickness cannot be more than the thickness of the granular film and it is difficult to do measurement on the same. Therefore, in order to resolve this issue, a three step lithography process is used to deposit top and bottom electrodes as shown in fig.2.5a and the electrical measurements are made by sandwiching the granular film between two metal contacts. The lower metal layer is 10 nm thick, while the top metal is 300 nm in thickness. Either Al or Cr/Au metals are used for the electrode deposition. Au is the actual electrode while Cr helps to improve the adhesion between Si and Au. Cr thickness is usually ~ 15 nm, while Au thickness is ~ 200 nm.

2.3 Characterization

2.3.1 Rutherford Back Scattering

The Rutherford Back Scattering (RBS) experiment is a very useful tool for depth profile and quantitative analysis for different thin films. At a basic level, RBS demonstrates the electrostatic repulsion between high energy incident ions and target nuclei. The specimen under study is bombarded with mono-energetic beam of $4He^+$ particles and the back scattered particles are detected by the detector-analysis system which measures the energies of the particles. During the collision, energy is transferred from the incident particle to the target specimen atoms; the change in energy of the scattered particle depends on the masses of incoming and target atoms.

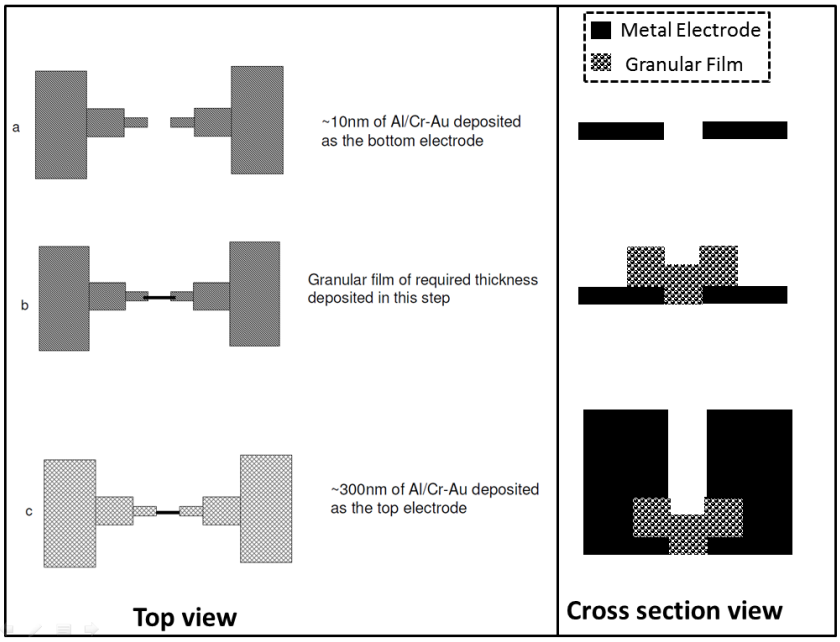

(a)

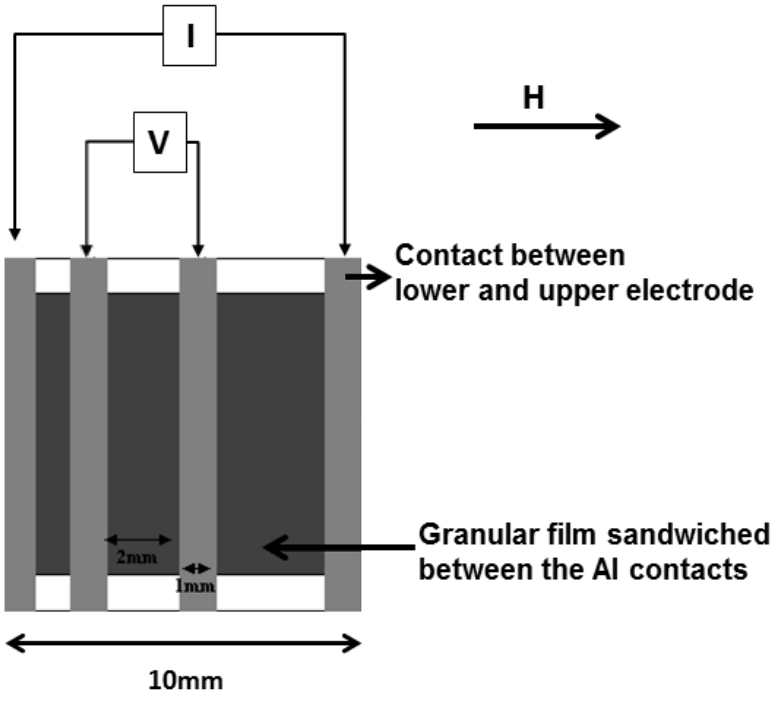

(b)

Figure 2.5: Electrode deposition to counter the high resistivity of granular films and to drive the current through the whole structure a) Photolithography for microdevices b) Bulk film sputtering using shadow mask

The RBS is also weakly sensitive to low mass elements (esp. below oxygen in the periodic table) and it is difficult to get the exact composition for the same [91]. In this research study, a collimated beam of 2 MeV or 500 keV He^+ ions was generated by a 3.5 MV HVE Singletron accelerator and normally incident onto the samples. Back scattered ions were collected and their energy measured simultaneously by two Ortec Ultra silicon solid-state detectors at different scattering geometries. The resultant spectra were fitted using the SIMNRA software [92], and the elemental depth profiles were extracted from a target structure which provides a best fit for the respective spectrum.

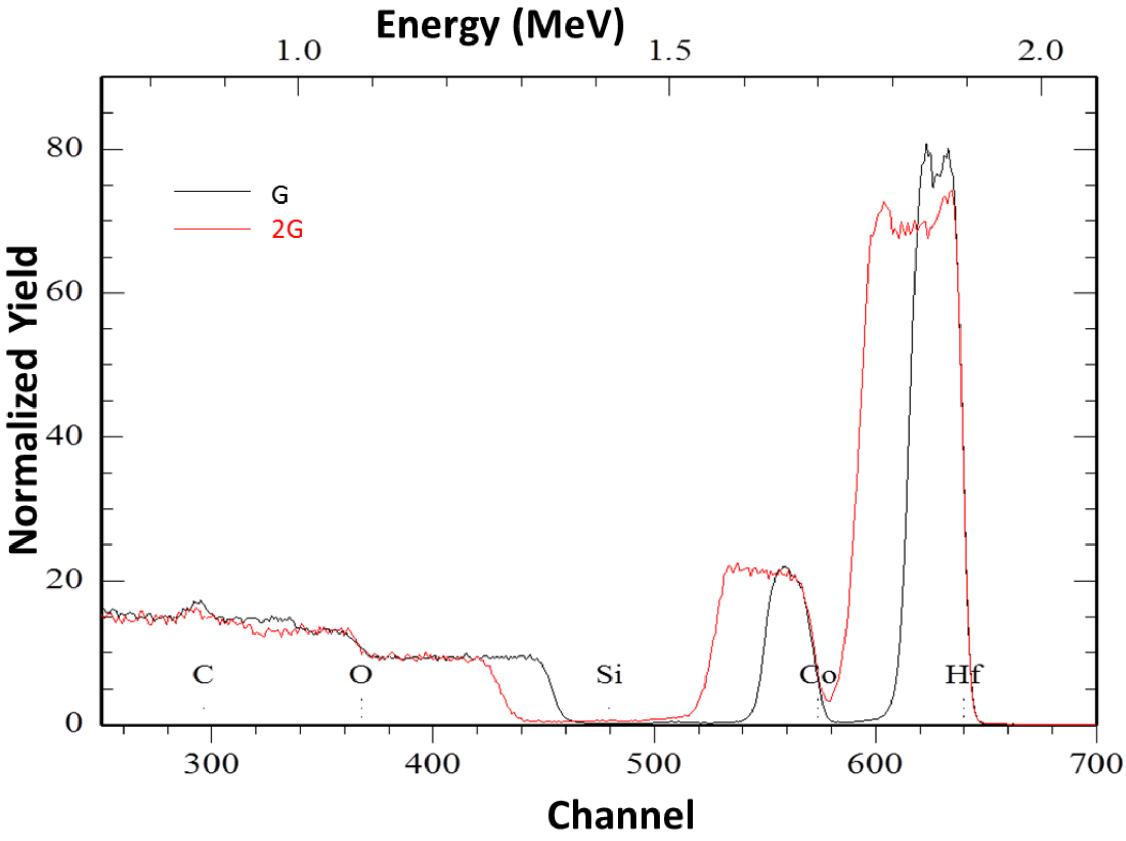

Figure 2.6: Comparison of normalized RBS graphs for sample G (10 bilayer) and 2G (20 bilayer)

The Co-HfO_2 granular films in thesis are fabricated by sequential sputtering and

it was found by earlier experiments in our group that 10 bi-layers of Co and HfO_2 gave the optimum MR ratio at room temperature [74]. In order to understand the film properties and to form the basis for this research study, two films namely structure G and 2G consisting of 10 and 20 bilayers of Co and HfO_2 respectively, were analyzed . The sputtered film compositions for G and 2G were [Co(0.9 nm) $+HfO_2$(1 nm)]$_{10}$ and [Co(0.9 nm) $+HfO_2$(1 nm)]$_{20}$ respectively.

Figure. 2.6 shows the normalized RBS data for sample G and 2G. The obtained data is fitted using the SIMNRA simulation model to determine the elemental composition of the sample (Co, Hf, O and Si) and then the volume fraction of Co is calculated. The fitting is done splitting up the film data from the experiments into three or more physical layers in order to improve the accuracy of the fit. Then, for each layer elemental fit is obtained such that the overall fit still matches the experimental results and the stoichiometry data for each layer is fit to 100 % for the elements. From the RBS data fit the Co volume fraction for both the samples was found to be 42 %. From fig. 2.6 it can be seen that the width of Co and HfO_2 spectrum in sample 2G is approximately twice that of sample G, indicating that the thickness of sample 2G is twice that G, which is expected.

2.3.2 Magnetic measurement

The M-H loops for the sample are obtained using the Vibrating Sample Magnetometer(VSM) tool. In this research work, Lakeshore 7404 VSM is used to measure sample sizes of up to 1cm x 1cm in sweeping fields between ± 12 kOe. The Co-HfO_2 films sputtered in our research group have the same M-H loops for in plane measurements at various angles [74].

Figure. 2.7 shows the M-H loops for samples G and 2G. From fig. 2.7a, it can be observed that magnetic moment of sample at 10 kOe for 2G (~0.65 memu)

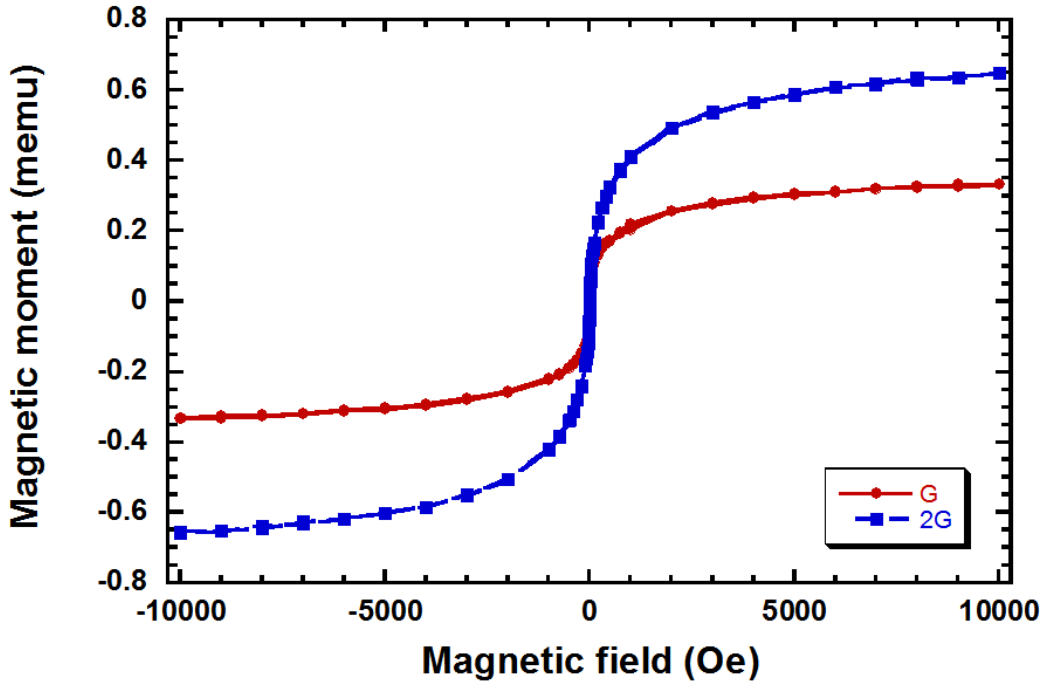

(a)

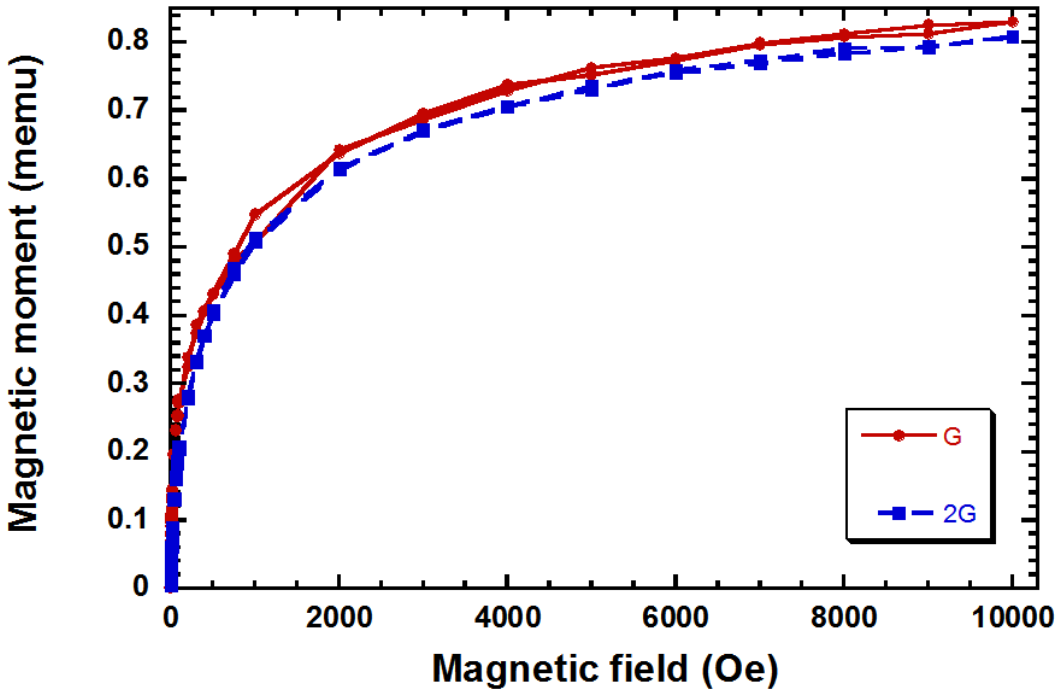

(b)

Figure 2.7: M-H loops at ±10KOe for G and 2G (a) Actual curve (b) Normalized curve

is approximate twice that of G (~0.34 memu). This is because 2G has twice the content of Co in G. However, in order to better understand the difference, the curve is normalized (also called the reduced magnetization curve) with the saturation value moment of Co in the film [82]. It is well known that super paramagnetic systems are characterized by lower coercivity and saturate at extremely large applied fields [6, 25, 29]. Ideally, the shape of the curves should be linear and any deviation is due to the existence of grain size distribution and the extent of deviation from this is a measure of the grain size distribution [82]. It can be observed from the normalized saturation curve (fig. 2.7b) that sample G has slightly higher normalized moment and also sharper $\frac{dM}{dH}$ response when compared to 2G. This refers to the fact that G has larger grain size as compared to 2G. This is also observed by Honda et al. in Fe-SiO_2 systems wherein they changed the volume fraction and found that the sharper response is usually given by films with a larger grain size [6].

2.3.3 Electrical measurement

The bulk granular film measurements are done using 4 probe measurements. As discussed in lithography section, the granular films being highly resistive because of the 5nm oxide cap, the electrical measurements are made by sandwiching the granular film between two Al contacts. The lower layer Al is 10 nm thick, while the top Al is 300 nm in thickness. The shadow mask technique is used to deposit Al contacts on the glass substrate (fig. 2.5b) and the measurement is CIP based measurement.

MR measurements

- **Room temperature measurement**-The transport properties were studied using four-probe DC magnetometer. A constant current of 1 μA is passed

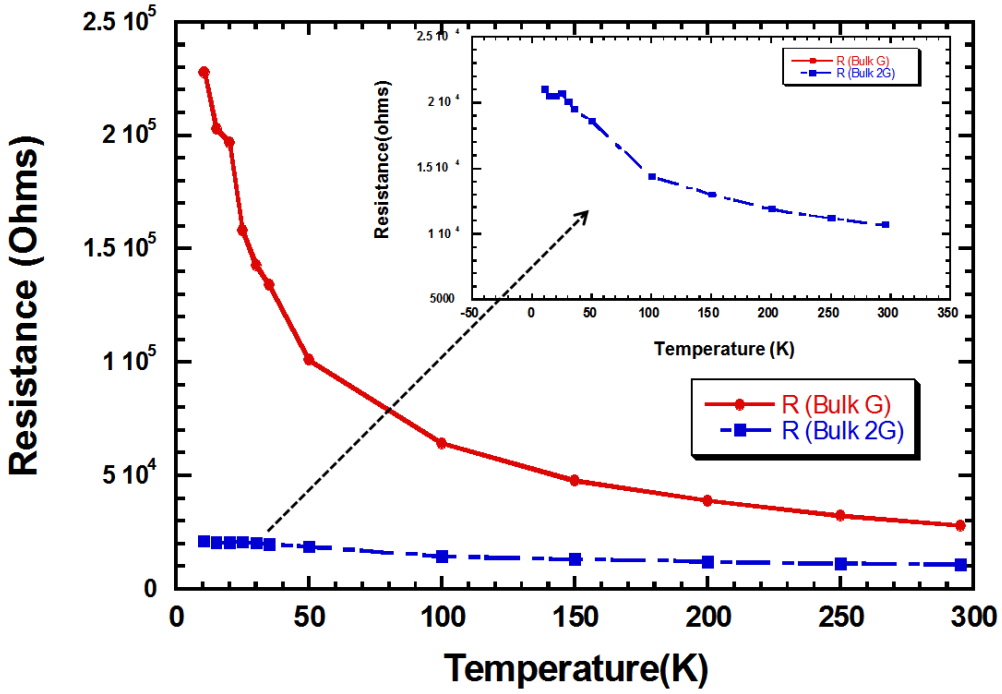

(a)

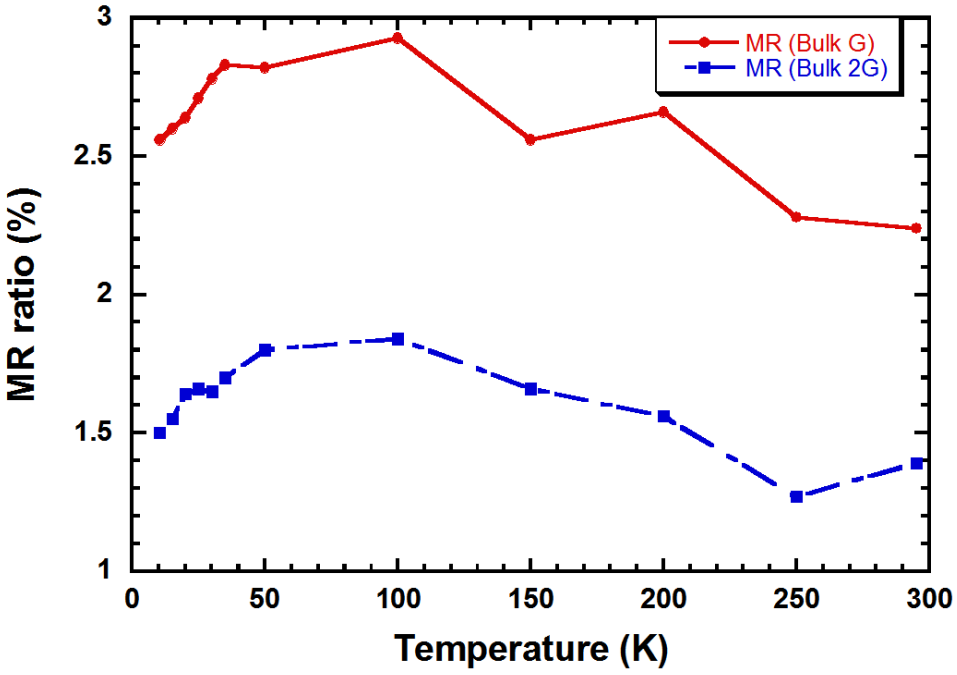

(b)

Figure 2.8: G and 2G a) Resistance vs. Temp (inset shows zoom-in for sample 2G) b) MR ratio vs. Temp

through the sample and the voltage and MR are calculated for the magnetic fields between ±4.2 kOe. Granular films usually have a high saturation magnetization ~ 6 Tesla [74]. However the minor hysteresis loop for an applied field of ±4.2 kOe follows that of ±12 kOe and higher fields. Hence, it is reasonable to compare the MR ratios for the various samples measured between ±4.2 kOe. The MR ratio is calculated as

$$MR = \frac{R_{max} - R_{min}}{R_{max}} \tag{2.1}$$

where R_{max} and R_{min} are resistances at zero and maximum field respectively.

- **Low Temperature measurement** - For low temperature measurements, a Oxford closed cycle cryostat CCC1200 is used and it is capable of achieving temperatures as low as 10K. The samples have to be wirebonded on to a leadless chip carrier and then loaded onto a holder, which is then inserted into the cryostat. After cooling down the system to the required temperature, measurements are made in magnetic fields between ±4.0 kOe. Fig. 2.9a shows the schematic of the CCC-1200 cryostat showing its main components. The block diagram in fig. 2.9b shows the connections and placement of the sample with respect to the magnets. The holder supports both in-plane and out-of-plane configurations and also allows the angle between the magnetic field and sample to be varied in both the configurations.

As explained earlier, the resistance and MR curves are important in understanding the electrical properties of granular films. Figure. 2.8 shows the variation of resistance and MR with temperature as well as some of the MR curves measured at 300 K, 100 K, 20 K and 10.6 K. Figure. 2.8a shows resistance trend for bulk samples G and 2G respectively. Sample 2G has twice the number of bi-layers as G and hence

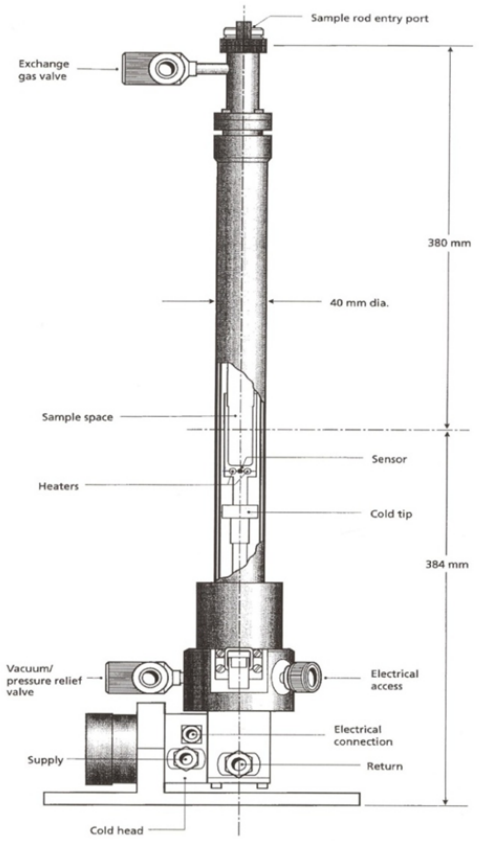

(a)

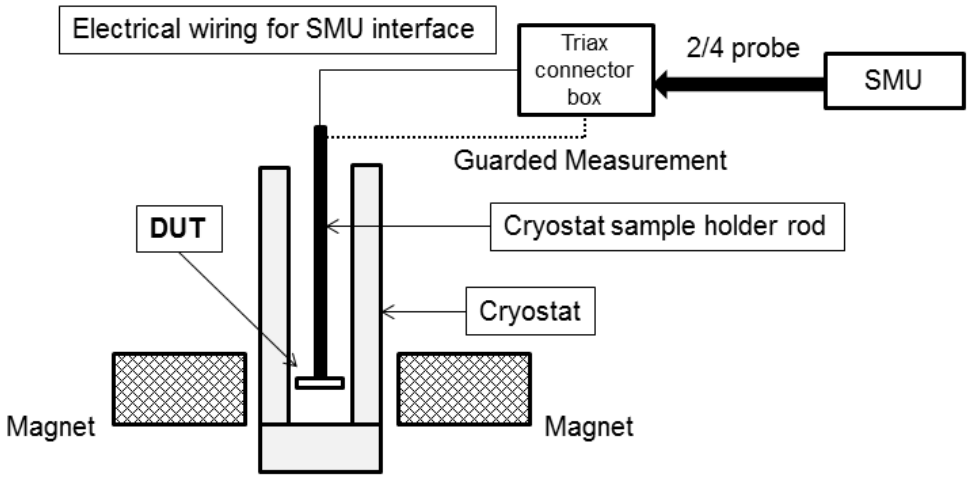

(b)

Figure 2.9: Low temperature measurement setup a)Schematic illustration of CCC1200 cryostat [93] b)Schematic of low temperature electrical measurement setup

twice in thickness and the observed resistance trend with temperature is smaller for 2G than G. Granular systems with larger grain size along the conduction have lower resistance [6, 74]. From the normalized M-H loop shown in fig. 2.7 it can be seen that 2G has comparatively smaller grain size compared to G. Therefore the only possibility for lower resistance of 2G is due to the presence of additional conduction paths as compared to G. This is in accordance with the previous results on granular films as well as experiments done in our group for Co-HfO_2, wherein an increase in thickness leads to additional number of available tunneling paths and hence lower resistance [74, 83].

As far as the MR ratio is concerned it is higher for G than 2G at all temperatures (fig. 2.8b). A general trend which is observed is that the MR increases with decrease in temperature for both the curves. The MR ratio generally varies with temperature because of various spin-flip processes which will scatter the electrons. The spin-flip process may arise from the impurity states or the excitation of bulk magnons. Decreasing temperature will make the probability of spin-flip scattering decrease so as to increase the maximum MR ratio [59]. From the normalized M-H loop in fig. 2.7b it can be seen that G has bigger grain size compared to 2G. In MR measurements, presence of larger grains along the conduction helps to improve the MR ratio as these grains align easily to the direction of applied field compared to smaller grains [6] and hence enhance spin-dependent tunneling. Therefore from the MR results and M-H loops, it can be observed that G has higher MR and comparatively larger grains along the conduction path. This is also reflected in the MR curves plotted in figs. 2.10 & 2.11. It can be seen from these figures that G not only has higher MR ratio but also a higher switching field compared to sample 2G at all temperatures. The grains in the granular films are single domain particles but since they are smaller than 10 nm, the thermal energy (k_BT) overcomes the

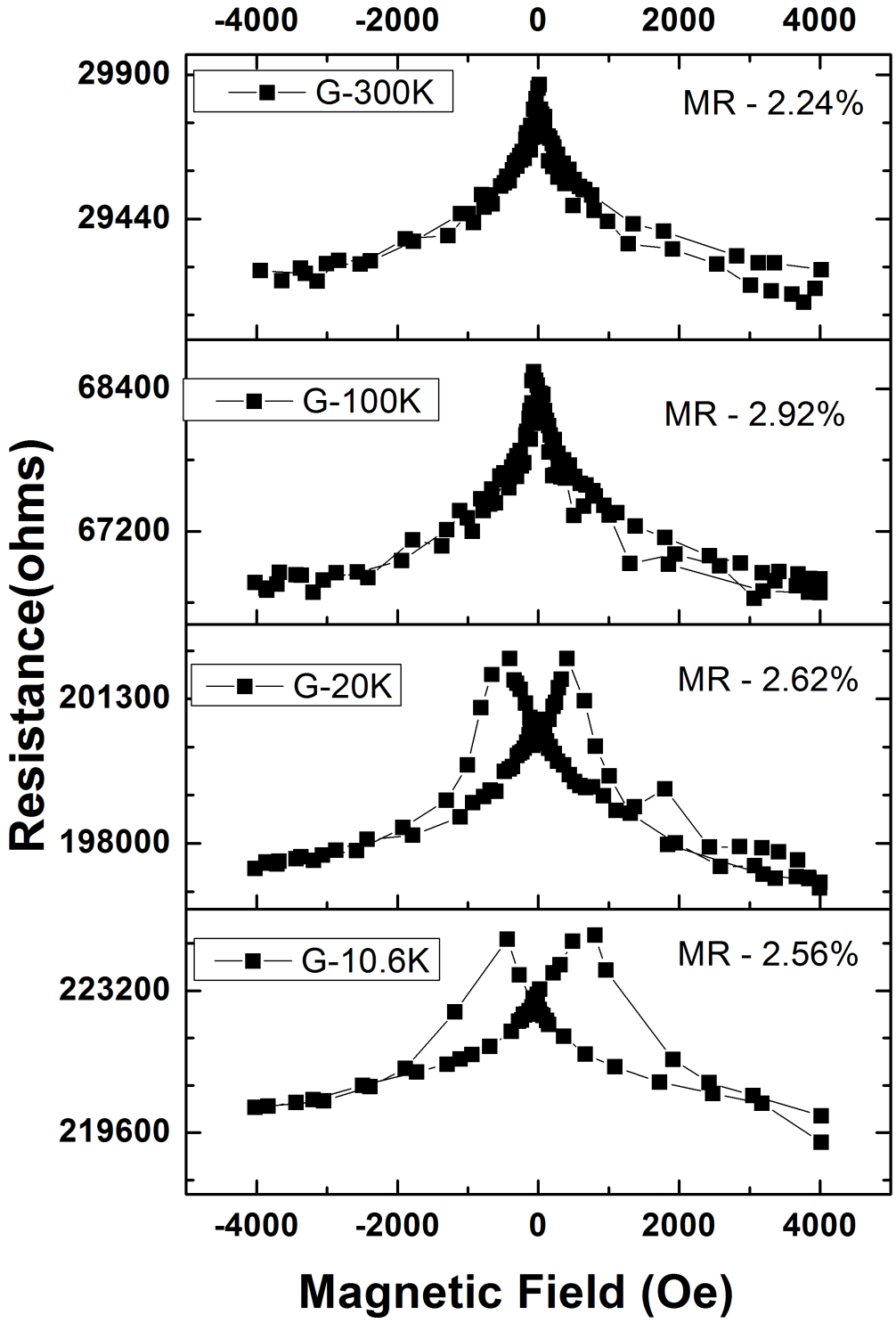

Figure 2.10: MR curves for Samples G at T=300K, 100K, 20K and 10.6K

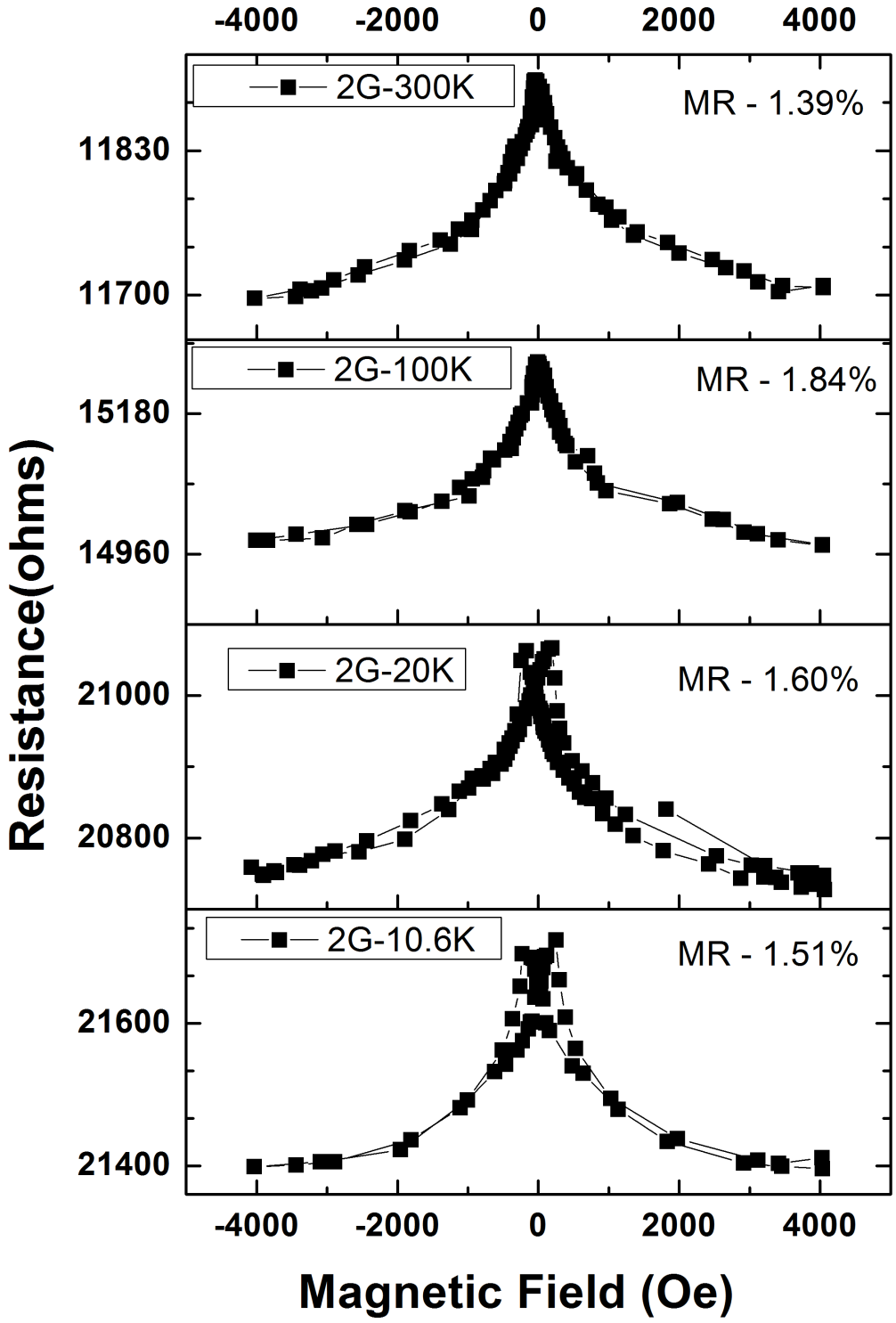

Figure 2.11: MR curves for Samples 2G at T=300K, 100K, 20K and 10.6K

anisotropy energy (K_uV) at room temperature making them superparamagnetic [9, 77, 79]. So as temperature decreases, the larger grains start blocking earlier as compared to smaller grains. The MR curves of sample G show higher switching field compared to 2G indicating the fact that G has far more larger grains along the conduction path, verifying the observation based on the shape of the M-H loop. For temperatures below ~100 K, it can be seen that the samples G and 2G both show a decreasing trend of MR with temperature. This is due to the blocking (T_B) of the grains and exchange interaction [6]. Below blocking temperature the grains start behaving like single domain particles and no longer align easily to field, leading to reduction in MR.

From the blocking temperature, the approximate. grain size can be calculated using

$$V_c(T) = \frac{25k_BT}{K_u} \tag{2.2}$$

where k_B,T and $K_u = 4.5 \times 10^6 erg/cc$ are the Boltzmann constant, the temperature and the anisotropic constant for bulk Co respectively [77, 79]. Substituting the various values and value of T_B as 100, the mean grain size of Co is estimated to be approximately 6 nm for both the sample G and 2G. The value is similar for both the samples because the T_B measured using this method is not accurate. However, it is difficult to observe Coulomb Blockade for films with large grain size. Coulomb Blockade is of interest as it gives rise to higher order tunneling characteristics and improved MR ratio at lower temperatures [94].

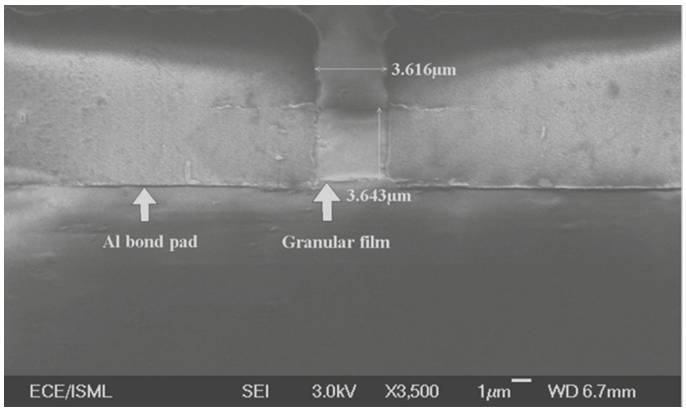

Figure 2.12: SEM image of the microdevice using 3-step lithography process showing device dimension of 3.6 μm × 3.6 μm

2.4 Microdevices based on standard structures

The previous section dealt with the bulk film characteristics. In this section we discuss microdevices based on these films. The length of the bulk structure is approximately 1 cm while that of the microdevice is 3 μm . If the approximate grain size and separation are assumed to be 4 nm and 1 nm respectively, the number of grains along the length of the bulk structure is ~2×10^6 while it is ~7×10^2 for the microdevice. There is ~ 4 orders of difference in magnitude for the number of grains between the bulk and the microdevice. Hence it is essential to study microdevices based on these films. The approximate size of the active device region for the microdevices is 3.6 μm × 3.6 μm for CIP devices as shown in fig. 2.12. The electrical measurements are done on the microdevices and the results are analyzed.

Figs. 2.13 & 2.14 shows the resistance and MR trends for samples G and 2G for bulk and microdevice. It can be seen that the behavior of the microdevice is different from that of the bulk which is expected as the conduction channel in a microdevice is more restricted. The resistance of the microdevices are identified to be higher than that of the bulk films for both the samples. The variation of MR ratio with temperature for the microdevice is higher than that of the bulk.

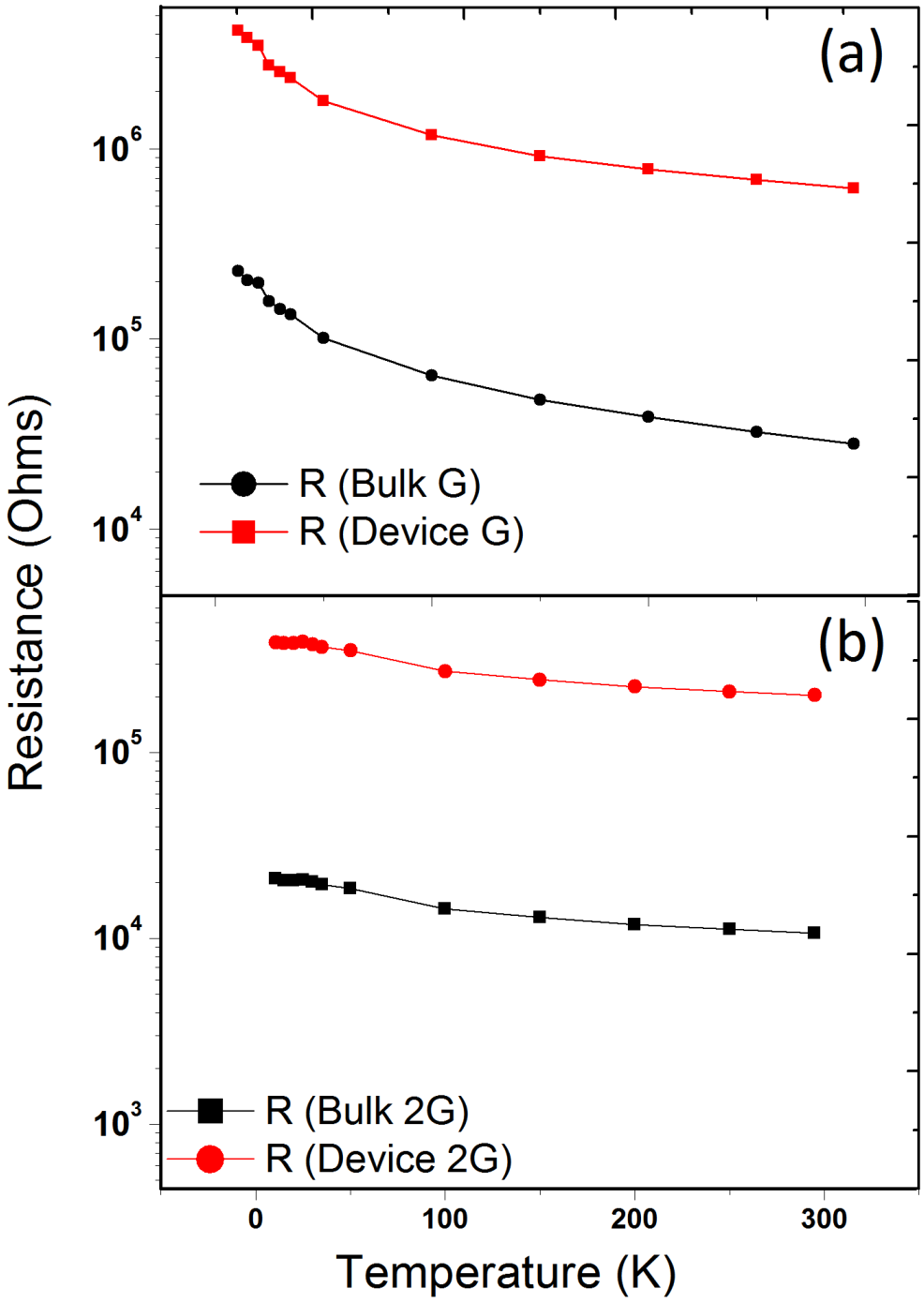

Figure 2.13: Resistance variation with temperature for Bulk and microdevice a) Sample G b) Sample 2G

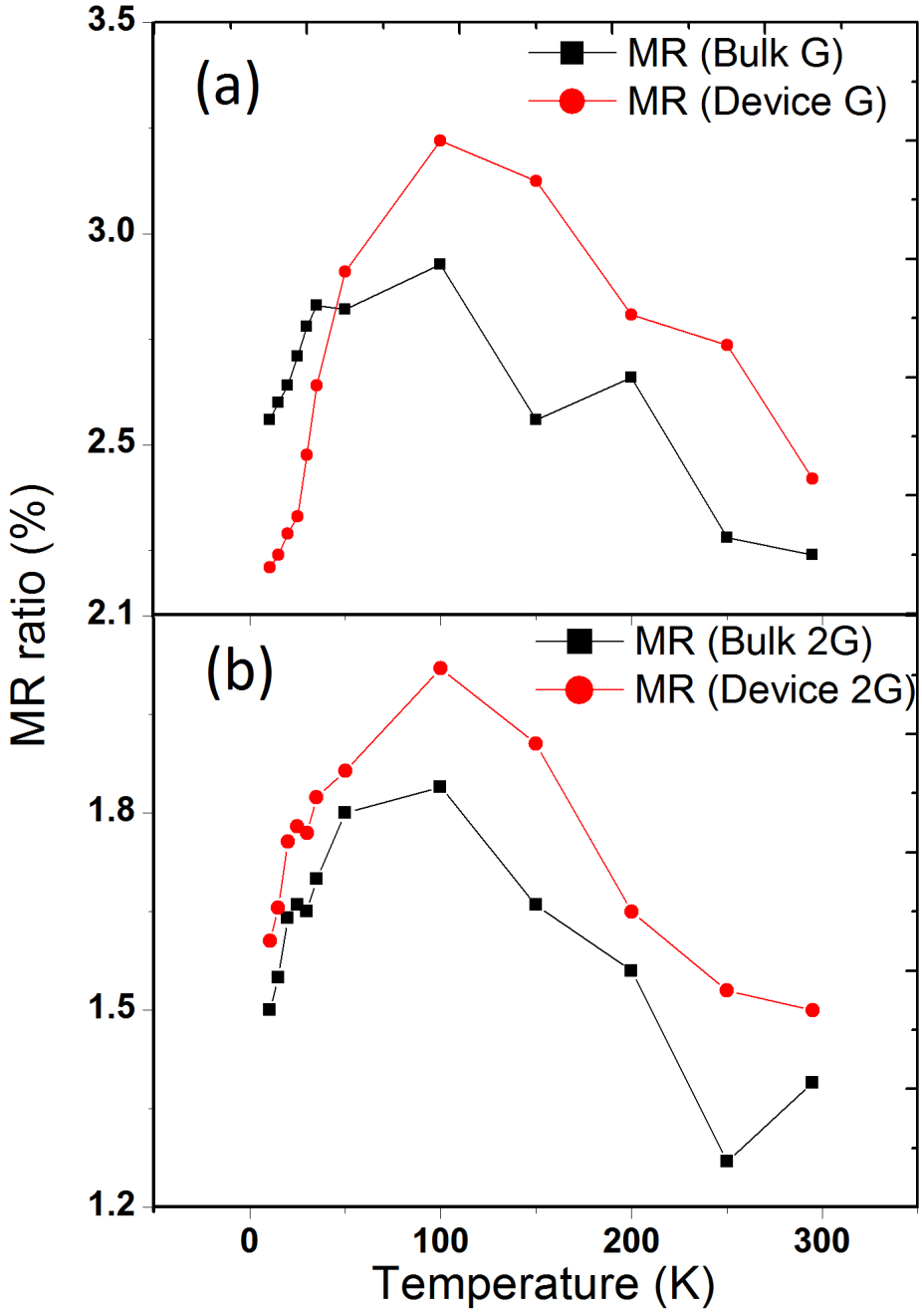

Figure 2.14: MR ratio variation with temperature for Bulk and microdevice a) Sample G b) Sample 2G

From these two observations, it can be concluded that the number of grains taking part in the conduction is different for bulk and microdevices. This verifies that the difference in number of the grains between the bulk and microdevice will have an effect on MR and resistance. The bulk as well as the microdevice shows a decrease in MR below the blocking temperature (100 K). As explained earlier this is due to the blocking of the single domain particles at temperatures less than 100 K [6]. In the case of structure G, the decrease in MR below 100 K is steeper for the device than the bulk as the microdevice has lower number of tunneling paths compared to the bulk and hence the drop in MR due to blocking is more apparent. The 2G based microdevice structure clearly does not show this property because the number of tunneling paths is higher compared to G and hence it is less affected by blocking.

Figure. 2.15 shows the MR curves for the bulk and microdevices for samples G and 2G. It can be seen that sample G and 2G have different switching fields because of the difference in grain sizes in the samples which take part in the conduction. The bulk and microdevices have similar switching fields reflecting the fact that the grain size distribution along the conduction path are similar for both the bulk and microdevices.

2.5 Summary

The granular films were fabricated using sequential sputtering and the properties of bulk and microdevices based on these films were analyzed. Sample G which consisted of 10 bilayers of Co and HfO_2 is found to be optimum in terms of MR ratio as opposed to sample 2G consisting of 20 bilayers of Co and HfO_2. The performance of microdevices is better in terms of MR ratio, although they showed higher resistance as compared to bulk films. In general, the restriction of tunneling paths and the thickness of the films plays an important role in engineering MR

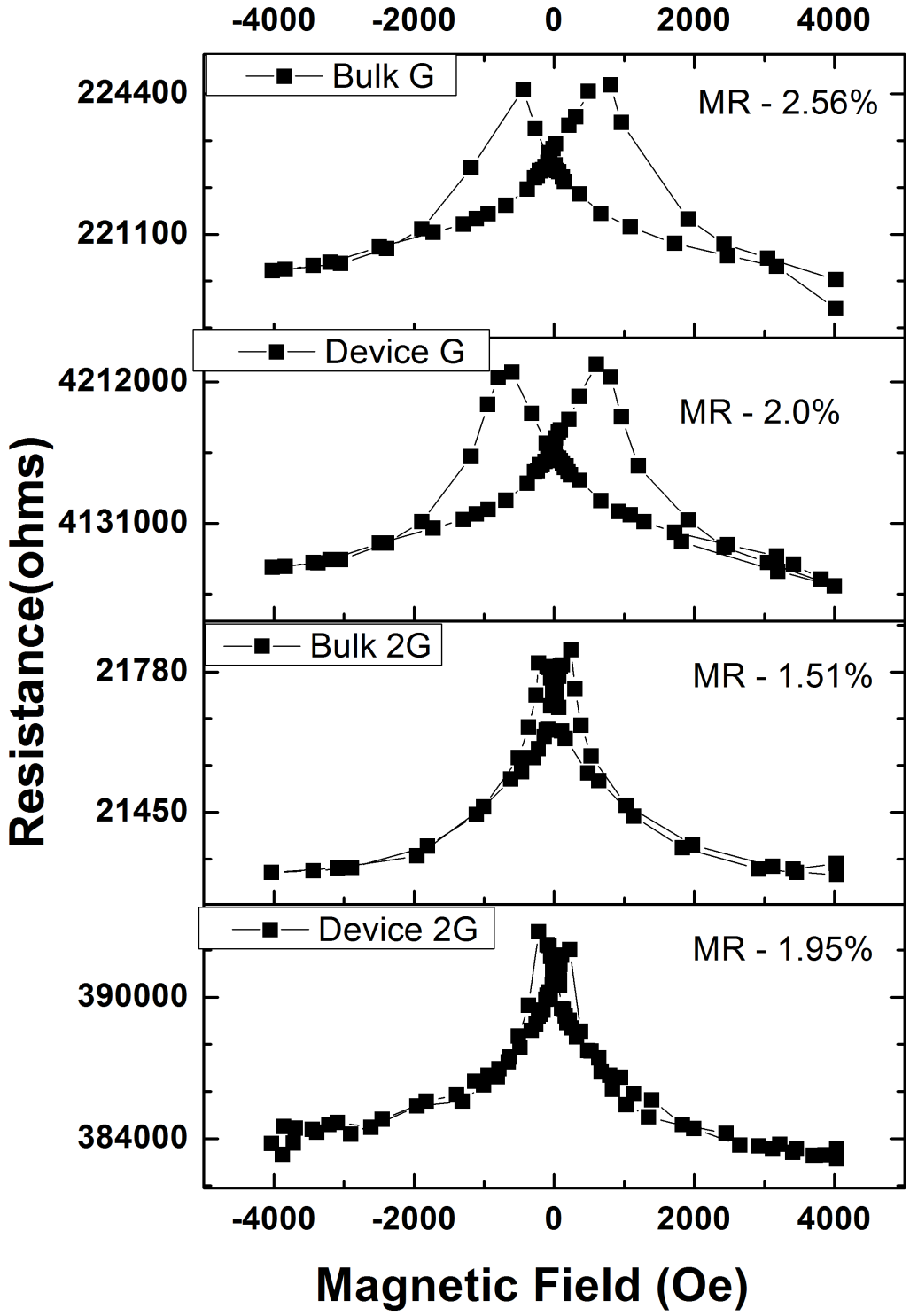

Figure 2.15: MR curves for Bulk and microdevice at 10.6 K

and resistance. With sample G and 2G as reference structure, a device structure in proposed in Chapter 3 to indirectly control the grain size by changing the roughness of the films.

Chapter 3

CIP devices based on insertion of oxide layer in Co-HfO_2 granular films

In Chapter 2, the fabrication and characterization of the standard granular films namely G and 2G are studied and it is found that sample G gives the best MR ratio. It has also been found that the M-H loops for structure G and 2G are different, indicating the fact that the two structures have different grain size distribution [6, 82]. Therefore, the grain size distribution varies with thickness and it affects the resistance and MR value. It would be of interest to control the grain size distribution and hence the electrical properties of such films. The grain growth and nucleation are dependent on the roughness of surface on which the films are grown. Therefore, in this chapter roughness is made use of to control the grain size distribution. This is done in a controlled manner with the help of an oxide insert. The change in roughness will affect the grain size distribution and possibly help observe Coulomb Blockade (CB) like characteristics provided grains along the conduction path are small enough. This chapter discusses in depth the fabrication

and characterization of micro devices based on different thickness of the oxide insert (and hence different roughness). We intend to observe the grain size variation introduced by the inserted oxide layer and study the change in properties in such films. The electrical measurements made in this chapter are current in plane (CIP) measurements. In this chapter, the volume fraction of Co is reduced in order obtain smaller grain sizes and hence observe possible CB.

3.1 Proposed structure: Bulk films - Insertion of oxide layer

As described earlier, simulation models for granular films predict that the magnetoresistance (MR) ratio remains constant with thickness [25, 82]. However, experimental research done on granular films, including the results presented in the previous chapter, do not reflect this trend. This can be explained based on the fact that the grain size and number of tunneling paths in these films change with thickness [48, 80, 83].

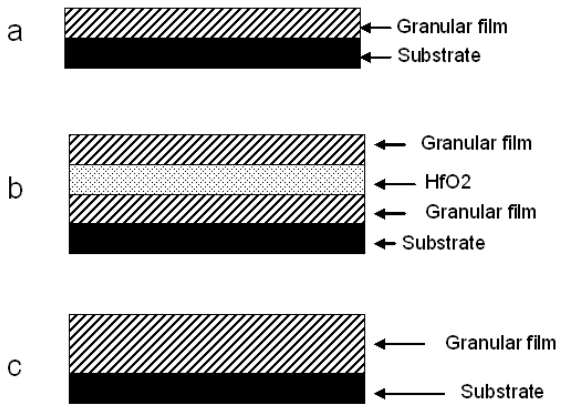

Figure 3.1: Illustration of granular film structures a) Sample G (10 bilayers of Co and HfO_2) b) Proposed structure (10 bilayers of of Co and HfO_2+ HfO_2 +10 bilayers of Co and HfO_2) c) Sample 2G (20 bilayers of Co and HfO_2)

In this chapter, an oxide layer (HfO_2) is inserted at the center of structure 2G,

which splits it into two granular films of equal thickness separated by the oxide layer. Hafnium oxide is chosen as the insert so as to make sure that the films are homogenous in nature in terms of the oxide used. Since similar substrates are used for growing the films, the bottom granular film would have the grain size distribution same as that of sample G whereas the top layer grain size distribution will depend on the roughness of the inserted HfO_2 layer. The overall Co content in the proposed structure is same as structure 2G, while that in each of the top and bottom layer is same as structure G. It is already known that structure G has the best MR and the idea of inserting an oxide into 2G, is to make the structure 2G similar to G in terms of thickness i.e. two G structures separated by the oxide layer.

The thickness of the oxide inserted is varied from 1.5 nm to 15 nm. Figure 3.1 shows the proposed structure along with structures G and 2G. The compositions of the various device structures are given in table 3.1. The devices are fabricated as discussed in the previous chapter (fig. 2.5) using the 3 step lithography process.

Table 3.1: Granular films of standard thickness (G and 2G) and the proposed structures

Sample	Composition
G	$[Co(0.7\text{ nm}) + HfO_2(1.1\text{ nm})]_{10}$
2G	$[Co(0.7\text{ nm}) + HfO_2(1.1\text{ nm})]_{20}$
X_n	$[Co(0.7\text{ nm}) + HfO_2(1.1\text{ nm})]_{10}$ + $[HfO_2(n)]$ + $[Co(0.7\text{ nm}) + HfO_2(1.1\text{ nm})]_{10}$ where n=1.5, 3, 5,10 and 15 nm respectively

Rutherford Back Scattering (RBS) is used for compositional analysis and to verify the multilayer structure. Figure. 3.2a shows the RBS data for sample X_{15nm} which is fitted using SIMNRA modeling software to the possible elements found in the sample (Co, Hf, O and Si) and thereafter volume fraction of Co and HfO_2 is calculated. Points A and B on the figure show Co content in the top and bottom layer respectively whereas C and D show the content of Co and Hf layer in the

central layer .

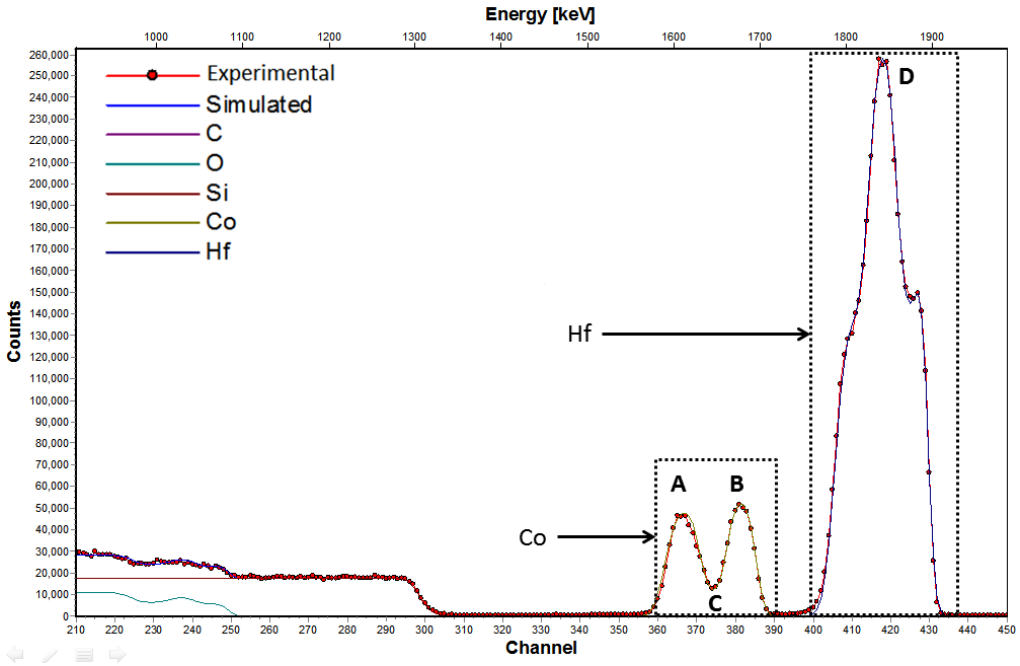

(a)

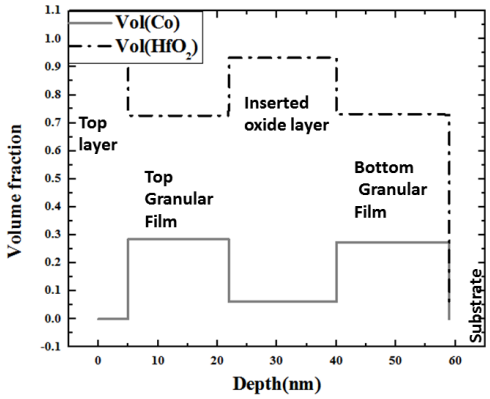

(b)

Figure 3.2: a) RBS data for X_{15nm}: Markings A,B,C corresponds to Co content in bottom,top and center of the film respectively while D represents the Hf composition across the multilayer (peak showing the content in the central layer) b) Volume fraction vs. depth profile

The fig. 3.2b shows the variation of volume fraction of Co and HfO_2 (calculated from the fitting) with depth and it can be seen that the average Co volume fraction for the sample is 27 %. Although the central oxide is continuous, it has ~7 % of Co

in that central layer. This is due to formation of Co atomic clusters in the central layer during sputtering. Maurice et al. have found such clusters in their Cobalt Alumina films prepared by sputtering [27]. They first deposit 3 nm of alumina layer, followed by 0.2 nm to 2nm of Cobalt and then finally 4 nm of alumina layer on top. They found that Co formed small atomic clusters which was not detected by electron microscopy.

3.2 Grain size and roughness

As described in Chapter 1, some of the techniques used to find the particle size/distribution of granular films are TEM and SAXS. However, SAXS requires thicker samples of ~100 nm or greater to give consistent and reliable results. Our samples had a thickness of less than 40 nm for the active granular film layer and SAXS measurements were not successful. TEM which is based on atomic number (Z) contrast, failed to give any conclusive evidence for the samples because of the close atomic numbers (Z) of Co (Z=27) and HfO_2 (Z=29.33)[1]. Similar issue was reported by Kim et al. [88] for Co-Cu granular films because of the close atomic numbers of Co and Cu, and hence they employed alternative techniques based on M-H loop and ZFC/FC measurement to find the grain size distribution. In this chapter ZFC/FC measurements are used to find the grain size for the various samples. The results are corroborated using the simulation model discussed in Chapter 4 which also helps in obtaining the relative grain size distribution for the samples.

In this chapter, applied field ($H_{applied}$) of 10 Oe is used to obtain the ZFC/FC curves. A 'Quantum Design' SQUID magnetometer having a sensitivity of 10^{-7} emu, equipped with a 5.5 T super-conducting coil and working temperature range of 4 K to 300 K is used in this study.

[1] Avg Z (HfO_2)=[Hf(Z=72)+2×O(Z=8)]/3=29.33

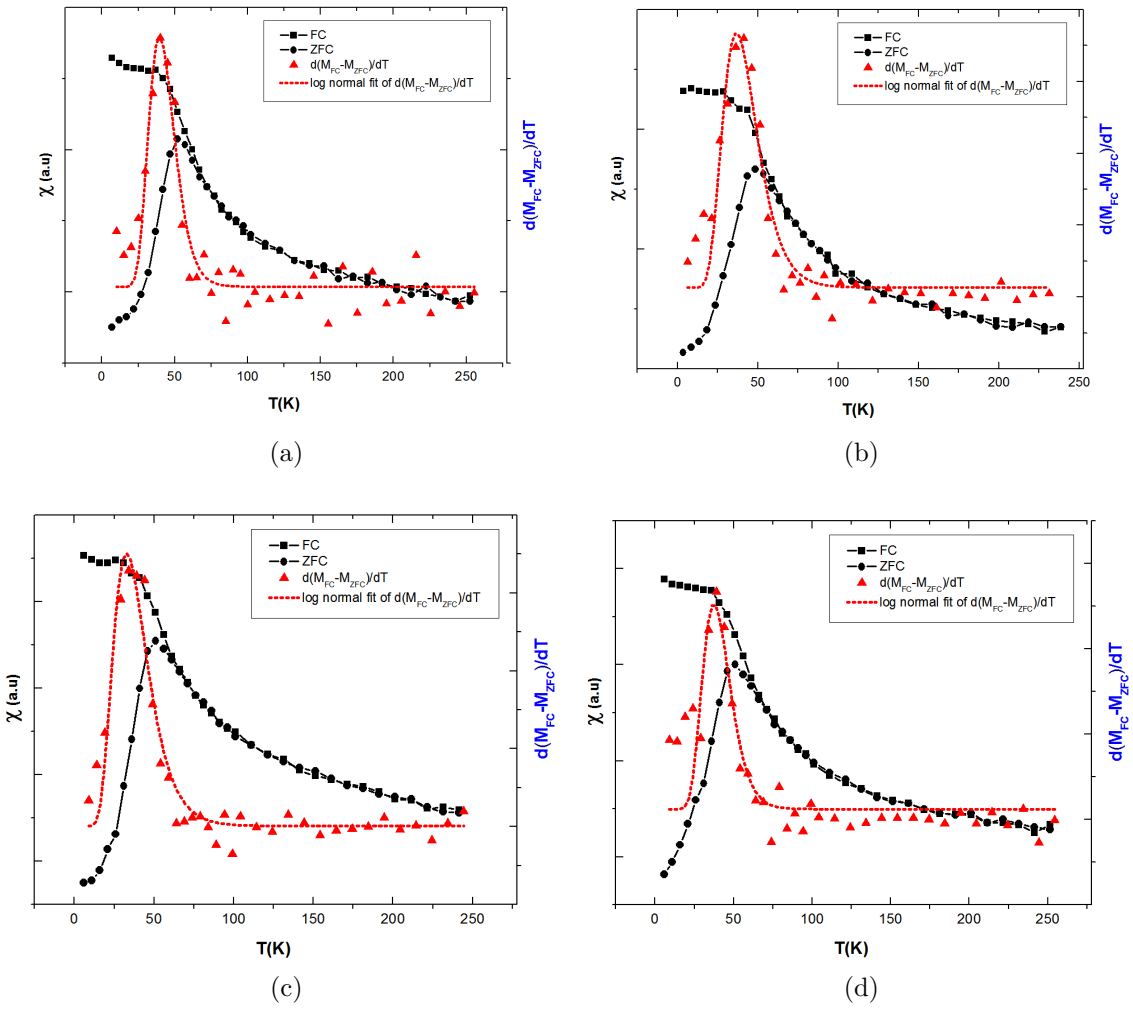

Figure 3.3: T_B calculation from FC/ZFC curves a) G, b) 2G, c) $X_{1.5nm}$ and d) X_{3nm})

Using the method described in section 1.2.4 of Chapter 1, grain sizes are obtained for the samples as shown in Figs. 3.3 & 3.4. The grain sizes distribution are obtained for all the samples using this method and tabulated in table 3.2. It can be seen that T_B and its spread (hence the grain size) is different for all the structures. As seen from fig. 3.5a, the value of T_B is lowest for $X_{1.5nm}$ followed by X_{3nm} , 2G, G, X_{15nm},X_{10nm} and X_{5nm}. However the highest spread is for $X_{1.5nm}$ followed by X_{3nm}, 2G, X_{10nm}, X_{5nm},X_{15nm} and G.

In order to understand the grain size distribution, top surface roughness mea-

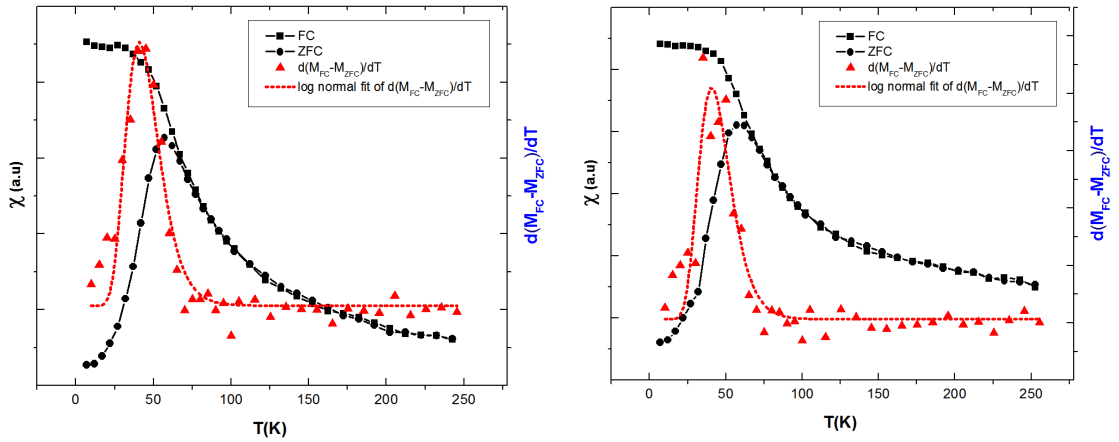

(a) (b)

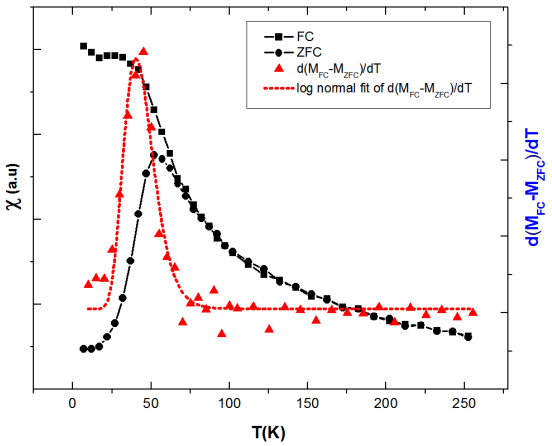

(c)

Figure 3.4: T_B calculation from FC/ZFC curves a)X_{5nm}, b) $X_{10nm}$and c) X_{15nm})

surements are done on the samples. Atomic force microscopy is used to measure the surface roughness of the samples. There is an increase in roughness from G to $X_{1.5nm}$ and then it decreases monotonically to X_{15nm}. Figure. 3.5a shows the variation of spread (T_B) and grain size diameter for all the structures, while fig. 3.5b shows the roughness trend for the various structures measured using AFM. Figures. 3.6 a, b & c shows sample AFM images for G, 2G and $X_{1.5nm}$. It can be seen that when 1.5 nm of oxide is inserted into sample 2G, there is a increase in roughness from 0.81 nm to 1.17 nm due to the discontinuity of the insert. As the

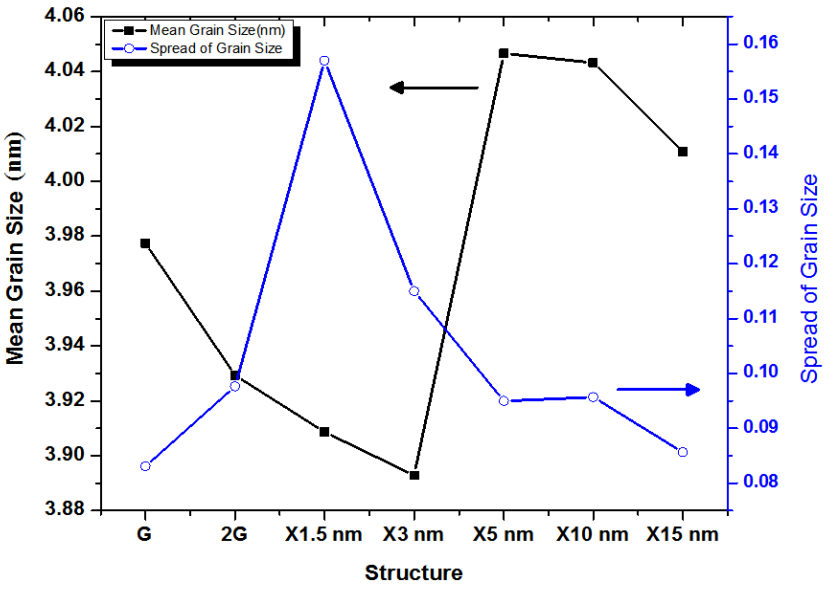

(a)

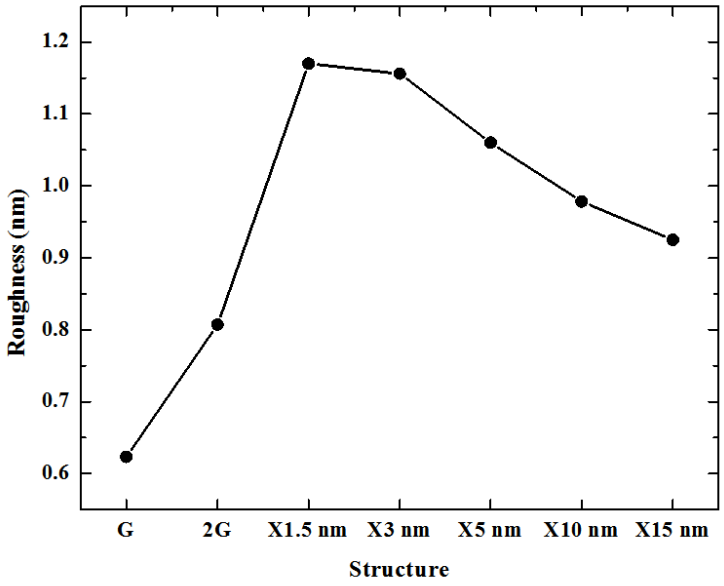

(b)

Figure 3.5: Grain size and roughness for the fabricated granular film structures a) Grain size and spread obtained using the FC/ZFC discussed in Figs. 3.3 & 3.4 b) Roughness of the top of the granular film for the various structures obtained using AFM measurements

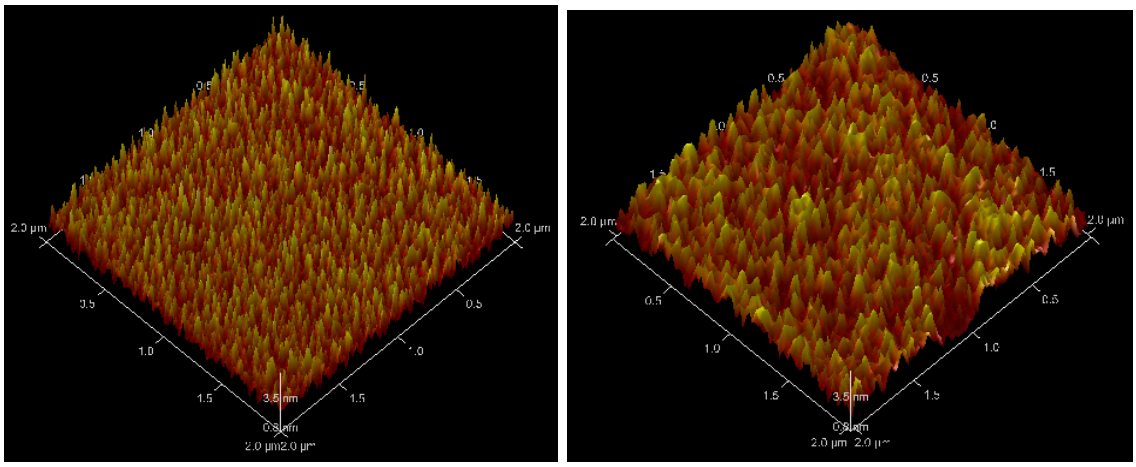

(a) (b)

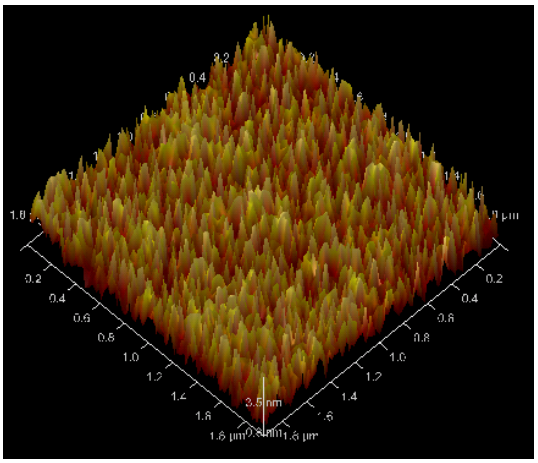

(c)

Figure 3.6: AFM image of scan size 2 μm x 2 μm for a) G (roughness ~0.62 nm) b) 2G (roughness ~0.81 nm) c) $X_{1.5nm}$ (roughness ~1.17nm)

thickness of the insert is increased to 15 nm, there is a monotonic drop in roughness from 1.17 nm to 0.93 nm. This can be explained based on the fact that the oxide layer becomes smoother with increasing thickness. For oxide thickness of 1.5 nm, the insert is highly discontinuous and provides a very rough surface for the top film deposition. This leads to the formation of Co grains with higher spread as evident from the FC/ZFC measurement. As the thickness of the insert is increased to 3 nm the roughness reduces as the film becomes more continuous leading to a decrease in grain size and spread. As the thickness is further increased the roughness re-

Structure	T_B distribution (K)		Grain diameter (nm)		Roughness (nm)
	μ	σ	μ	σ	
G	38.79	0.21	3.97	0.07	0.62
2G	37.54	0.31	3.93	0.10	0.81
$X_{1.5nm}$	35.84	0.41	3.88	0.14	1.17
X_{3nm}	36.82	0.25	3.91	0.08	1.16
X_{5nm}	40.6	0.29	4.03	0.10	1.06
X_{10nm}	40.4	0.27	4.02	0.09	0.98
X_{15nm}	39.7	0.26	4.00	0.09	0.93

Table 3.2: T_B and grain size obtained using the FC/ZFC measurement along with top surface roughness for the various structures

duces even further forming the basis for formation of uniform grain sizes with lower spread.

There is a significant change in grain size when the insert thickness is changed from 3 nm to 5 nm and it indicates the transition from discontinuous to continuous nature of the inserted oxide layer. When the inserted layer thickness is increased to 5 nm, there is decrease in grain size spread as there is a reduction in overall roughness. However, the average grain size increases, which can be explained based on the fact that the inserted layer becomes continuous and forms a good base for grain growth. As the inserted layer thickness increases the grain size increases while the spread decreases long with the roughness. Thus, there are two different regimes affecting roughness because of the inserted oxide layer -

a) Discontinuous inserted layer sizes and hence observe possible CB.

b) Continuous inserted oxide layer.

3.3 Understanding interactions present in the fabricated structure

In 2002, Kechrakos and Trohidou suggested that inter-granular interactions play an important role in the magnetic configuration of the film [65]. They found that the uni-axial anisotropy energy of the granules and their dipolar interaction determined the magnetic property of the film. In this chapter, the Curie-Weiss law [55, 95, 96] is employed to find the type and extent of the interactions.

The superparamagnetic particles generally follow the Curie's law given by

$$\chi = {}^{C}/_{T} \tag{3.1}$$

where χ is the initial susceptibility, C is the Curie constant and T is the temperature. However, it is observed that if interactions are present in the films, the equation 3.1 has to be modified to obtain the Curie Weiss law given by

$$\chi = {}^{C}/_{(T+\theta)} \tag{3.2}$$

where the additional term θ is the Weiss constant [54, 55, 95, 96], which defines the extent of the interactions in these films. Thus, the plot of initial susceptibility vs. temperature can be used to deduce the type of interaction in granular films. The fitting of the linear regime of $\frac{1}{\chi}$ vs. T helps obtain the value of θ (fig. 3.7a). The positive θ values show the presence of antiferromagnetic interactions whereas negative values indicate the presence of ferromagnetic interactions.

There are numerous research articles which show that θ is proportional to the dipolar energy [38, 82, 97]. Chantrell and Wohlfarth theoretically analyzed the factor θ and found that it represents the strength of inter-particle interactions [95]. The factor θ has dimensions of temperature and its effect can be understood as a

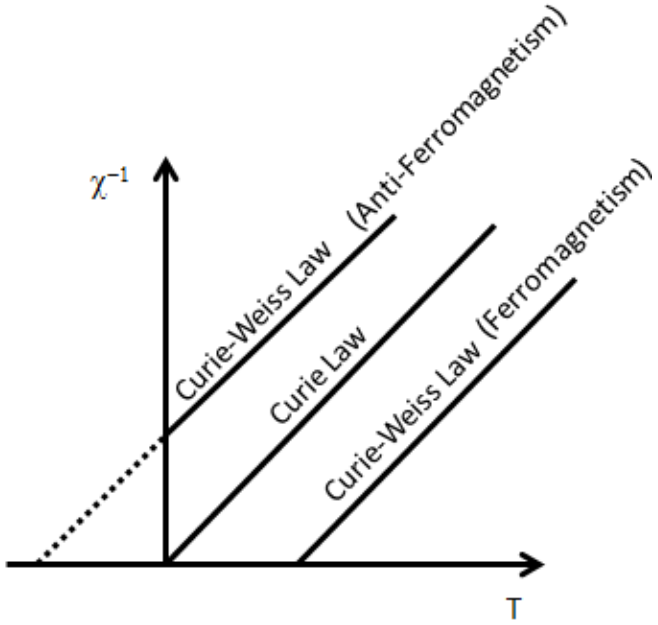

(a) Curie and Curie Weiss Law (interactions)

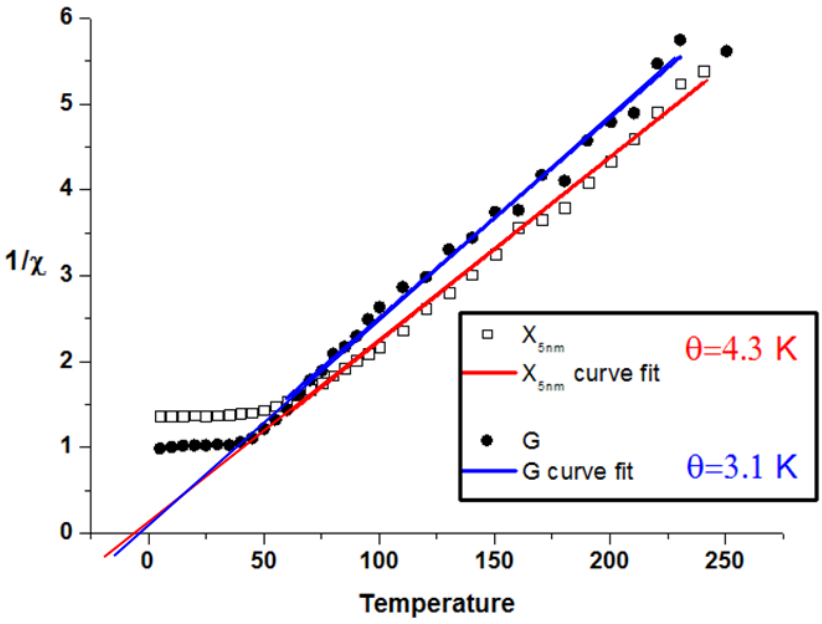

(b) Initial Susceptibility vs. Temperature for G and X_{5nm}

Figure 3.7: Deducing interactions using Curie Weiss Law

Structure	θ (K)
G	3.1
2G	2.8
$X_{1.5nm}$	3.8
X_{3nm}	3.1
X_{5nm}	4.1
X_{10nm}	4.9
X_{15nm}	4.7

Table 3.3: Weiss constant θ for the proposed structures

dipolar field exerting a disordering or ordering torque on the magnetic moments of the particles, depending on whether it is anti-ferromagnetic or ferromagnetic in nature. This effect of this factor changes with the applied magnetic field as well as temperature.

Sample plots of initial susceptibility vs. temperature for G and X_{5nm} are shown in fig. 3.7b. The linear region of the susceptibility plot gives the equation from which the θ values are obtained to be 3.1 K and 4.3 K for G and X_{5nm} respectively. The Weiss constant for the other samples are also determined in this manner and tabulated in table 3.3. It can be seen from the table that the θ values are less than < 5K indicating the fact that all the systems are weakly antiferromagnetic. Chadha et al. found that for higher volume fraction (>35%) sputtering of Co the value of θ can be as high as 50K and the interactions are ferromagnetic in nature [98]. In other words, the volume fraction of Co plays an important role in determining the effect of interactions. As the volume fraction increases, so does the grain size and the interactions change from being anti-ferromagnetic to ferromagnetic [99].

3.4 M-H loops

The vibrating sample magnetometer is used to obtain the M-H loop for non-saturating fields between $\pm$11 kOe. The granular films usually saturate at fields greater than

6T [9, 74].

Structure	Magnetic Moment at 11 kOe (μemu)
G	53
2G	97
$X_{1.5nm}$	93
X_{3nm}	93
X_{5nm}	135
X_{10nm}	135
X_{15nm}	111

Table 3.4: Magnetic moment for the various structures at 11 kOe

As suggested in the previous chapter, the M-H loop hsizes and hence observe possible CB.elps in obtaining the relative grain size for comparison. Samples with inserted oxide layer have the same Co content as sample 2G but show dissimilar M-H loops as seen in fig. 3.8a. The slope of M-H loop (or the susceptibility) gives an estimation of the grain size distribution - the smaller grains will pin slowly with applied magnetic field, while the bigger grains will pin faster giving steeper slope. So in this case X_{5nm} to X_{15nm} has a larger grain size distribution than G and 2G because of the same. This is verified in Chapter 4, wherein a model based on ref. [82] is used to generate the grain size distribution from the M-H loops. Table 3.5 shows the obtained grain size values for all the structure using this model and it can be seen that these obtained values are consistent in trend with the obtained SQUID results.

Interactions also play a role in this analysis - ferromagnetic interactions will give steeper slope whereas the presence of anti-ferromagnetic interactions will give a smaller gradient. However we have already shown that the system has minimal antiferromagnetic nature (section 3.3) and hence the M-H loop presented here are a good representative of the grain sizes.

Large grain sizes align easily to the applied field compared to smaller grain sizes and this is reflected in the M-H loops as steeper rise in moment with field [82].

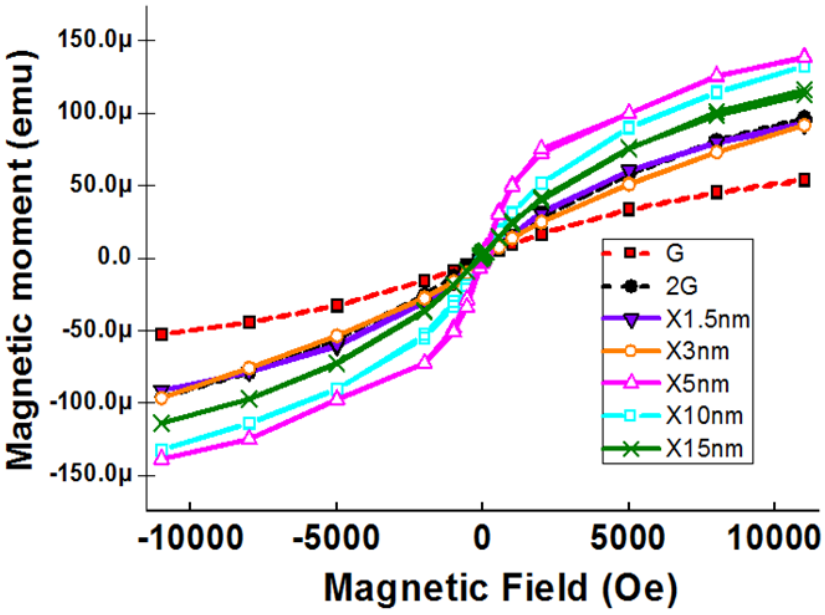

(a)

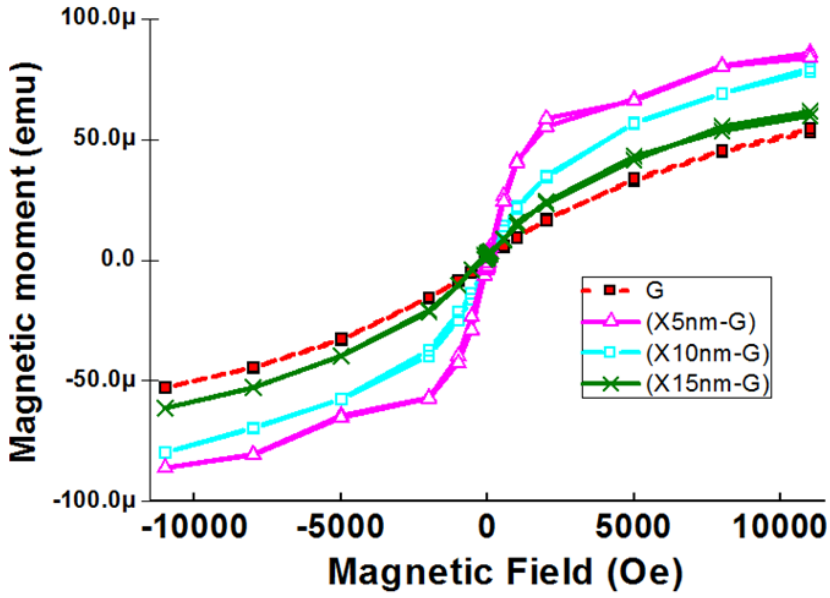

(b)

Figure 3.8: M-H loop for the samples a)G, 2G and proposed structures b)Magnetic moment for X_{5nm} *to* X_{15nm} (after subtraction with that of G)

It is known that the Co content is same for 2G and $X_{1.5nm}$ to X_{15nm}. Therefore, the magnetic moment at saturation field will be same for all these films. However, at non-saturating field of 11 kOe , it can be seen from the M-H loops that the magnetic moments are different for different films. This is due to the different grain size distribution in the films. Higher magnetic moment observed at 11 kOe indicates the presence of larger grains. The samples X_{5nm} to X_{15nm} have been shown to have continuous inserts as discussed in section3.2. Therefore, the bottom granular film in these structures are similar to structure G and hence to obtain the contribution from the top granular film, the magnetic moment of G is subtracted from these structures and the results are as shown in fig. 3.8b. It can be seen that the moment contribution from the top layer for X_{5nm},X_{5nm} and X_{15nm} is greater than that of G. This shows that top layer has a larger grain size than the bottom layer in these structures [6, 100].

Structure	**Grain diameter (nm)**	
	μ	σ
G	2.73	0.47
2G	2.51	0.475
$X_{1.5nm}$	2.49	0.57
X_{3nm}	2.405	0.43
X_{5nm}	3.07	0.41
X_{10nm}	3.05	0.32
X_{15nm}	2.914	0.34

Table 3.5: Grain size obtained by fitting the M-H loop

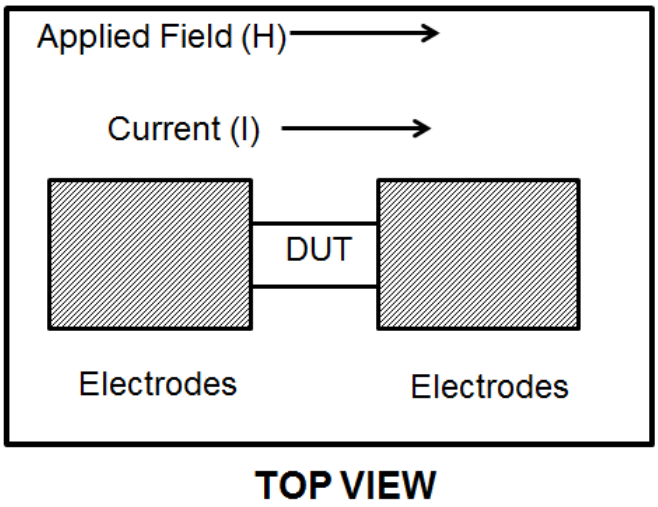

Figure 3.9: CIP measurement of the devices (Applied Field parallel to current - Top view)

3.5 Resistance and MR(at 4kOe) ratio trends

In order to understand the microstructure and electrical properties of the structure, the conductivity and MR trends were analyzed. The electrical properties are obtained by making I-V and MR measurement on the CIP devices in the temperature range of 11K and 300K as shown in fig. 3.9 where the applied field of 4KOe is parallel to the current. It was observed that the MR curves were same when the applied field is perpendiculFigure. 3.5aar to the direction of the current. Similar MR curves in both the measurement configurations points to an absence of any AMR in these structures [101].

Figure. 3.10 shows the resistance and MR curves for all the films. It is noted that in general there is a rise in MR ratio with decrease in temperature. This can be explained on thermal generation of electrons. These electrons are magnetic field independent and cause reduction in MR ratio [22,102]. As the temperature is lowered the generation of thermal electrons are reduced and hence the MR improves. However, the MR increase is not linear and there is some dependance. Various research articles have modeled the anomalous dependance of conductance with temperature

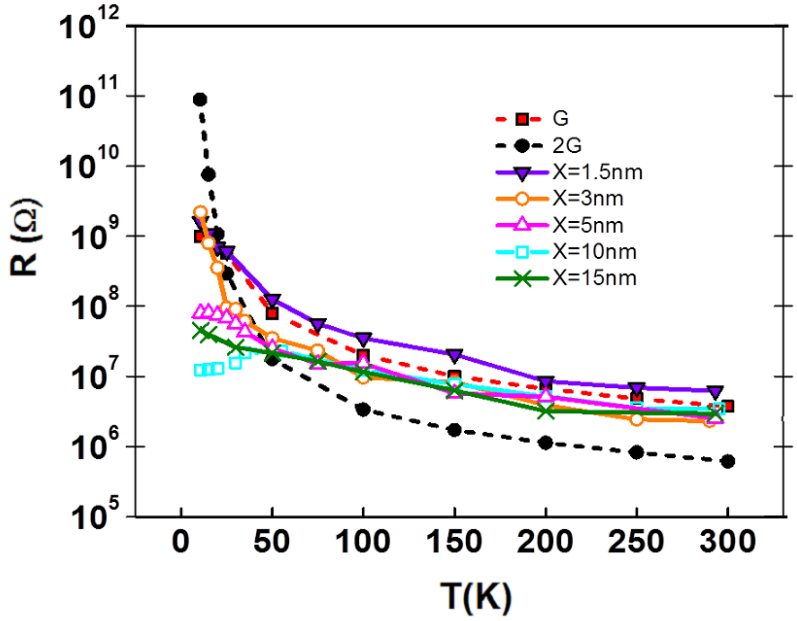

(a)

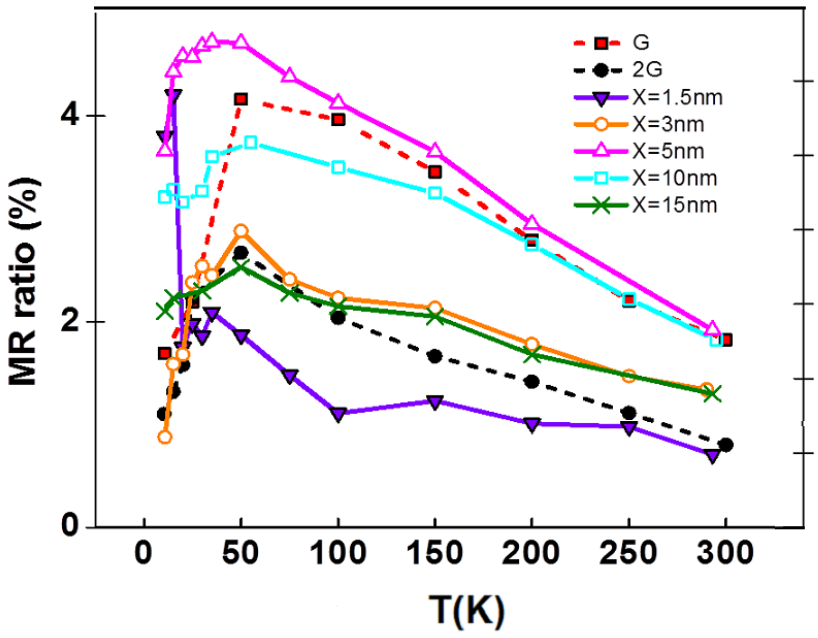

(b)

Figure 3.10: Temperature variation of a) R and b) MR_{4KOe} ratio for all the samples

based on either variable hopping in amorphous semiconductors or tunneling conductance in insulating granular film system or electron-electron interaction effects in a disordered metallic system [29, 103, 104]. Therefore, we will proceed to analyze the anomalous dependance of conductance based on these models.

3.5.1 Conductivity vs. Temperature dependency

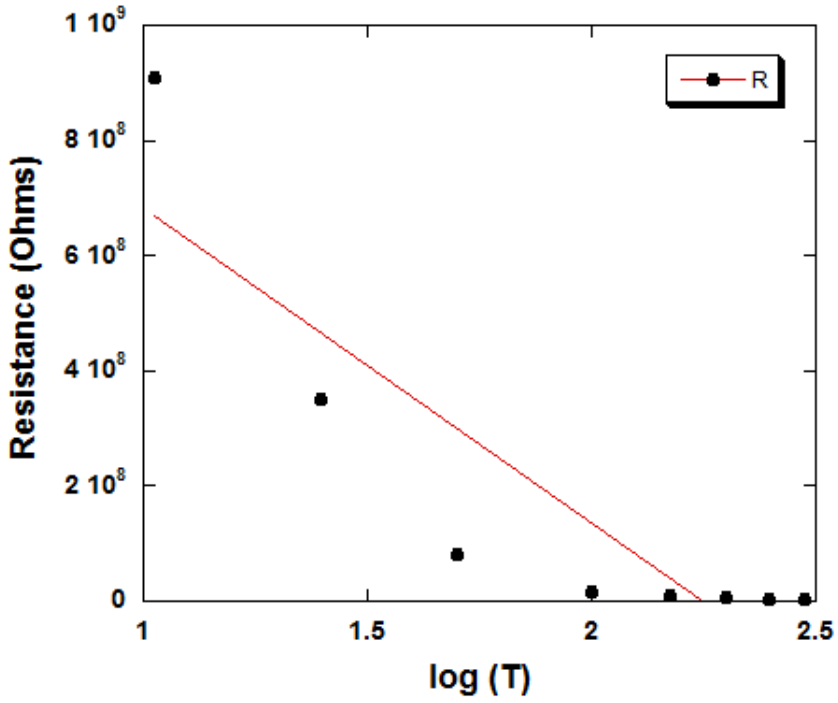

Figure 3.11: Resistance vs. Log (T) trend for sample G (based on eqn. 3.3- red line represents the linear fit)

Denardin et al. [103] have studied sequential sputtering of Co-SiO_2 granular multilayers earlier and found that their conductance variation with temperature was related to weak localization or electron–electron interaction effects in a disordered metallic system. The difference between their film and the one discussed in this thesis is that their films have thicker oxide layer which are continuous in nature as compared to films discussed in this thesis. The conductivity equation for such systems show the following dependency

$$\frac{1}{\sigma} \propto log(T) \tag{3.3}$$

The other possible dependance of conductivity is variable range hopping conductivity with electronic states being exponentially localized at random positions and the states being isotropic with random energies. This is the Mott's law [105] given by

$$1/\sigma \propto exp(T^{-1/4}) \tag{3.4}$$

Ziese et al. studied La-Ca-Mn-O Films [104] which were prepared by sequential sputtering in a manner similar to films discussed in this thesis. They found that the half metallic films did not follow the conductivity equation trend proposed by Sheng et al. [22] and found conductivity dependance as shown in eqn.3.5

$$1/\sigma \propto exp(T^{-3/2}) \tag{3.5}$$

Figure. 3.11 shows the resistance fit for sample G using eqn.3.3. If the proportionality was true then the fit should have been linear. However it can be seen that the fit is non-linear and is not a good representative for the films. Similarly fitting were done using eqns. 3.4 and 3.5 and it was found that the fit were not good and this was applicable for all the structures.

Finally, the fit was done using $T^{-1/2}$ for sample G and it can be seen from fig. 3.12 that fit is very linear and fits the best compared to other equation and hence is a good representative for the films. This dependence shows that the conduction in our granular film is due to thermally activated tunneling as explained by Sheng et al. using the charging energy modeling [22], which is actually valid for most insulating granular films [6,29,30,37]. However it can be seen from the fit that the graph shows

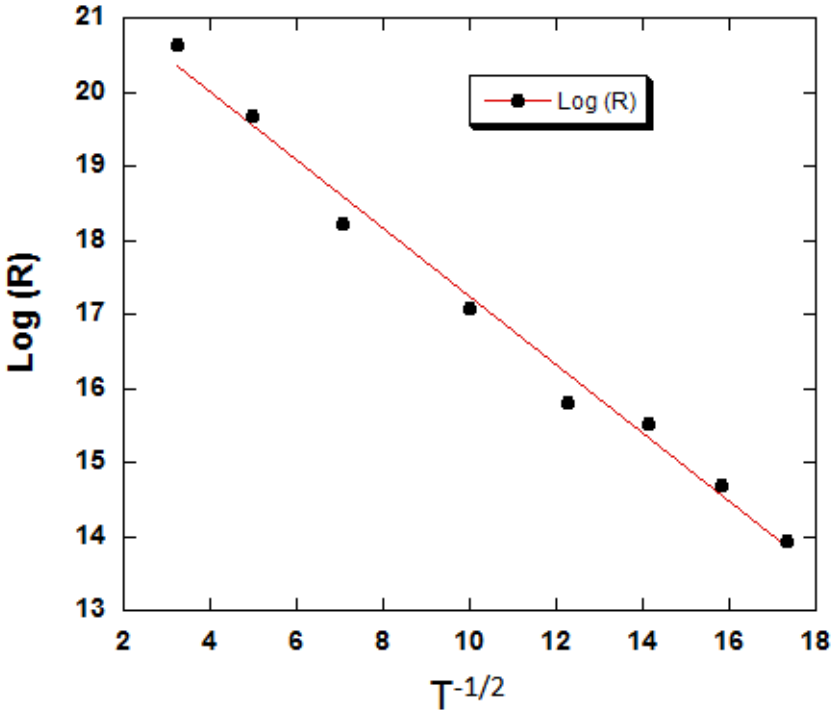

Figure 3.12: Log (Resistance) vs. $T^{-1/2}$ for sample G (red line represents the fit)

a additional shift and fits rather well to eqn.3.6 which has an additional term β which represents the leakage constant. [6,106]. Fitting the variation of conductance curve with temperature with eqn.3.6 gives the tunneling activation energy C_A for the various structures [22,107].

$$g = \alpha e^{-2\sqrt{C_A/k_B T}} + \beta \tag{3.6}$$

where α is the proportionality constant, β is the leakage constant, C_A is the activation energy k_B is the Boltzmann constant and T is temperature.

Fettar et al. have analyzed discontinuous double junctions consisting of the Co clusters sandwiched between Co/Cu electrodes as shown in fig. 3.13 [102]. They found that the temperature dependence of the resistance can be attributed to two conduction channels in parallel between electrodes i) via granules and ii) via other channels such as metallic/magnetic impurities in the insulating layer. They modeled

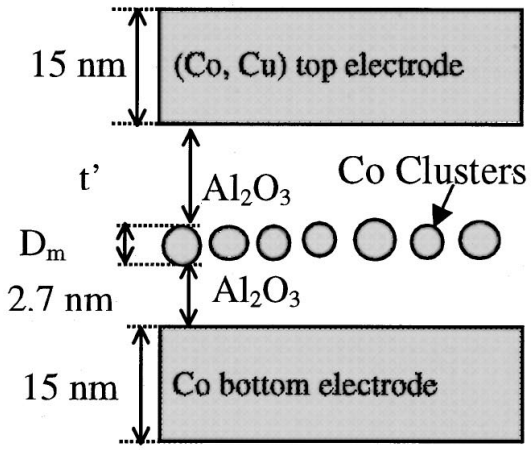

Figure. 3.5a

Figure 3.13: Drawing of cross section of the discontinuous double junction [102]

the resistance as

$$1/R = (1/R_1)exp\{-2.(c/T)^{0.5}\} + 1/R_2 \tag{3.7}$$

where 1/R is the observed conductivity, R_1 is related to proportionality constant, R_2 is related to leakage conductivity and C is related to activation energy (very similar to eqn. 3.6).

The first term in eqn.3.7 represents a thermally activated tunneling current flowing from grain to grain in the discontinuous layer while the second term ($1/R_2$) is the resistance due to possible metallic/magnetic impurities in the insulating layer. This variation was also observed by Honda et al. in Fe-SiO_2 granular films which they attributed to leakage conductivity in such systems [6]. The channels responsible for this leakage conductivity are field-induced tunneling in the high electric field regime [6] or magnetic impurities [108]. Fettar et al. found that the leakage in their structure was due to the existence of isolated Co atoms. This non-aggregated atoms or very small clusters of Co was also observed by Maurice et al. for their Cobalt-Alumina granular films [27].

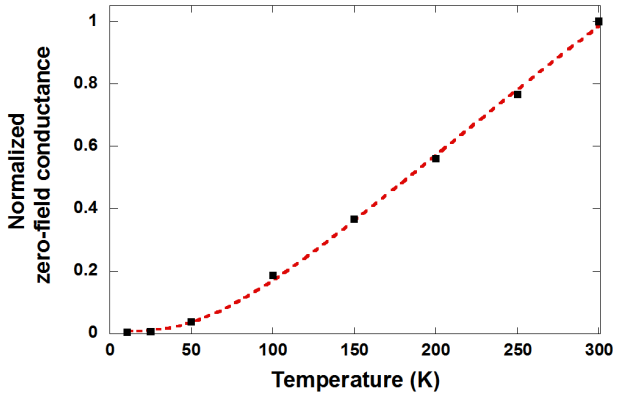

(a)

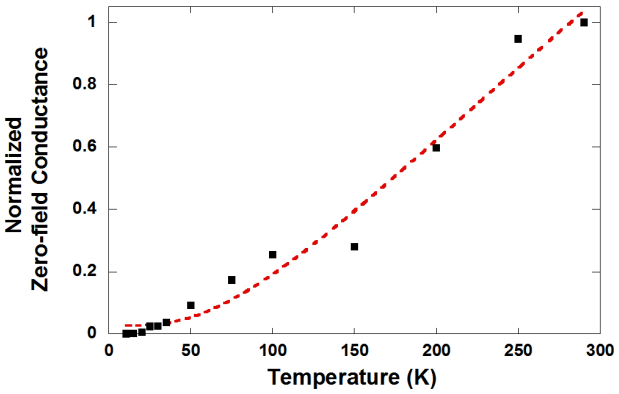

(b)

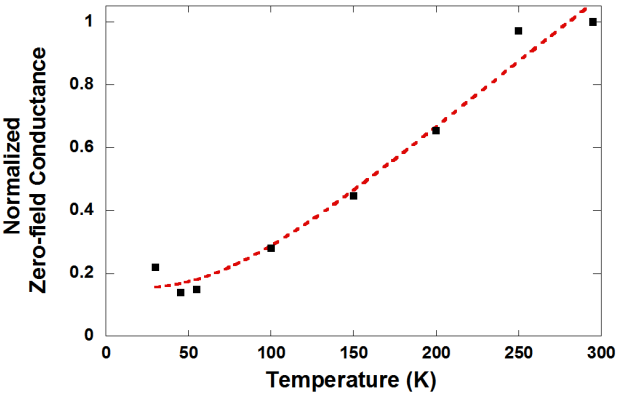

(c)

Figure 3.14: Curve fitting using eq. 3.6 - Normalized conductance vs. Temperature for samples a) Sample G ,b) Sample X_{3nm} and c) Sample X_{10nm} . The curve fitting is good with C_A value given in table 3.6 and β value in fig. 3.15

The variation in the conductance with temperature for the sample G, X_{3nm} and X_{10nm} is shown in Figure. 3.14. The conductance have been normalized with that at 300 K. The table 3.6 gives the tunnel activation energy for the various films calculated using similar fitting [22, 107].

Structure	C_A (meV)
G	38.8
2G	40.5
$X_{1.5nm}$	37.8
X_{3nm}	41.7
X_{5nm}	39.4
X_{10nm}	41.7
X_{15nm}	40.1

Table 3.6: Activation energy for the proposed structures (C_A)

As seen from table the values of C_A are very similar for films and the parameter C_A is defined by eq. 3.8

$$C_A = s \times \frac{e^2}{d} F\left[\frac{s}{d}\right] \tag{3.8}$$

where s is the grain size, d is the inter-granular distance and $F[\frac{s}{d}]$ is a function which is dependent on the shape and arrangement of the grains [6, 22].

Higher values of C_A indicate presence of FM grains that are well separated and having a sharp particle-matrix interface. Previous studies done by Strijkers et al. [109] on Fe-HfO and Fe-HfSiO granular films prepared by reactive sputtering show lower activation energy. The activation energy was calculated to be 2.6 meV for $Fe_{40}Hf_6Si_6O_{48}$ and 0.7 meV for $Fe_{47}Hf_{10}O$ films. These low values of C_A were attributed to the intermixing of Fe and Hf phases. However, the Co-HfO_2 films studied in this thesis have higher values of C_A as shown in table 3.6 indicating the fact that Co and HfO_2 phases are well separated for the films. Therefore the proportionality of conductivity to $T^{-0.5}$ dependence on temperature, along with

high tunnel activation energy and resistivity indicates the presence of discontinuous Co particles embedded in HfO_2 matrix.

Usually the C_A value decreases exponentially with increase in volume fraction [6]. In the case of granular films prepared by co-sputtering technique, the s/d is a function of ferromagnetic concentration [6, 22] and hence similar C_A values reflect that they have similar compositions according to Sheng et al's theory [107].

The β value is the leakage constant introduced by researchers [6, 106, 110] to explain the deviation from the $T^{-1/2}$ law which was originally proposed by Sheng and Ables [22]. This term usually represents the conduction through the film due to field-induced tunneling in the high electric field regime [6] or magnetic impurities [108]. For the films discussed in this chapter, the proposed films are sputtered in a similar manner and hence the expected leakage due to field induced tunneling for all the structures should be the same. However from the β value shown in fig. 3.15, it can be seen that the leakage constant increases with thickness of inserted HfO_2 layer. This can be interpreted as presence of magnetic impurity (isolated clusters of Co atoms) in the oxide layer separating the top and bottom layer of the proposed structure. The RBS data X_{15nm} shows presence of $\sim 7\%$ of Co in the inserted oxide layer which is due to the presence of Co clusters. It was also observed using RBS that $X_{5nm}$and X_{10nm} had $\sim 6\%$ of Co in the inserted oxide layer. This can be interpreted as presence of Co clusters at the interface separating the central oxide and granular film The amount of Co clusters in the inserted oxide layer increases with the thickness of the oxide layer and these are responsible for leakage conductivity. The conduction through the Co clusters is independent of the magnetic field and hence reduces the effective MR ratio. The possibility of presence of Hf metal in such thick HfO_2 layers is also considered. However, the stochiometry of the films in the central layer obtained through RBS suggests the Hafnium exists as oxide and not as metal. The

presence of Co in the inserted layer is a valid indicator of Co atomic clusters which causes leakage conductivity.

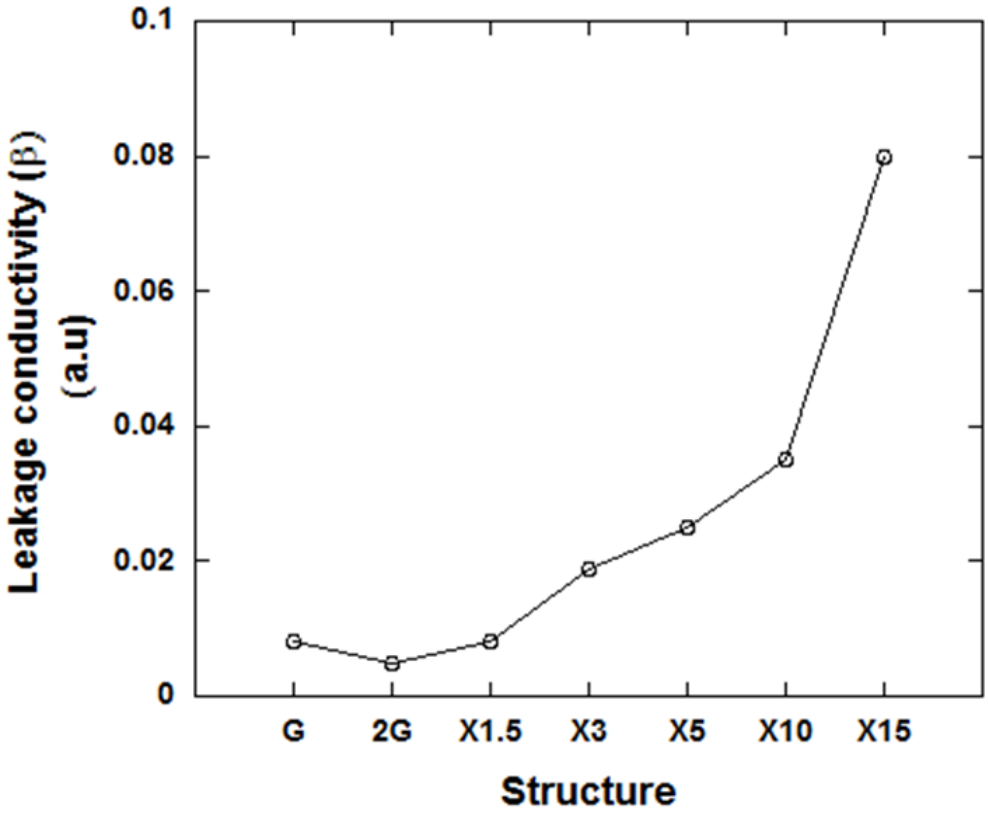

Figure 3.15: Leakage constant (β) for the different fabricated structures. It increases with increasing inserted oxide thickness indicating the presence of Co in the inserted layer as atomic clusters

In general, the resistances trends for the inserted oxide sample are closer to G than 2G. The MR ratio trends for all the samples show a increase in MR with decreasing temperature until 40K below which it starts to decrease. This is approximately the blocking temperature (T_B) for all the samples and the MR decreases because of this blocking effect [6].

It was already discussed in the section 3.2 that based on the the roughness of the inserted layer, the films can be split into insert with discontinuous and continuous

regime. Also, the structures G and 2G form the basis for this study. Hence for proper analysis the data set is divided into three groups .

1. Group A: Standard film devices (G and 2G)
2. Group B: Films which have discontinuous sandwich layer (X=1.5nm and 3 nm), Sample G and 2G
3. Group C: Films which have continuous sandwich layer (X= 5, 10 and 15 nm), Sample G and 2G

3.5.2 Group A : CIP measurement of sample G and 2G

The resistance and MR ratio trend for group A is shown in fig. 3.16. It can be seen that sample 2G, having twice the number of bilayers as G, has lower resistance compared to G. This is in accordance with the previous results on granular films as well as our experiments based on bilayer experiments [74]. One of the major reasons for this is the increase in the number of available tunneling paths with increasing thickness [83]. Below 20 K, it can be seen that the sample 2G shows an increase in resistance as compared to G. This can be explained based on the fact that sample 2G has lower grain size with higher spread (seen from table 3.2) and blocking of the smaller grains leads to an increase in resistance at temperatures below 20 K. Since the major conduction for sample 2G is due to smaller grains as compared to sample G, the MR is lower for sample 2G as compared to sample G. The MR ratio for both the films shows a decrease below 40 K which corresponds to the the approximate blocking temperature (T_B) and MR drops below that this temperature because of the blocking of the grains [6].

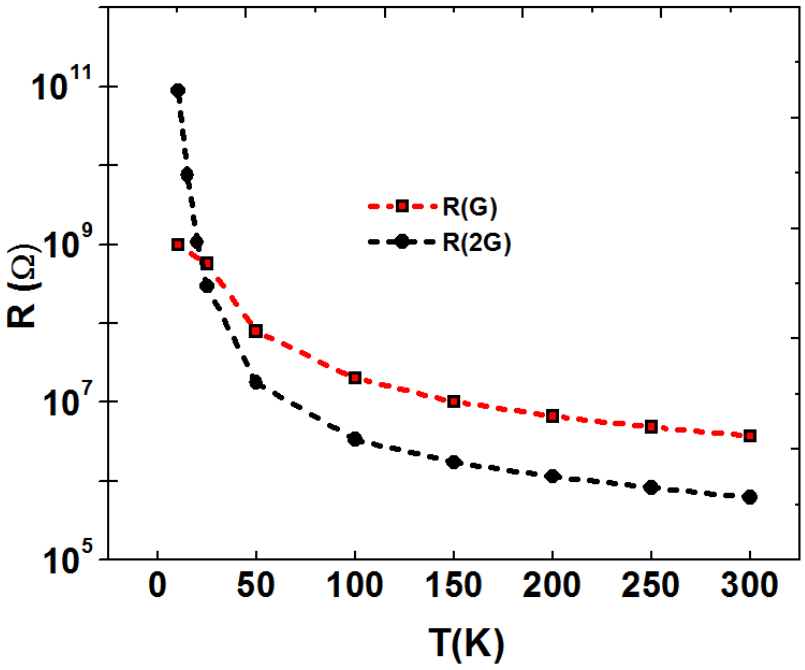

(a)

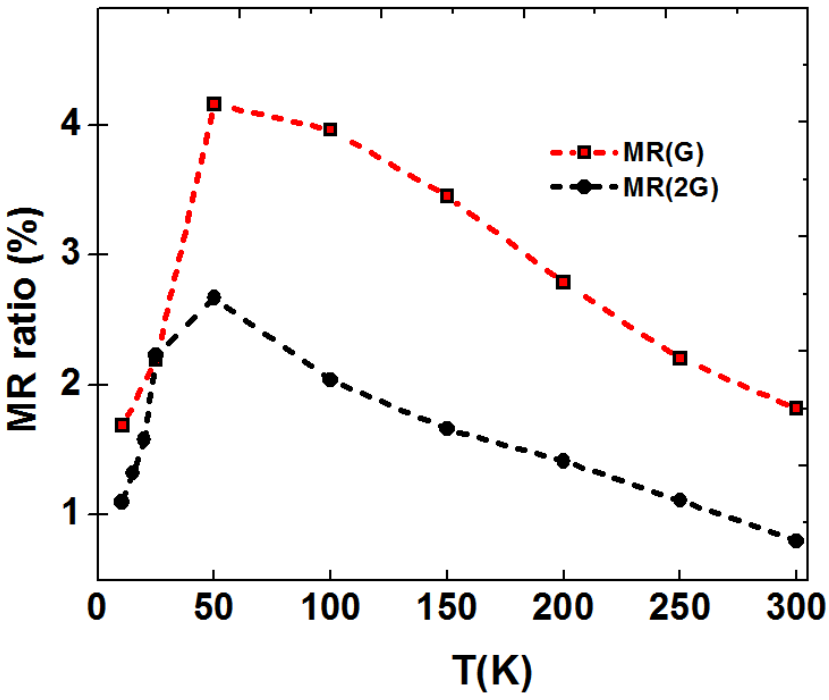

(b)

Figure 3.16: Group A: Samples G and 2G - Temperature variation of a) R and b) MR_{4KOe} ratio

3.5.3 Group B: CIP measurement of sample 2G, $X_{1.5nm}$ and X_{3nm}

In group B, it can be seen that $X_{1.5nm}$ has slightly higher resistance compared to G, although the order of resistance is still the same ($10^6\Omega$ at room temperature to $10^9\Omega$ at 10.6 K) as shown in the fig. 3.17. This is due to the discontinuous insert which introduces higher roughness and hence larger grain size spread as seen from table 3.2. Compared to this, X_{3nm} has smaller resistance than $X_{1.5nm}$ as well as G because the inserted layer has reduced discontinuity leading to lower roughness and hence reduction in grain size spread. As seen from the M-H loops (fig. 3.8a) 2G, $X_{1.5nm}$ overlaps while X_{3nm} has a slightly lower magnetic moment compared to the other two. This refers to the fact that grain size of X_{3nm} is smaller than the other two which is also confirmed by the FC/ZFC measurement (table 3.2). The structures have different resistances and MR ratios because of the discontinuity and roughness of the inserted layer which in turn affects the grain size distribution leading to a change in conduction and MR ratio.

$X_{1.5nm}$ shows interesting transport characteristics. If the MR ratio of $X_{1.5nm}$ is considered, it can be seen that the MR ratio increases from 0.72 % at room temperature to 2.10 % at 50 K. It then drops to 1.71 % at 20 K which is expected due to blocking of the grains below 50 K [6]. However at 15 K, it rises to 4 % and at 10.6 K, it stays around 3.8 % as seen from the fig. 3.17. This sudden increase in MR is due to higher order tunneling [30], wherein there is tunneling between between larger grains occurs through intermediate smaller grains. Mitani et al. found that for their Co_{54} $Al_{21}O_{25}$ films the variation of MR ratio changed from ~6 % to 8 % from room temperature to 40 K and then below 40 K the MR ratio suddenly increased to ~15 % at temperature of ~5 K because of higher order tunneling [30]. This is an inherent property of granular films as it has a broad distribution of grain

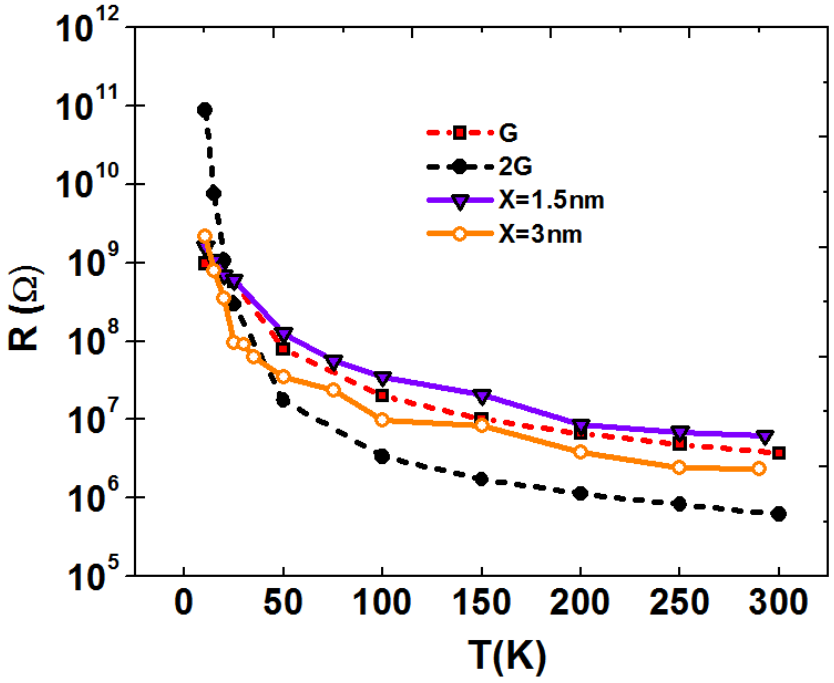

(a)

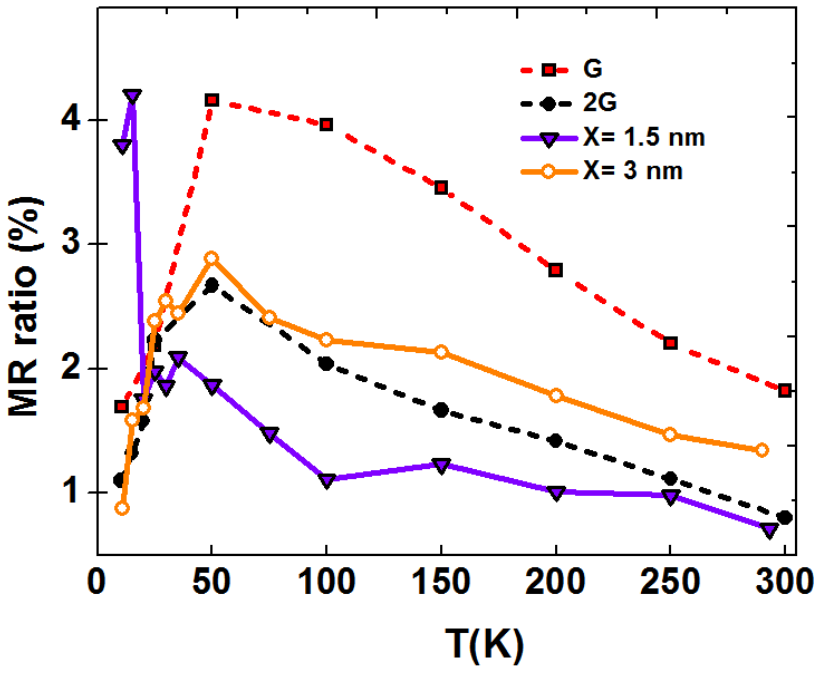

(b)

Figure 3.17: Group B: Samples G, 2G, $X_{1.5nm}$ and X_{3nm} - Temperature variation of a) R and b) MR_{4KOe} ratio

sizes [30].

Figure. 3.18 shows the MR ratio curve for $X_{1.5nm}$ for temperatures 10.6 K, 25 K, 35 K and 50 K. It can be seen that the switching field of the samples increases with decreasing temperature and there is also increase in MR ratio due to higher order tunneling.

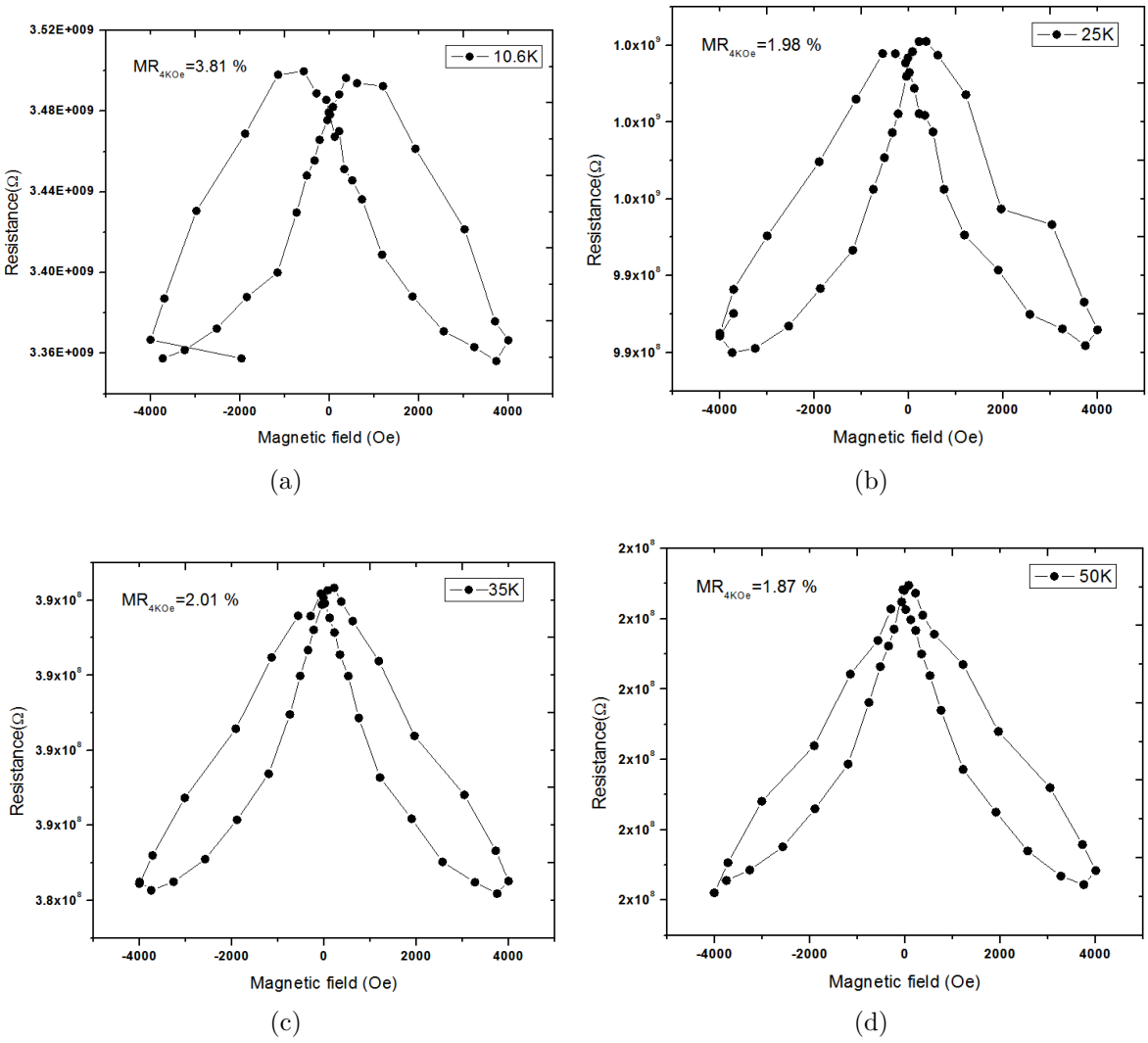

Figure 3.18: MR curve for $X_{1.5nm}$ at various temperatures for fields between ±4 KOe a) 10.6 K b) 25 K c) 35 K and d) 50 K

For temperatures above 15 K, $X_{1.5nm}$ has lower MR than X_{3nm} and 2G. It should be noted that $X_{1.5nm}$ has discontinuous oxide insert and because of this the effective

grain size distribution has a higher spread. As a result, compared to the other structures, $X_{1.5nm}$ has different grain sizes along the conduction path and from the higher resistance observed compared to other structures, it can be concluded that smaller grain sizes are involved in the conduction. As a result the effective change in resistance (ΔR) for $X_{1.5nm}$ at T>15 K is smaller in comparison to X_{3nm} and 2G leading to lower MR ratio as compared to them.

Compared to $X_{1.5nm}$, structure X_{3nm} has a much more continuous insert leading to lower roughness as seen from fig. 3.5a. The 3 nm insert is not as continuous films as the 5 nm and is not expected to form proper parallel paths by splitting the granular film at the center. Therefore, the expected resistance of X_{3nm} lies between that of G and 2G. It can be seen from the fig. 3.17 that the resistance variation with temperature is closer to G than 2G indicating the fact that continuity of the insert is better than $X_{1.5nm}$, but still not continuous enough. This will affect the MR ratio of X_{3nm} and it should be higher than $X_{1.5nm}$ but still lower than that of G. This is verified in fig. 3.17 and it can be seen that its MR is actually better than 2G and $X_{1.5nm}$, but still lower than G. Therefore it can be postulated that X_{3nm} has lower discontinuity of the insert than $X_{1.5nm}$ nm but not continuous enough to reflect sample G like characteristics. Hence the resistance variation is closer to G, while the MR variation is closer to that of 2G.

3.5.4 Coulomb Blockade in $X_{1.5nm}$, 2G and X_{3nm}

This section deals with CB nature of structures $X_{1.5nm}$, 2G and X_{3nm}. The CB for 2G and X_{3nm} is at a temperatures lower than 10.6 K unlike sample $X_{1.5nm}$ which shows CB at 10.6 K. Figure. 3.19 shows the CB curves for samples 2G and X_{3nm}. The plot is generated by measuring current while sweeping the applied voltage between -10 V and 10 V. The various temperature of measurement are 10.6 K, 15

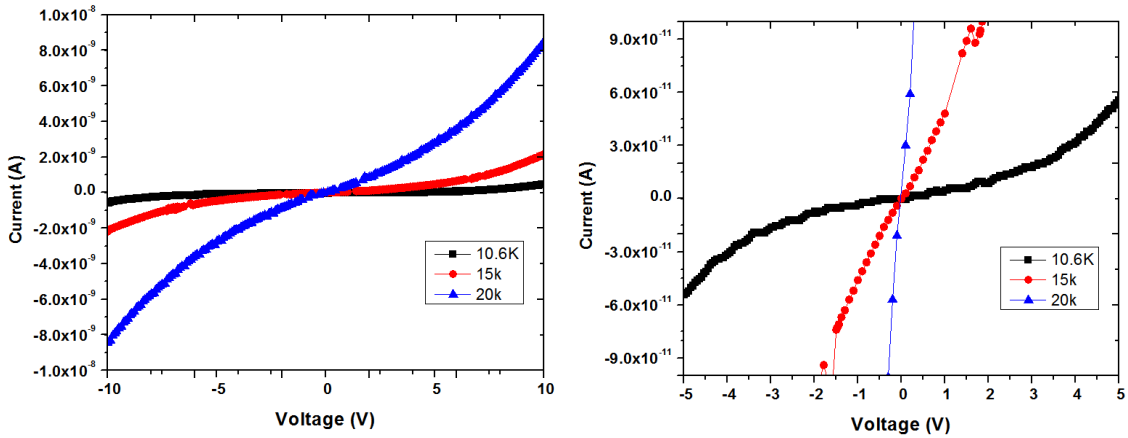

(a)

(b)

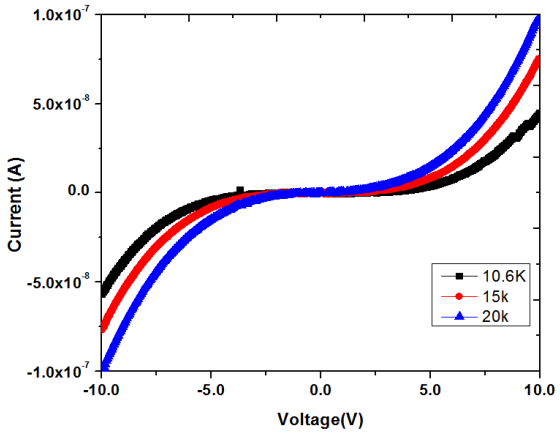

(c)

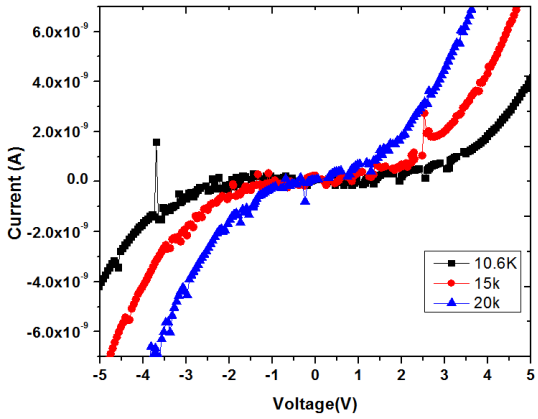

(d)

Figure 3.19: IV curve for a) 2G at T=10.6 K,15 K and 20 K for V=±10V b) Zoom in for 2G at T=10.6 K,15 K and 20 K for V=±5V c) X_{3nm} at T=10.6 K,15 K and 20 K for V=±10V b) Zoom in for X_{3nm} at T=10.6 K,15 K and 20 K for V=±5V

K and 20 K respectively. Compared to 2G, X_{3nm} shows more obvious trend toward CB as seen from the fig. 3.19 as seen from the decreasing slopes of the V-I curves with temperature.

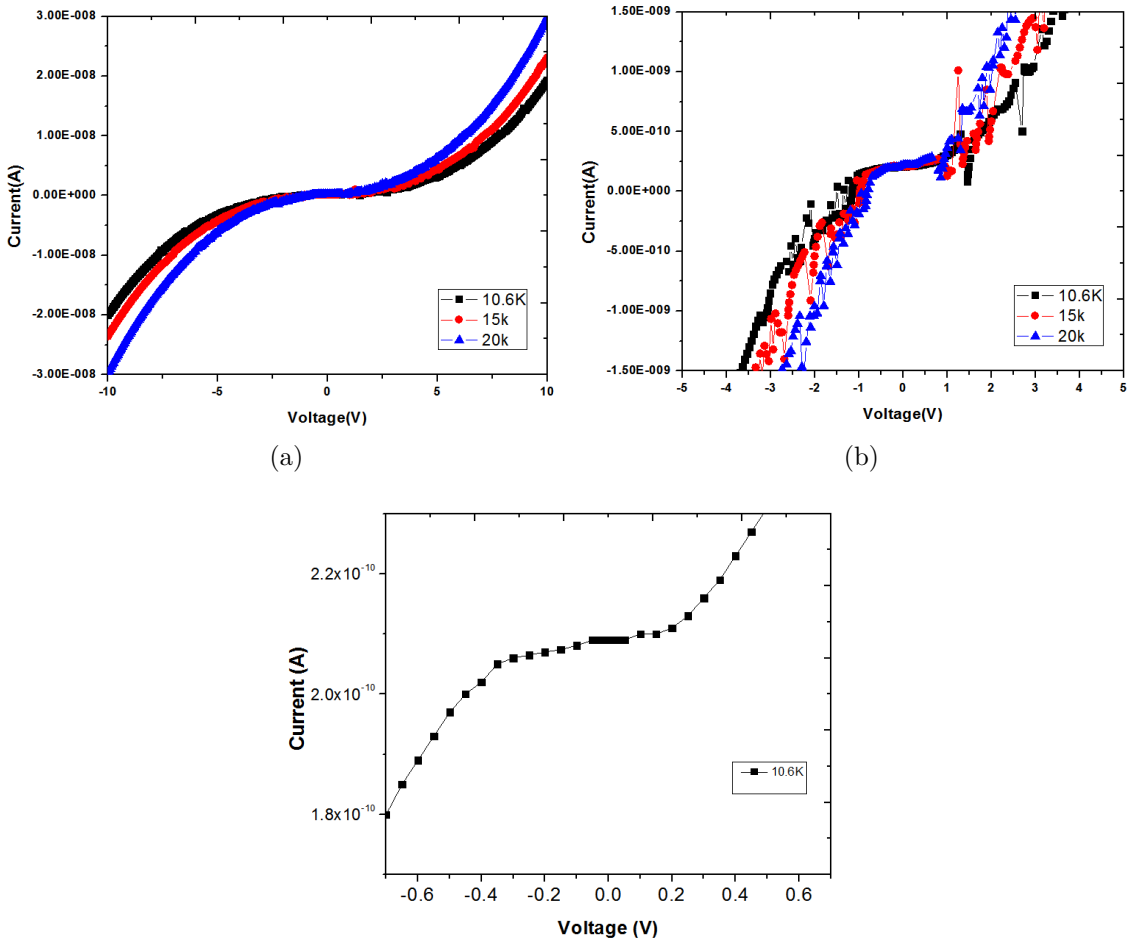

Figure 3.20: IV curve for $X_{1.5nm}$: a) T=10.6 K,15 K and 20 K for V=±10V b) T=10.6 K,15 K and 20 K for V=±5V c) T=10.6 K showing CB

$X_{1.5nm}$ is the only structure which shows CB at 10.6 K as seen from fig. 3.20. The CB threshold voltage (V_{th}) for $X_{1.5nm}$ is observed to be 50 mV at a temperature of 10.6K [20,30]. Using the eq. 3.9, the approximate grain size of the blocking grains can be calculated [20].

$$V \leq \frac{e}{2C} \tag{3.9}$$

where C =$2\pi\epsilon d$ where ϵ is the permittivity of the surrounding medium (HfO_2) and d is the Co grain size.

Substituting the values, the value of grain size obtained was 2 nm indicating the fact that in sample $X_{1.5nm}$, there exists grains of sizes less than ~2 nm along the conduction path which is not only responsible for CB but also for the high resistance. The MR ratio in the CB regime is enhanced by $2/(1-P^2)$ as compared to the sequential tunneling regime (P is the spin polarization of a ferromagnetic electrode) [69]. In the case of $X_{1.5nm}$, the MR ratio at 20 K is ~1.7 % and for temperatures below 20 K the MR increases to ~4 % which actually follows $MR_{20K} \times 2/(1-P^2) = 1.7 \times 2/(1-0.34^2) = \sim 4\%$ where P=0.34 for Co and matches the suggested higher order tunneling increase in MR discussed in section 3.5.3.

3.5.5 Group C: CIP measurement of samples 2G and X_{5nm}, X_{10nm} and X_{15nm}

The group C represents the films having a continuous inserted oxide layer. The variation of resistance and MR ratio for group C is shown in fig. 3.21. The resistance trend for all the samples X_{5nm} to X_{15nm},G and 2G are increasing with decrease in temperature. The change in order of resistance (10^6 Ω at room temperature to 10^7 Ω at 10.6 K) with temperature for samples X_{5nm} to X_{15nm} are very similar and close to the standard sample G. It is also observed that X_{3nm} from group B, has resistance values close to to these structures for temperatures below 50K (10^6 Ω to 10^7 Ω) and below that there is a increase in resistance to order of 10^9 Ω. This again indicates the fact that X_{3nm} is more continuous than $X_{1.5nm}$, but the grain size variation and spread in this structure leads to reduction in MR because of the

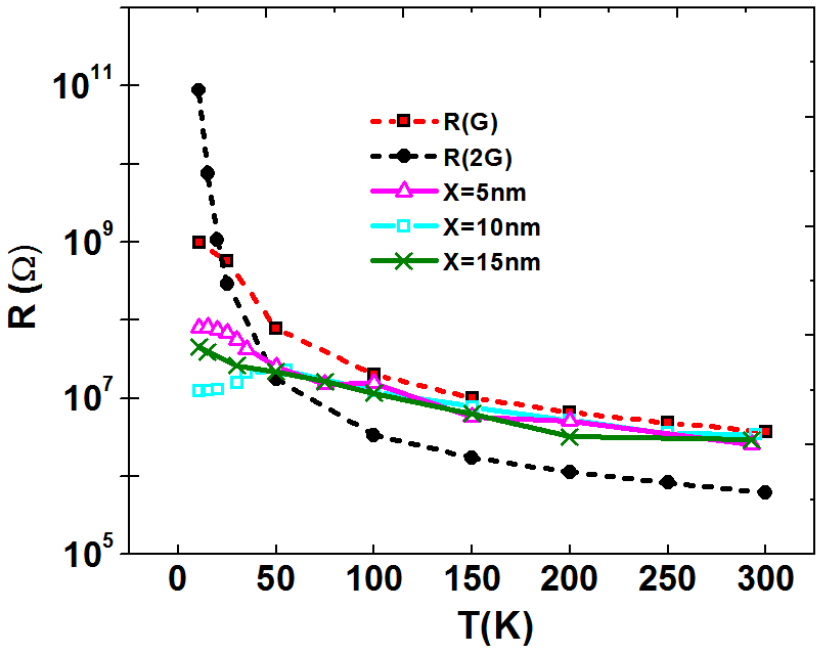

(a)

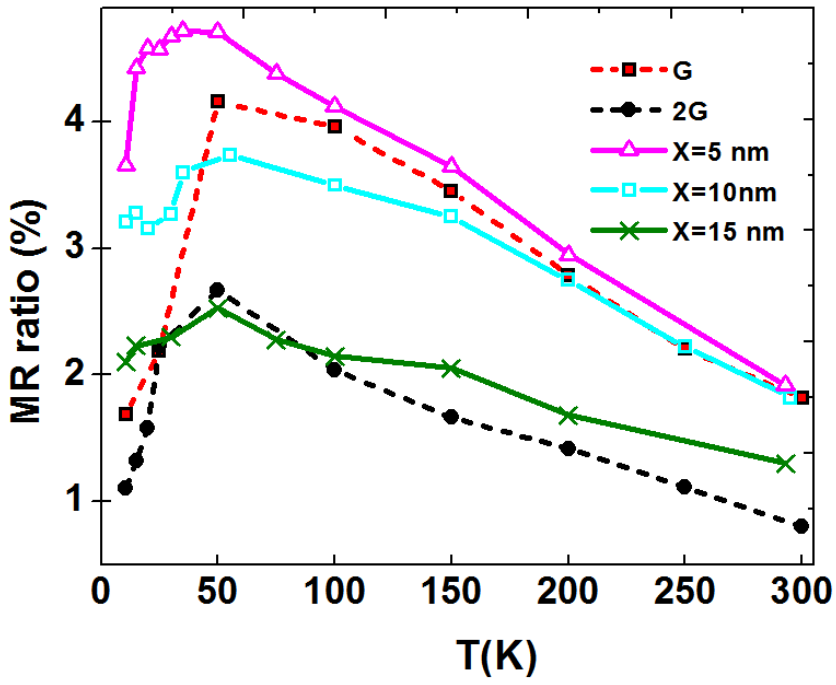

(b)

Figure 3.21: Group C: Samples G, 2G, X_{5nm}, X_{10nm} and X_{15nm} - Temperature variation of a) R and b) MR_{4KOe} ratio

smaller grains involved in the conduction (as seen from resistance trend and CB characteristics) as compared to structures X_{5nm} to X_{15nm}.

As the inserted layer of oxide becomes continuous, there are two layers of films formed which are parallel from conduction point of view. This provides two possible mechanisms for electrical conduction in these films:

- Parallel path conduction through both the granular film layers or
- Domination of conduction along the one of the paths (either top or bottom).

It can be seen that the bottom layer is sputtered in the same way as G and hence it is supposed to have the same grain size distribution as G. It is known from the M-H loops (fig. 3.8b) that the top granular layer had larger grain size compared to the bottom granular film layer and as a result has lower resistance of the two. It is well known that conduction is generally along the least resistance path. If the conduction is through bottom layer, it is expected that the resistance will be equal to that of G.

The resistance of G varies from 3.8×10^6 Ω to 9.8×10^8 Ω for a temperature change from room temperature to 10.6 K. The resistance change with temperature observed for the structure X_{5nm}(highest resistance change of the three structures) is from 2.8×10^6 Ω to 5×10^7 Ω from room temperature to 10.6 K. This variation is not only lower but also less than half the observed resistance of G (assuming conduction is along both the paths, the resistance will be nearly half). This indicates the fact that the conduction in X_{5nm} to X_{15nm} is majorly due to the top layer and not so much through the bottom layer. The change in resistance below the blocking temperature is lower for samples X_{5nm} to X_{15nm} as compared to sample 2G which has the same Co content. This can be explained based on the fact the conduction is majorly through the top layer in X_{5nm} to X_{15nm}, which has comparatively larger grains taking part

in conduction. Hence the conduction in these structures is less affected by blocking (T_B), compared to 2G which has smaller grains along its conduction path.

The observed MR ratio trend for this group seems to follow the magnetic moment obtained at 11 kOe i.e X_{5nm} followed by X_{10nm}, X_{15nm} and 2G gives the best MR ratio for field between ±4 KOe. However, it should be noted that the variation of magnetic moments with field are greater for X_{5nm}, X_{10nm} and X_{15nm} as compared to sample G (fig. 3.8b). But the MR ratios for X_{10nm} and X_{15nm} are much smaller than that of structure G which has comparatively smaller grains. This can be explained based on the leakage conduction β shown in fig. 3.15. This leakage conduction is due to Co atom clusters discussed earlier in section 3.5 and the conduction through these small clusters are independent of magnetic field. Hence the value of β correlates to the reduction in MR ratio. The MR reduction for X_{10nm} is not as pronounced as for X_{15nm} because its leakage conduction β is lower of the two.

Therefore for temperatures above 15K, X_{5nm} from group C shows improved MR ratio due to tunneling through larger grain size (1.93 % at room temperature to 3.67 at 10.6K), while for temperatures below 15K, the $X_{1.5nm}$ from group B gives improved MR ratio due to higher order tunneling (3.8 % at 10.6 K, while only 0.72 % at room temperature). The introduction of roughness is highest for $X_{1.5nm}$ and decreases monotonically for higher thickness of the insert. The structures X_{10nm} and X_{15nm} would have given improved MR ratios as compared to G because of their larger grain size, but the presence of high leakage conductance lowers the effective MR for such films.

3.6 Summary

In this chapter, a new structure is proposed and microdevices are fabricated by inserting a oxide layer (HfO_2) in between structure 2G. The top and bottom films

formed were of equal thickness to sample G, the optimum MR structure for Co-HfO_2 systems. The thickness of the inserted oxide was varied from 1.5 nm to 15 nm. The idea was to utilize the roughness of the inserted oxide layer to control the grain size and hence the electrical properties of films. By varying the thickness of the HfO_2 insert we were able to study regimes of continuous and discontinuous oxide film at the center of the granular film and its effect on conduction and MR. The films with discontinuous oxide showed CB characteristics whereas the films with continuous oxide showed that the major conduction path was along the top granular film. $X_{1.5nm}$ structure formed using a discontinuous insert thickness of 1.5 nm was the only sample with visible CB and higher order tunneling characteristic at 10.2K. The higher order tunneling improved the MR from 1.7 % at 20 K to 3.84 % at 10.2 K for $X_{1.5nm}$. Sample 2G was observed to have lower MR and resistance than the continuous insert structure namely X_{5nm} - X_{15nm}, suggesting that inserting an oxide layer improves both the resistance and MR ratio by changing the grain size distribution because of the roughness of the insert. The observed drop in MR with increasing HfO_2 thickness can be explained based on higher leakage conductivity. Thus by controlling the roughness of the insert layer we have succeeded in engineering different types of transport and hence moderating the MR ratio.

Chapter 4

Simulation model for CIP device conduction

The structures that have been fabricated in this research work and discussed in the chapters 3 are new and do not have reference structures to compare the results. As described in the motivation of this thesis, a model to obtain the M-H loop and MR curves for the proposed structures is described in this chapter. Some of the most important parameters useful for analyzing granular films are M-H loop and the magnetoresistance (MR) curves. The M-H loop for granular films usually follows the Langevin function and researchers have modified the same to obtain the fit for the experimental curves as discussed in Chapter 1. However, the simulation model does not generate the physical size and location based on the M-H loop. In this chapter, the grain size and location are generated using a model described in ref [82] and MR curves are obtained by implementing resistor network model for these grains.

4.1 Overview of the simulator

The simulator can be expressed as the block diagram in fig 4.1. It consists of 3 coding blocks

- Microstructure code (generation of randomly positioned FM grains)
- Loop code (M-H loop generation)
- Resistor network solver (MR curve generator)

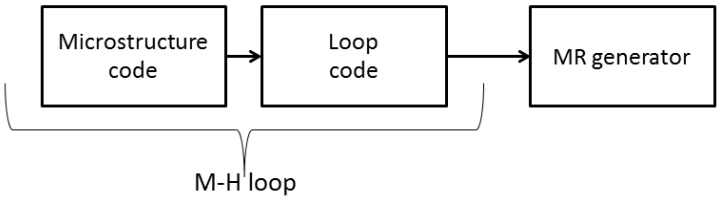

Figure 4.1: Block diagram of the simulation model - Consists of two steps; first one for generating the M-H loop and second for MR

The microstructure code and the loop code are based on the model in ref [82][1]. Those two block help obtain the M-H loop for the samples. The microstructure code takes user input of grain size and distribution information and generates granular film accordingly while the loop code takes the sample geometry information and the input of external field and generates the M-H loop for the sample. The resistor network solver calculates the effective resistance of the sample at various fields.

The microstructure model generates a cubic cell of particles with random locations and sizes. The coding is done in such a way so as to avoid overlapping of grains. If the generated particle overlaps with another one, it is regenerated in another random location and is repeated till none of the grains overlap. The grain sizes follow

[1]The basic codes were obtained from Prof Chantrell Roy from University of York

log-normal distribution which have been experimentally proved to exist in granular films [73, 77]. However, the simulator allows the making of another commonly used grain distribution system namely the Gaussian distribution. Preliminary fitting analysis done by our group showed that grain size distribution is log-normal and not Gaussian [111]. A selection criterion was implemented in the log-normal distribution wherein the grain size had to meet the condition $d_{Grain} \leq (5 \times d_{Median})$ to match the experimental grain size. The grain size generation and positioning is as follows.

1. The simulation model assigns the particles in decreasing order of their diameters in order to achieve better packing density by allowing smaller particles to occupy the interstitial space between large grains.

2. The anisotropy easy axes were generated randomly in 3D i.e., with a probability for the polar angle $p(\theta) = sin(\theta)$ and uniformly random distribution for the equatorial axis ϕ.

3. Periodic boundary conditions are applied along the three dimensions in order to remove the boundary effects for the magnetization of the grains at the edges.

The total energy of the particle is calculated as

$$E = KV(e.m)^2 - \mu \times H_T \tag{4.1}$$

where K is the anisotropy of the particle, V is the volume of the particle, H_T is the total acting field, $\overrightarrow{e}$ and $\overrightarrow{m}$ represent the unit vectors of the anisotropy easy axes and magnetization respectively. The total local field H_T acting on each particle is the sum of the applied field and the dipolar field arising from the neighboring particles, given by

$$H_T = H_a \hat{z} + \sum_{i \neq j} \left[\frac{3(\mu_j . r_{ij}) r_{ij}}{d_{ij}^5} - \frac{\mu_j}{d_{ij}^3} \right] \tag{4.2}$$

where the applied field is chosen to be along the z axis. The second term of the equation 4.2 represents the vector sum of the total dipolar fields arising from neighboring particles. $r_{ij} = d_{ij}.\hat{r}_{ij}$ is the position vector of the particles i relative to j where $\hat{r}_{ij}$ is a unit vector in the direction of the particle separation d_{ij}. The dipolar field is calculated within a spherical volume defined by a cutoff radius chosen to be at a distance six times the mean radius of the particles. The dipolar interactions depends on the grain size and reduces with distance. It becomes negligible for distances greater than six times the mean radius of the particles [82, 111] .

The most essential input parameters for the model are

1. Number of grains
2. Grain median diameter
3. Spread of grain size distribution (log-normal distribution)
4. Packing fraction

The number of grains affects the smoothness of the curves while the grain size and spread is taken from the experimental fit. The simulation model generates magnetic orientation for each particle at each applied field and sums it to obtain the magnetic moment. The number of grains along each axis is the same (say 'N' grains) and hence the simulator is a cubic system with N^3 grains. The computational time rises exponentially along with increasing N. The change in number of grains does not change the trends of M-H loops significantly at high field, but helps to reduce the noise at low fields. In order to reflect the exact thickness of the proposed structure, higher N values could not be used. Rather another technique was used

to reduce the noise, namely a factor of 'seed' is implemented in the simulator. The 'seed' is meant for generating random numbers which in turn control the diameters generated. So, for the same input condition, by changing the 'seed' value , the grain size distribution and location are changed. Thus, multiple M-H loops can be obtained for the same input condition, which can be averaged to obtained a reduced noise M-H loop. We have implemented a 20 averages for the M-H loop and obtained the MR curves in a similar manner. The grain median diameter and the spread are calculated empirically to find the most optimum value for the fit, while the packing fraction is taken from the RBS data from the experiments.

In this simulation, the focus is on the MR properties of the proposed structure i.e. granular film which has inserted oxide insulating layer. Since it has been already shown in Chapter 3 that that the conduction in the structures with oxide thickness greater than 5 nm is through the top layer, the MR curves are generated with the M-H loop of the top granular film and not of the whole structure. However for comparison of grain sizes obtained using FC/ZFC measurement in Chapter 3, the M-H loop of the whole structure has to be considered. In this model, the proposed structure is generated by by shifting up the top half of the film by user-defined value, which is the thickness of the insertion layer. As shown in fig.4.2, from the original granular bulk, the new routine finds the center of the film on the vertical axis and shifts all grain centers which lie in the top half by a user-defined value (thickness of the insert). The dimension of the final structure is no longer a cube. However, the properties of two granular layers such as grain size distribution and packing fraction are still identical.

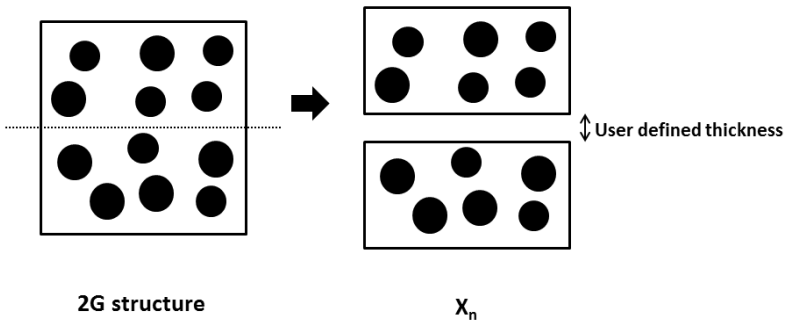

Figure 4.2: Schematic showing the generation of the proposed structures (all the proposed structures are generated from 2G by splitting the film at the center and separating the two blocks by required value)

4.2 MR generation

MR forms one of the most important parameters required for the analysis of granular thin films. Theoretical calculation/simulation of the MR curve can be achieved by the following method:

1. **Inoue model** - This was one of the most utilized model for obtaining the MR ratio for granular films, suggested by Inoue and Maekawa in 1996 [25]. According to this model (eqn.1.6), the thickness of the granular film does not affect the MR ratio, which was found otherwise by many experimental researchers [75, 80]. This is because the Inoue model averages out the grain size and grain separation and is based on the modification of the MTJ equation. Nevertheless the model is quite useful and serves as a starting point for modeling of the granular film conduction.

2. **Julliere's model** - This model was proposed by Julliere in the year 1975 for TMR calculation based on spin scattering [17]. If two adjacent grains in granular film can be considered as an electrode then the electron tunneling between the two can be solved using the Julliere's model. But it has to incorporate the fact that source of electrons for one set of granules(electrodes)

depends on the tunneling of the electrons from the previous set of granules. The model gets complicated, considering the fact that a single granule can receive electrons from all the surrounding granules in 3D matrix with varying probabilities. The other important factor is incorporation of tunneling as well as higher order tunneling which will make the model very complex.

3. **Resistive network** - This is one of the most widely used model for granular film as well as other films. The granules are considered to be nodes and the insulating barriers between them are thought of as resistors, which vary with magnetic field. So basically the granular material can be visualized as huge resistance matrix, which when solved gives the MR response. There are various methods used to solve the resistor network e.g

    - Partial Differential Equation [48]
    - Network solution methods like nodal elimination, solving simultaneous current voltage equations etc [112, 113]

The current work makes use of the resistive network model along with Inoue's equation [25] for establishing the initial results.The resistive model is quite flexible and simple to implement at the same time quite robust and reliable as proved by other researchers [113].

The grains are considered as nodes and the insulating barriers (along with the grain properties) are translated to resistor component between the nodes, which vary with magnetic field. Therefore, the granular material can be visualized as a huge resistance matrix, which when solved gives the MR response for a particular field. The resistor network model has been previously implemented for granular films.

One of the earliest know application of the resistive network model for granular films was in 1992 by Zhou et al [113]. They simulated electrical conduction in granular metals by mapping hopping conductance between grains into a simple cubic lattice resistor network. They assumed that the tunneling conduction occurs only among neighboring grains. Their sample matrix was $7 \times 7 \times 7$ with 1176 linear equations for current and voltages and $8 \times 8 \times 8$ with 4208 unknowns. Using their model they proved that granular film conductivity follows the $-log(\sigma) \propto T^{-1/2}$ rule [113]. In the year 2000, Lin and Wu modified previous transport theories which considered only the nearest-neighbor hopping in granular metals and compared the modified theory with the experiment of Abeles et al [114]. They carried out a critical path analysis, and showed that with practical material parameters, the modified theory gave values in better agreement with the experiment for the temperature-dependent conductivity :- $\rho \propto exp(-(T_0(x)/T)^{-n}$ where x is the volume fraction and n=0.5. They made use of the resistor network simulation to show that the value n=0.5 is applicable over a large range of temperatures. The network was solved with the help linear I-V equations to obtain the conductance [114]. In one of the recent papers, Zhou et al. have made use of the resistive model for simulating the magneto-resistance in half metals [115]. Their model relies on the usage of the Inoue model for the conduction between grains. They made use of 2D and 3D models for their research study and tested their model for 15×15 2D square array and $10 \times 10 \times 10$ 3D cubic array. They found that the MR for the 2D and 3D model varies as the polarization factor increases. Their calculation only takes the magnetic field at zero and maximum field (when the spins are non-aligned and perfectly aligned respectively). For the randomized spins at zero field they make use of the spherical co-ordinates and allow the computer to generate the required two angles for each of the grains.

The implementation in this thesis is similar to that of the above researchers except for the fact that the resistance calculated using Inoue-Maekawa conduction equation [25], given in eqn.1.6. When calculating the effective resistance of new structure, the solver treats the insertion layer as insulator. All connections through this insertion layer will have a larger tunneling distance and hence a larger resistance. The electrodes on the right and left hand side are assumed to be shorted to all the grains on the right and left hand side borders of the 3D cube to facilitate easier calculation. Multiple MR curves are obtained because of the multiple M-H loop generated through the 'seed' option discussed in the previous section. The multiple conductance values obtained at various magnetic fields are averaged, filtered and smoothed to obtain the simulated curve. The obtained MR is a function of conductance through all the grains in the system and hence form the ideal basis. The variation of MR ratio with field is plotted in the figures where the MR ratio at a particular field is calculated in this case is $(R_{field} - R_{max})/R_{max}$. G_0 is not calculated for the system as it gets canceled out during the MR ratio calculation. However, a detailed analysis is done to obtain the relative value of this parameter in section4.3.1. Of all the resistor network solvers described in chapter 1, nodal elimination [112] is utilized because of the robustness and adaptability of the technique. Since it works by eliminating one node at a time, it can handle scaled networks with higher number of nodes. It is a one time implementation which will adapt itself scaled networks.

Nodal elimination : A network of resistors can be characterized as a set of nodes with connections between them. Each of these nodes is given an index i assigned a voltage V_i. Each connection between nodes, say i and j, has a conductance denoted by g_{ij}. The nodes are either internal nodes or external nodes, the latter being the

nodes that are connected in some way to the surroundings, typically a voltage source or a current source. It is allowed to remove a node, say 0, from the system if all connections, already existing or not, between the neighbors of node 0 are updated. The additional conductivity between node j and k is given by [112]:-

$$\Delta g_{jk} = \frac{g_{0j} g_{0k}}{\sum_{i=1}^{n} g_{0i}} \tag{4.3}$$

which is a generalization of star–delta substitution (fig.4.3). This method can be used to solve 2D and 3D matrices of any size.

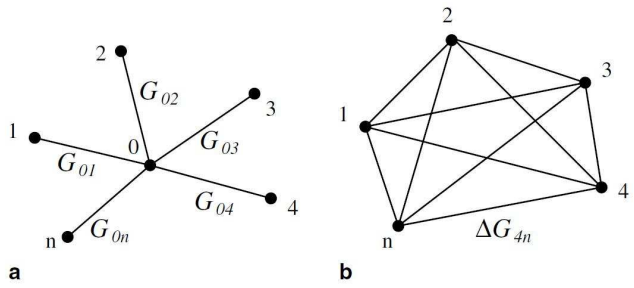

Figure 4.3: Illustration of Nodal Elimination (with 6 nodes) (a) The state before removing node 0. (b) After removing node 0 - The network is equivalent to (a), provided the additional conductivities are calculated from Eq. 4.3 [112]

Programming

This whole model was implemented using MATLAB, FORTRAN and C available at NUS High Performance Computing [2]. The analytical tools and resources provided are apt for the given problem. MATLAB has the concept of cell structure which is the basis for our calculations. A matrix of cells is used for solving the resistor network problem. Each cell represents a grain and can store the co-ordinates of related grains and their resistance value. This cell can expand to accommodate new correlation or existing correlations can also be removed. The nodal elimination is

[2] http://www.nus.edu.sg/comcen/HPC/

implemented on these cells to find out the resistance of the structures.

4.3 Result

The parameters varied in the Chantrell's simulator are grain size, its spread and Co volume fraction. The data fitting for G and X_{5nm} is as shown in fig 4.4 and it can be observed that the fit is good. The table shows the obtained grain size values for all the structure using the model. The trend for the grain sizes are comparable with those values obtained from the ZFC/FC measurement in Chapter 3. It must be noted that the M-H loop fit is a visual fit and because of size of the matrix used for generating the model is small compared to what was actually used in experiments, the low field magnetic response is noisy compared to higher fields.

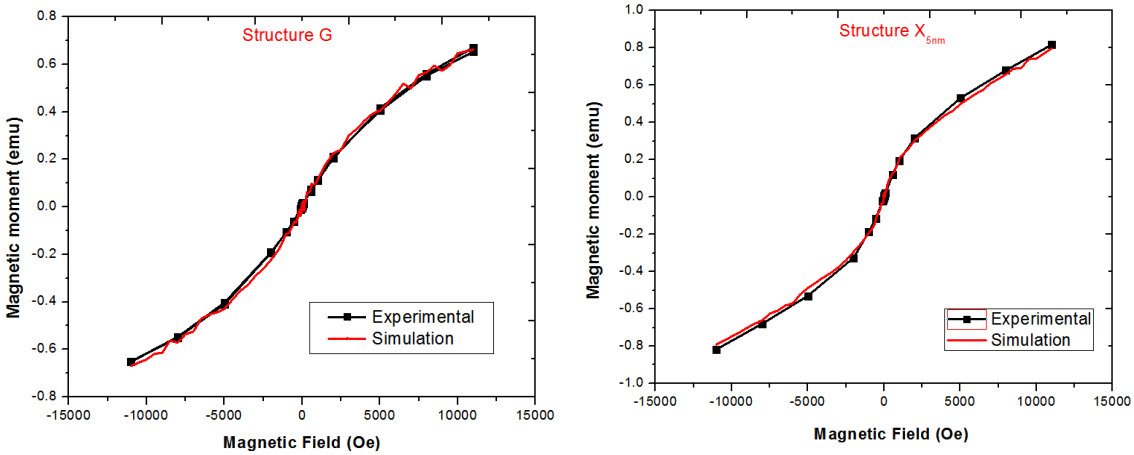

(a) (b)

Figure 4.4: Experimental curve and the simulation fit for a) Sample G and b) X_{5nm}

Using the location of the grains, the resistance at each field is calculated for each of the curves. The obtained resistance values cannot be compared as such because G_0 is not calculated . However it can be approximated assuming G_0 as a constant.

Structure	Grain diameter (nm)	
	μ	σ
G	2.73	0.47
2G	2.51	0.475
$X_{1.5nm}$	2.49	0.57
X_{3nm}	2.405	0.43
X_{5nm}	3.07	0.41
X_{10nm}	3.05	0.32
X_{15nm}	2.914	0.34

Table 4.1: Grain size calculation based on the simulation model from the experimental M-H loop (chapter 3, section 3.4)

4.3.1 Understanding G_0 on a comparative basis

G_0 is the conductance when the polarization is zero. For making the analysis simpler, it will be assumed that every 10 bilayers (thickness of G) can be translated to a series of one-dimensional grains (say 4 in this case) as shown in the fig 4.5. Furthermore for the G_0 calculation it shall be assumed that all the grains and the horizontal separation are same. Then conduction between the grains is given by [116]

$$g' = K_1 e^{-\beta d} \tag{4.4}$$

where

$K_1 = \frac{2e^2}{h}$, e is electron charge and h is the Planck constant

β is the constant which depends on the system and is usually equal to the work function and

d is the distance between the grains.

For sample G with 10 bilayers, the conductance depends on the product of tunneling probability from grains a→b→c→d

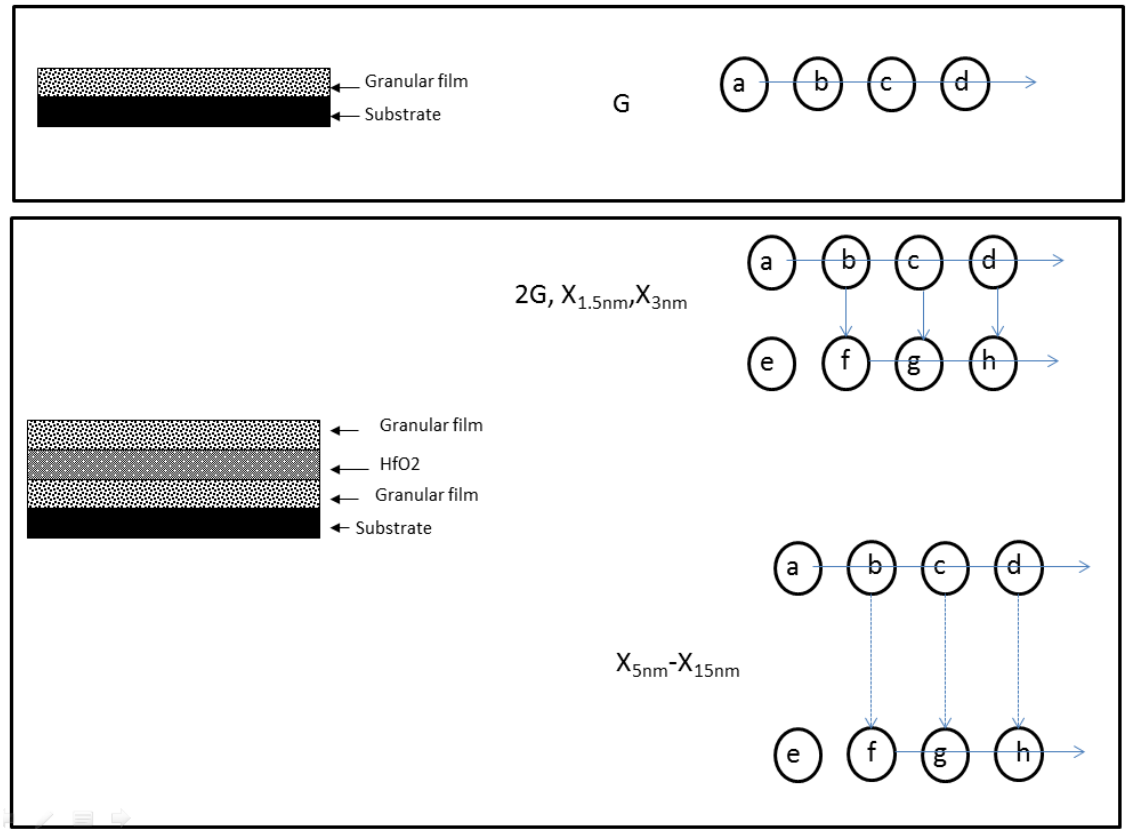

Figure 4.5: Schematic showing the assumption and calculation of G0

$$g' = K_1 e^{-\beta d} K_1 e^{-\beta d} K_1 e^{-\beta d} = K_1^3 e^{-3\beta d} = g_{base} \tag{4.5}$$

Similarly, in case of sample 2G, the conduction for the top film is sum of the conductivity from

a→b→c→d +

a→b→f→g→h +

a→b→c→g→h+

a→b→c→d→h

a→e→f→g→h

Here we assume for simplictiy that the vertical separation between the grains is equal to the horizontal separation. Hence the equation of conduction becomes

$$g' = K_1^3 e^{-3\beta d} + 4K_1^4 e^{-4\beta d} = g_{base}(1 + 4K_1 e^{-\beta d}) \tag{4.6}$$

Since similar contribution is made from the bottom chain of the grains the conductivity become twice of the above and is given by becomes

$$g' = 2g_{base}(1 + 4K_1 e^{-\beta d}) \tag{4.7}$$

It should be noted that though the vertical separation increases for $X_{1.5nm}$ and X_{3nm}, these two structures can be represented by above equation.

It was shown in chapter 3 that for thickness of insert above 5 nm, the insert is continuous and the top and bottom films are separated from each other. Therefore, for $X_{15nm \geq t \geq 5nm}$, the conduction probability between the top and bottom grains is very low and can be eliminated. This leads to the formation of parallel path in the CIP device and therefore the conductivity value is approximately twice that of sample G.

$$g' = 2K_1^3 e^{-3\beta d} = 2(g_{base}) \tag{4.8}$$

So keeping g' for sample G as reference (g_{base}), conductivity at zero polarization can be approximated as shown in the table 4.2. The resistance trend obtained using simulations can be correlated to the experimental resistance using the above factor of G_0/g_{base}.

Figure.4.6 shows both the experimental and simulated resistance values for the structures discussed in chapter 3. Although, the experimental trend has already been described in section 3.5, it is explained again in this section for easy reference.

Structure	$G_0^{'}$= ~(G_0/g_{base})
G	1
2G, $X_{1.5nm}$ and X_{3nm}	>2
X_{5nm} - X_{15nm}	2

Table 4.2: G_0/g_{base} with sample G as references

It can be observed that the experimental resistance drops as the thickness of the standard structure is increased from G to 2G. This is because of additional number of tunneling paths available in 2G compared to G [6,83]. When an oxide thickness of 1.5 nm is inserted in between 2G, the roughness increases and grain size distribution has a higher spread and the structure $X_{1.5nm}$ has higher resistance compared to the rest. As the thickness of the insert increases to 3 nm, the discontinuity and roughness of the insert decreases and this leads to formation of grains with less spread. So the resistance decreases compared to $X_{1.5nm}$. As the thickness of the insert is increased beyond 5 nm, the insert layer becomes continuous with lower roughness, leading to formation of larger grains in the top layer of the structures. The top layer plays an important role in the conduction and the resistance for X_{5nm}, X_{10nm} and $X_{15nm}$are very close to each other.

The simulation model considers all the possible tunneling paths between the grains and hence generates a complex resistive network. However, it has the advantage that very high resistance paths will be eliminated automatically during the network solution. For e.g if there are two resistances in parallel say R_1 and R_2 and if $R_1 >> R_2$, it is known that the effective resistance is R_2. It must be noted that G_0 in eqn.1.6 has not been calculated during the simulation, rather it has been analyzed on a comparative basis in section 4.3.1. The simulated resistance for G is approximately 680 Ω while that of 2G is to 4000 Ω. The resistance increases to 20,000 Ω for $X_{1.5nm}$ and drops to 2000 Ω for X_{3nm}. For $X_{15nm \geq t \geq 5nm}$, the resistance values are similar and approximately equal to 250 Ω. If the factor of G_0(~2) is con-

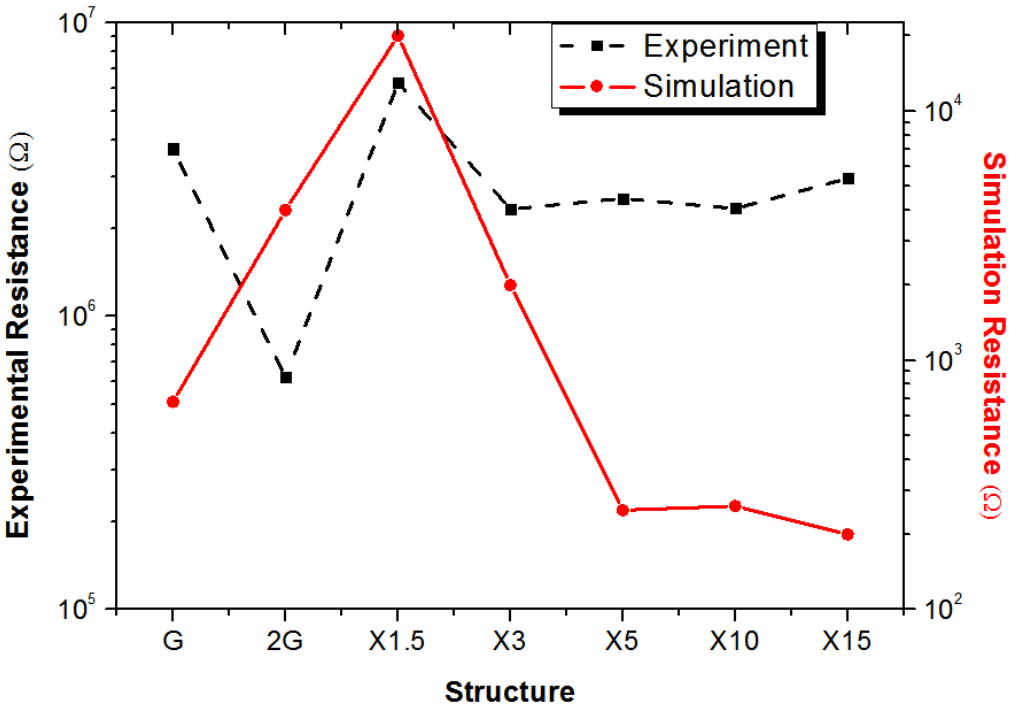

Figure 4.6: Resistance for different structures- experimental (black square) vs. Simulation (red circle), showing the similarity in trend for the experiment as well as for simulations (the difference in trend for structure 2G can be explained by using G_0

sidered for samples $X_{15nm \geq t \geq 5nm}$, then the resistance can be compared to sample G and it is found to 500 Ω. This resistance is lower than that of G and corresponds to the result in chapter 3. Similarly once 2G is normalized with respect to $G_0(>2)$, the resistance may become lower than that of G following the resistance trend. Similarly for $X_{1.5nm}$ and X_{3nm} the normalization factor will be closer to value of 2 and the resistance trends observed for simulation matches that of the experiments. Figures.4.7 & 4.8 show the simulated curve fitting for the experimental curves for G, 2G, $X_{1.5nm}$ and X_{3nm} matches quite well.

The simulation model will generate the same grain size and boundary condition for the structures with the continuous oxide. This is a limitation based on the particle generation and shrinking. Therefore the simulator cannot generate films having different top and bottom layer grain size. We propose a method to overcome

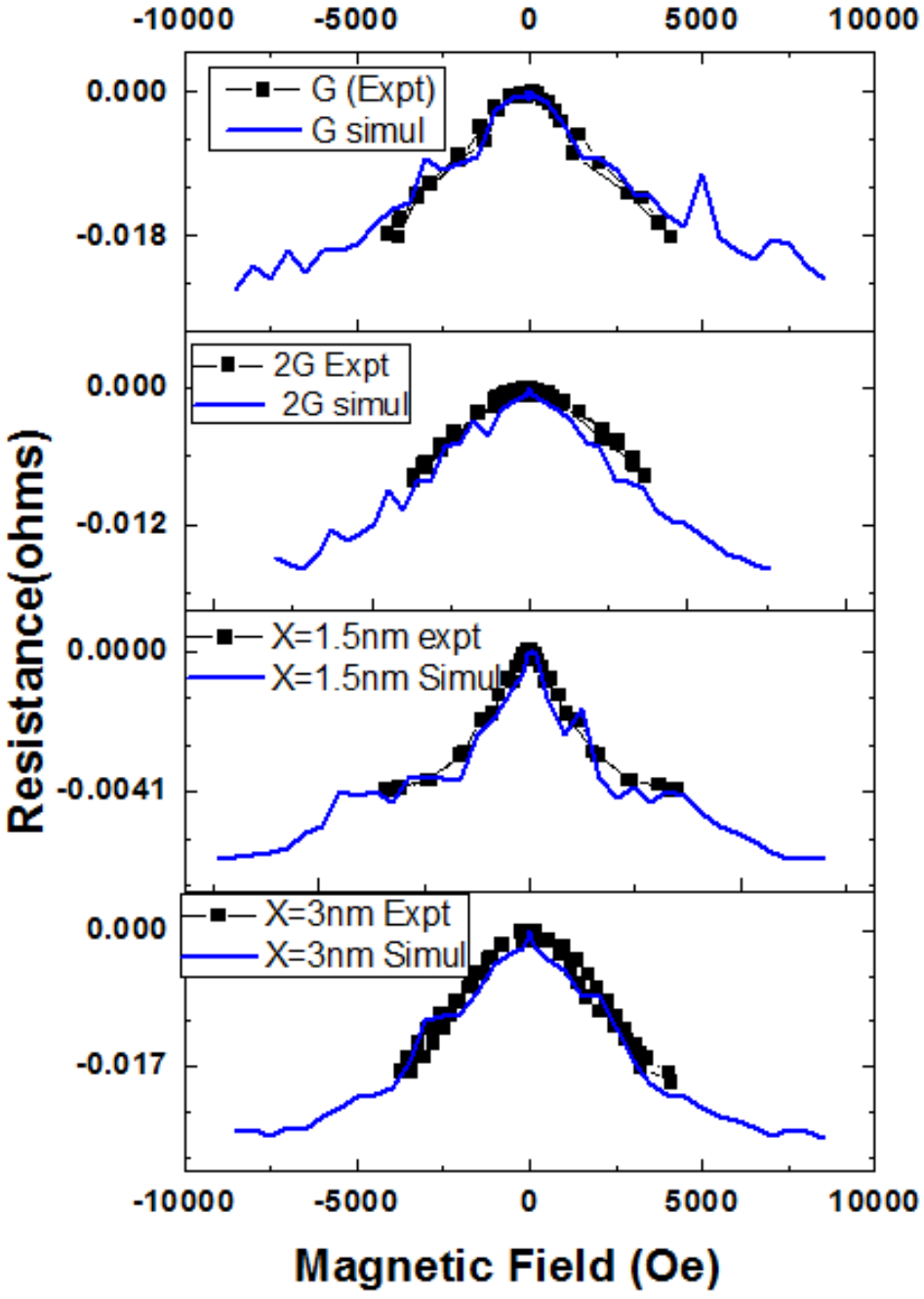

Figure 4.7: Graph showing the fitting of the simulation MR curve with that of the experimental for G, 2G, $X_{1.5nm}$ and X_{3nm}

this issue. From experimental results it is known that for structures with oxide insert greater than 3nm, the actual path of conduction is majorly through the top granular film layer. So by generating the MR for single layer corresponding to the top granular film layer we can verify the observation. So the M-H loop contribution from the top layer (fig.3.8b) is used to generate grains for the single layer device and then the MR curves are obtained for for X_{5nm}, X_{10nm} and X_{15nm} using the same. It can be seen from fig.4.8 that the simulated curve fits well for X_{5nm} but not for X_{10nm} and X_{15nm}. This is most probably due to the leakage conductivity seen in the experimental MR (discussed in section 3.5). Hence the simulated MR curves represent the ideal MR case for X_{5nm}, X_{10nm} and X_{15nm}.

The whole simulation model was implemented with and without dipolar coupling and it was found that it did not have an effect on the output of the simulator indicating the fact that there is minimal interaction in these films for the given Co volume fraction . This was already shown in chapter 3 (table 3.3) where the systems are found to be weakly antiferromagnetic.

It should be noted that the fitting and implementation is done only for CIP devices. The resistances are calculated on the eq. given by Inoue and Maekawa and high field induced tunneling factor is not part of the equation. Therefore, the MR calculated for the CPP system was found to have different resistance compared to the case of CIP, but the MR ratio obtained was still the same. This simulation model is quite useful for CIP systems where the high field induced tunneling is negligible. For the case of CIP, the M-H loop fitting was done for different grain array size (10 x 10 x 10 and 20 x 20 x 20) using the same volume fraction and the median grain size was found to be the same. It was found that though the resistance changes with the size of the device (10 x 10 x 10 vs. 20 x 20 x 20) the MR ratio remains unchanged. This suggests that the 10x10x10 model serves a good model

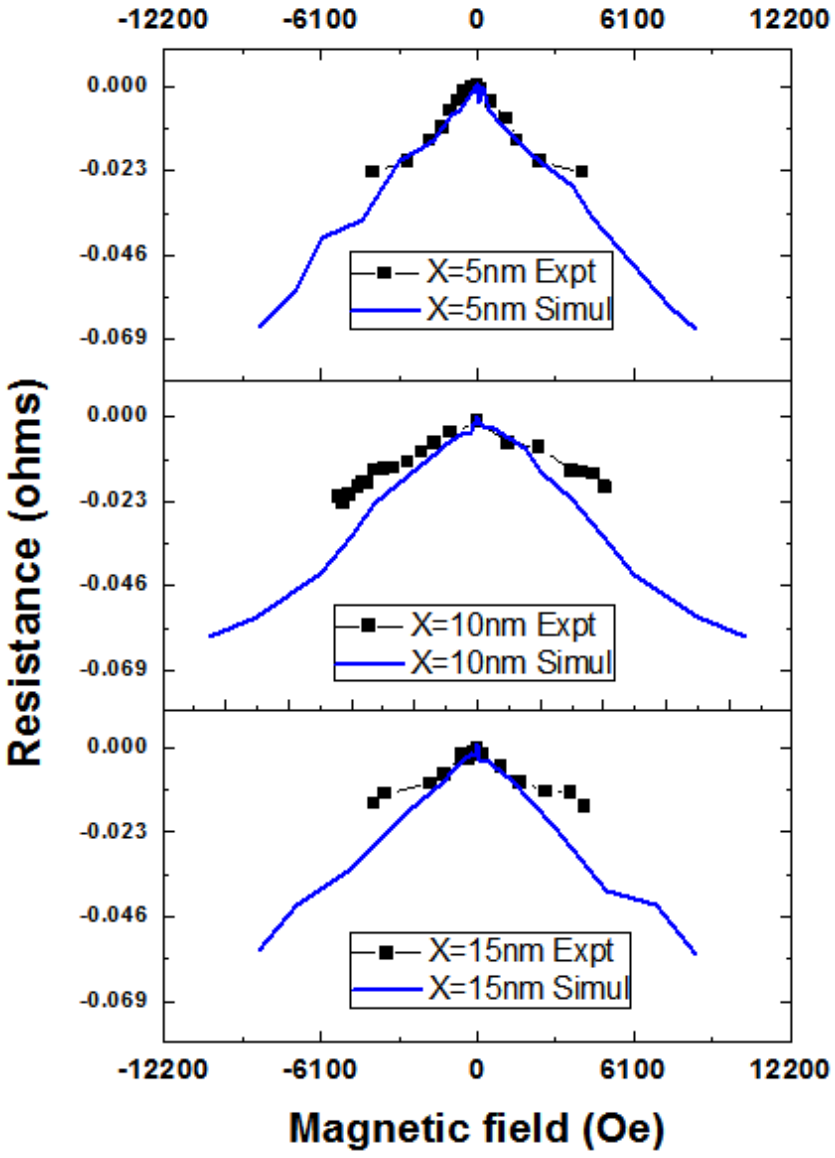

Figure 4.8: Graph showing the fitting of the simulation MR curve with that of the experimental for X_{5nm}, X_{10nm} and X_{15nm}

for the CIP structures discussed in chapter 3 of this thesis. This grain size array is a good representative of the overall microdevice and although the number of grains is lesser along the width and length as compared to the experimental structure, the electrical properties matches well for most of the structures.

4.4 Summary

A simulation model based on code by Chantrell et al. [82] was used to generate the grain size distribution based on the experimental M-H loop. It was found that the grain sizes obtained using this method followed the same trend as the those obtained using experiments in chapter 3 of this thesis. The G_0 term in Inoue Maekawa's equation is actually the conductance in granular film when polarization is zero. It was analyzed and found to be the highest for 2G followed by $X_{1.5nm}$,X_{3nm}, X_{5nm}, X_{10nm},X_{15nm} and G. This term was very useful in explaining the resistance values obtained using the simulation and enabled to compare it with the experimental results. The MR curve trend obtained by simulation matches the experimental values except for X_{10nm} and X_{15nm} which show higher MR ratio using simulations as compared to experiments. This is because of two reasons: first, the model assumes the top and bottom layer of these structures to have the grain size distribution , second, presence of leakage conductivity as verified by experiments in chapter 3 of this thesis.

Chapter 5

CIP and CPP devices based on insertion of oxide layer in Co-HfO_2 granular films

A detailed analysis of current in plane (CIP) devices based on the proposed structure of inserting oxide layer in between the granular film was done in the chapter 3. It was found that the grains in the top granular film are larger in the case of continuous inserts and hence the MR ratio is higher because of major conduction through this layer. However, it would be of interest to force the conduction through both the layers and observe the MR and resistance characteristics of the films. This can be achieved with the help of current perpendicular plane (CPP) devices. Therefore this chapter compares the device performance in terms of resistance and MR ratio for current in plane and current perpendicular plane devices based on Co-HfO_2films. The same film structures as in chapter 3 are compared for the CPP devices as shown in table 5.1. The active regions for both the CIP and CPP devices were sputtered together.

The photolithography process for the CIP devices has been explained in chapter

Sample	Composition
G	$[Co(0.8\ nm) + HfO_2(1.1\ nm)]_{10}$
2G	$[Co(0.8\ nm) + HfO_2(1.1\ nm)]_{20}$
X_n	$[Co(0.8\ nm) + HfO_2(1.1\ nm)]_{10}$ + $[HfO_2(n)]$ + $[Co(0.8\ nm) + HfO_2(1.1\ nm)]_{10}$ where n=1.5, 3, 5,10 and 15 nm respectively

Table 5.1: Composition of the standard films(G,2G) and the proposed structure($X_{1.5nm}$, X_{3nm}, X_{5nm}, X_{10nm} and X_{15nm})

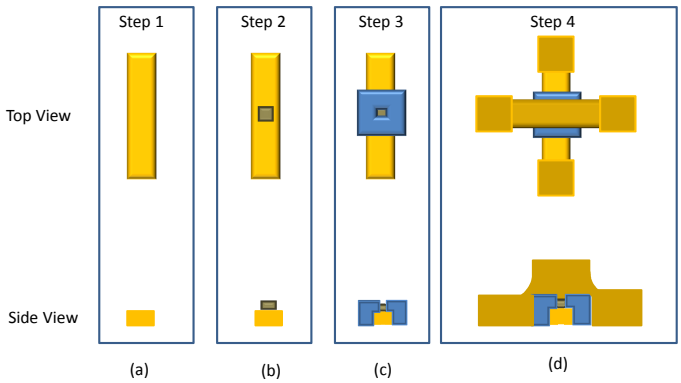

Figure 5.1: Sequence showing the four lithography steps and material deposition for making CPP devices a) Bottom electrode (Cr/Au) b) Active device c) Oxide layer surrounding the active layer(to prevent short between top and bottom electrode) d) Top electrode and bond pad deposition

2, while that for the CPP device is shown in fig. 5.1. The first layer consists of ~ 40 nm of Cr/Au which serves as the bottom electrode for the conduction. The second step consists of depositing the active device layer of 20-60 nm thickness. The active device layer area is ~10 μm × 10 μm . The deposition follows the condition given in the table 5.1 for each of the device. The third step consists of SiO_2 oxide deposition surrounding the active layer to prevent shorting between the top and bottom electrode. The last step consists of top electrode and pad deposition using Cr/Au of 300 nm thickness.

The samples are finally wire bonded for electrical measurements namely I-V and MR measurement on the CIP and CPP devices at room temperature. Reference

samples for M-H loop measurement and other measurements are inserted during the active layer sputtering process. RBS is again used for compositional analysis while M-H loops is used to understand the variation in grain size distribution.

5.1 RBS and M-H loop

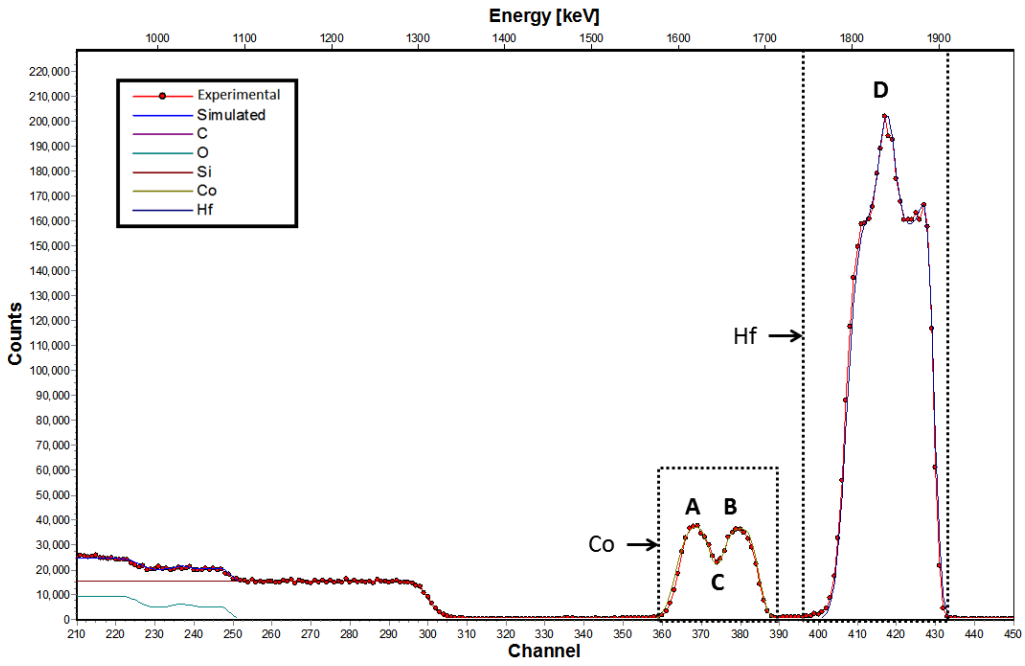

Figure 5.2: RBS data for X_{10nm}: Markings A,B,C corresponds to Co content in bottom,top and center of the film respectively while D represents the Hf composition across the multilayer (peak showing the content in the central layer) - Able to observe the separation between top and bottom granular film for a volume fraction of 0.355

fig. 5.2 shows the RBS obtained for sample X_{10nm} and as observed in the previous chapter, the sample shows separate Co and HfO_2 peaks, with obtained Co volume fraction of 35.5 % .

Figure. 5.3a shows the M-H loop for the samples while fig. 5.3b shows the M-H loop with magnetic moment for X_{5nm} to X_{15nm} subtracted by that of structure G. This has been explained in chapter 3 section 3.5,where the bottom granular film has

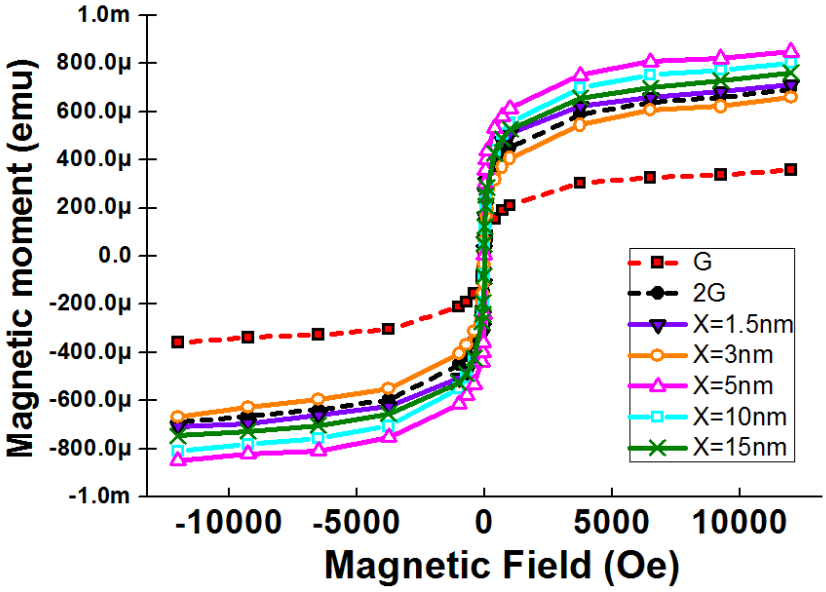

(a)

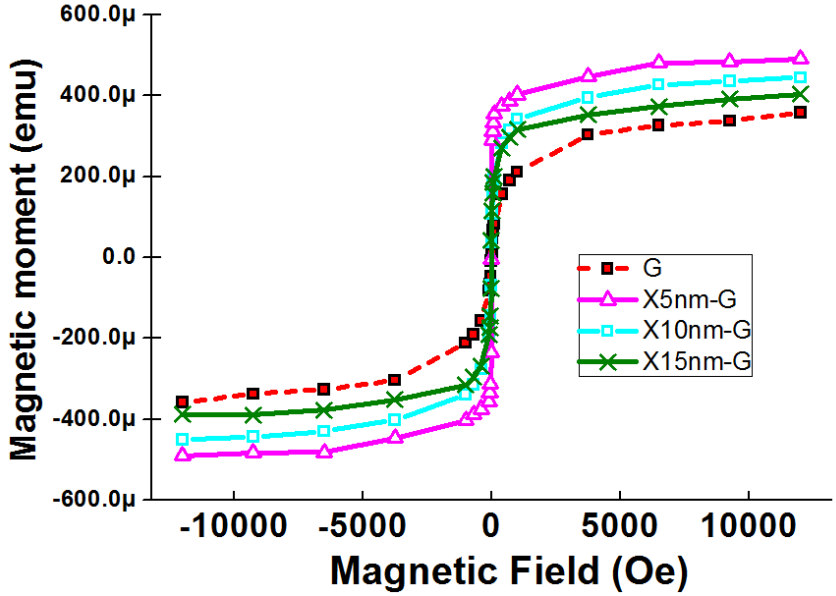

(b)

Figure 5.3: M-H Loop for a) G, 2G and the proposed structures b) Magnetic moment for X_{5nm} *to* X_{15nm} (after subtraction with that of G)

similar structure as G and so the subtraction helps to find the magnetic moment and grain size contribution from the top layer of these structures. It can be seen that the moment contribution from the top layer for X_{5nm},X_{10nm} and X_{15nm} is greater than that of G in the same order. This shows that top layer has larger grain size than the bottom layer in these structures [6, 100].

5.2 Resistance and MR results

5.2.1 Preliminary study : Resistance and MR study for G and 2G

It is essential to understand the differences between the CIP and CPP related resistances and MR as it helps to understand the effect of overall tunneling length on properties of these structures. For basic understanding, R and MR values of samples G and 2G have been compared for the case of CIP and CPP. The table 5.2 shows the R and MR ratio for sample G and 2G for the case of CIP and CPP devices. The overall tunneling length for CPP devices is equivalent to thickness of the device and is ~20 nm and ~40 nm for G and 2G. The overall tunneling length in the case of CIP devices is ~3.6 μm for both G and 2G. It can be seen from the table that CPP MR is always lower than CIP MR. This trend shows that channel length plays an important role in deciding the MR and is lower for smaller length scales. It should be noted that the voltage across the CPP devices causes high field induced tunneling in these structures as opposed to CIP devices. As a result the CPP devices give lower MR than their CIP counterparts. Also if the channel length is small as in the case of CPP G, the no of grain is very less and the number of grains taking part in the conduction will be also lower. Hence the MR will not reflect all the characteristics of the grains. As the thickness of the CPP structure

increases(from G to 2G), the high field effect reduces and the number of grains taking part in the conduction also increases. That is the reason why 2G gives better MR than G for the case of CPP. However it is still lower than the respective CIP structures which are not affected by high field induced tunneling because of their larger channel length. In the case of CIP as the thickness increases, the MR actually drops and the probable reason for this is smaller grain size of 2G as compared to G observed in chapter 3. The CIP resistance of 2G is lower than G because of the increase in number of available tunneling paths

Structure	Effective channel length	Resistance	MR
CIP G	~3.6 μm	18.31KΩ	2.13 %
CIP 2G	~3.6 μm	15.17KΩ	1.40 %
CPP G	~20 nm	0.18KΩ	0.10 %
CPP 2G	~ 40 nm	0.32KΩ	1.05 %

Table 5.2: Understanding the R and MR difference for G and 2G for CIP and CPP configuration

5.2.2 Resistance

Figure. 5.4 shows the resistance trend for the CIP and CPP structures. The analysis of the resistance trend for CPP device can be explained by splitting the resistance contribution from three layers namely

a) top granular film (R1)

b) tunneling across the barrier from top to bottom granular film (R2)

c) bottom granular film (R3) and

as shown in fig. 5.5.

The zero field conductance contribution can be explained based on the conductivity term described by Inoue and Maekawa in their paper [25]

$$G = G_0(1 + Pcos\theta)e^{(-2\kappa s - c/sK_BT)} \tag{5.1}$$

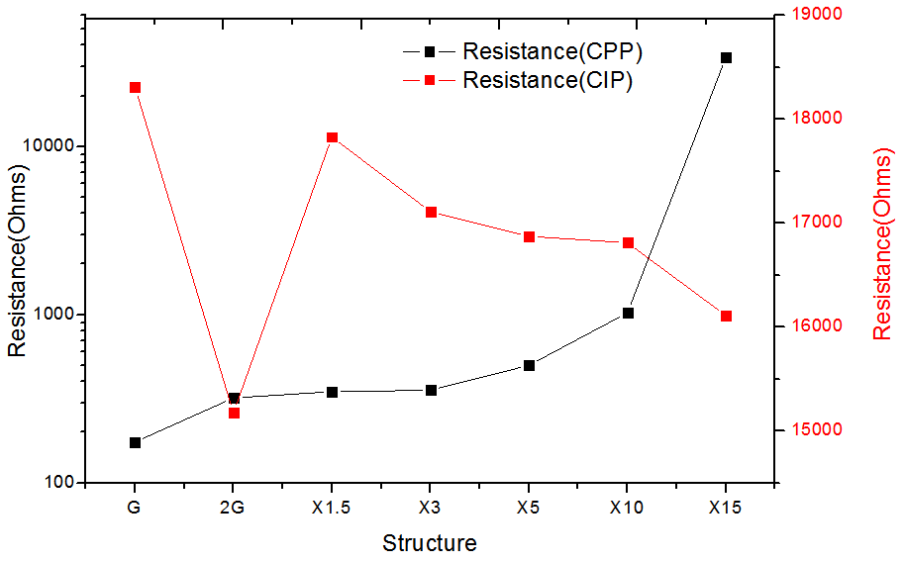

Figure 5.4: CIP and CPP resistance trend for G, 2G and $X_{1.5nm}$ to X_{15nm}. CIP trend is similar to what was observed in chapter 3. For CPP the resistance increases with increasing oxide thickness of the central layer

where $\kappa = \sqrt{\frac{2m_e\phi}{\hbar}}$, ϕ is the barrier height,

$c = \kappa s E_c$,

$E_c = 4s(e^2/\epsilon d)/(d + 2s)$ is the charging energy [23],

s is the thickness of the barrier between the grains d is the grain size, P is Co polarization factor and θ is the magnetic orientation of the grain with respect to the applied field and G_0 is the conduction when polarization is zero.

The first term in the exponent represents the tunneling between two electrodes separated by distance (s) and the second term accounts for the charging energy contribution for the grains. The following paragraph explain the trend for CIP and CPP case.

CPP device : In general, the resistance monotonically increases with thickness of HfO_2 insert for the CPP devices. The sample G would have less than 10 grains along the conduction path and hence the associated resistance is lower. Compared to this sample 2G has twice the number of grains and hence has higher resistance.

The films with 1.5 nm and 3 nm insert which do not have continuous central oxide layer show slightly higher resistance than 2G. Figure. 5.5 shows the equivalent resistor model for films having insert thickness greater than 5 nm. For these films, the resistance contribution layer from the bottom granular film (R3) are expected to be similar to that of sample G. Sample X_{5nm} followed by X_{10nm} and X_{15nm} has the largest grain in the top layer. So resistance is the top layer (R1) is lowest for X_{5nm} followed by X_{10nm} and X_{15nm}. Other than this, there is increase in resistance for tunneling across the central barrier which is related to the thickness of the inserted oxide. As a result, the resistance due to the tunneling component from top to bottom layer (R2) increases with increasing oxide thickness and so does the overall resistance. This is observed clearly in the fig. 5.4 that for CPP devices there is two orders increase in resistance from sample G (~200 Ohms) to sample X_{15nm} (~33,000 Ohms) because of the central tunneling barrier.

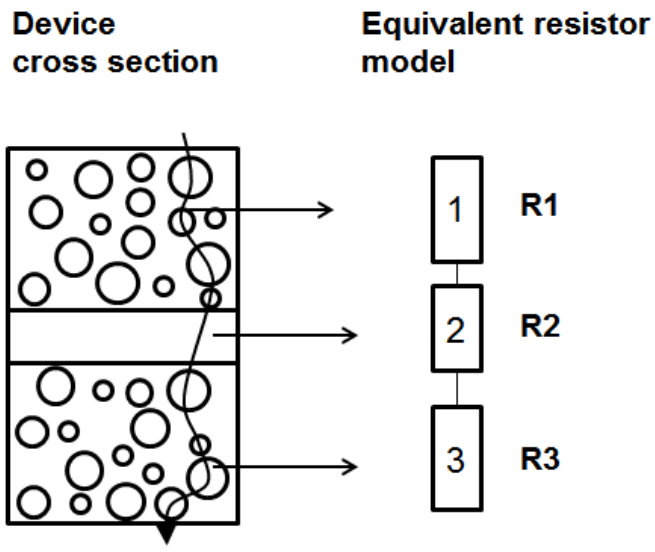

Figure 5.5: Equivalent resistor model for the CPP device with insert thickness greater than 5 nm

CIP device : The resistance trend for the CIP devices follows the trend explained in the previous chapter. Sample 2G being thicker than G has greater number

of tunneling paths and hence has a lower resistance [80, 83]. As far as the discontinuous inserted layers are concerned ($X_{1.5nm}$ and X_{3nm}), the resistance is closer to G than to 2G. This can be explained based on trend of roughness (fig. 5.6) as discussed in section 3.2 of chapter 3. Sample $X_{1.5nm}$ followed by X_{3nm} has maximum roughness because of the high discontinuity of the inserted oxide layer.

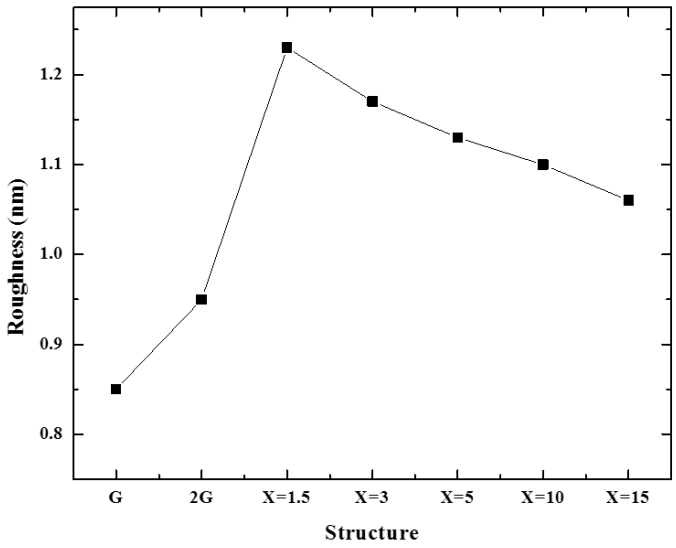

Figure 5.6: RMS roughness trend for G, 2G and $X_{1.5nm}$ to X_{15nm}

As seen in the previous chapter, it can be seen that the discontinuity causes the resistance behavior to be different from 2G and similar to that of G. In the case of continuous inserted oxide layer (X_{5nm} onwards), the bottom layer is sputtered in the same way as G and hence has the same grain size distribution as G. However, the grain sizes in the top granular film are influenced by the roughness of the underlying inserted oxide layer. The grain sizes in the top layer are comparatively larger than that of the bottom layer as seen from the M-H loops (fig. 5.3). Therefore the M-H loops for the samples with inserted oxide show a significant change in grain size distribution compared to G, which is the contribution from the top granular film layer. The CIP conduction can happen through the top or bottom layer or through both. If the conduction was through the bottom layer, the resistance is expected

to be equal to that of G. But the resistance seen in this case is slightly lower than that of G indicating the fact that the conduction is majorly due to the top layer of the film.

5.2.3 MR for CIP and CPP devices

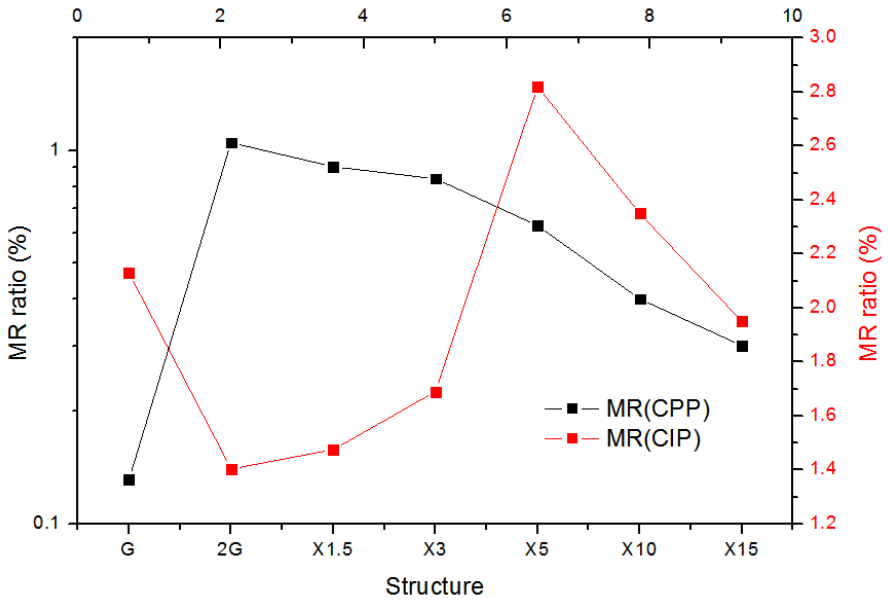

Figure 5.7: CIP and CPP MR ratio comparison for G, 2G and $X_{1.5nm}$ to X_{15nm}

Figure. 5.7 shows the MR trend for the CIP and CPP structures for in-plane magnetization measurement. In general MR for CIP is greater than that of CPP devices.Before going into the details, first the CIP and CPP MR curves for the samples are analyzed. Figs 5.8 and 5.9 show the MR curves for CIP and CPP measurement for all the samples and it can be seen that the MR curves for CIP and CPP devices are visibly different. It is known from chapter 3 that the CIP MR for structure with continuous insert is majorly due to tunneling in top layer of the granular film. The shape of the MR curves in the case of CIP curves follows the M-H loop. However for CPP case, it is not quite apparent. So the normalized resistance is plotted for X_{5nm} - X_{15nm} in fig. 5.9b. It can be seen that CPP MR

curves also follow the trend of the M-H loop, but are not as steep as the CIP MR curves. This trend is valid for rest of the structures also and indicates that not all grains in the CPP structure take part in conduction. The other reason is presence of high electric field tunneling in CPP structures [6,37]. The structure X_{5nm} has the highest improvement in CIP MR ratio and it verifies the result obtained in chapter 3.

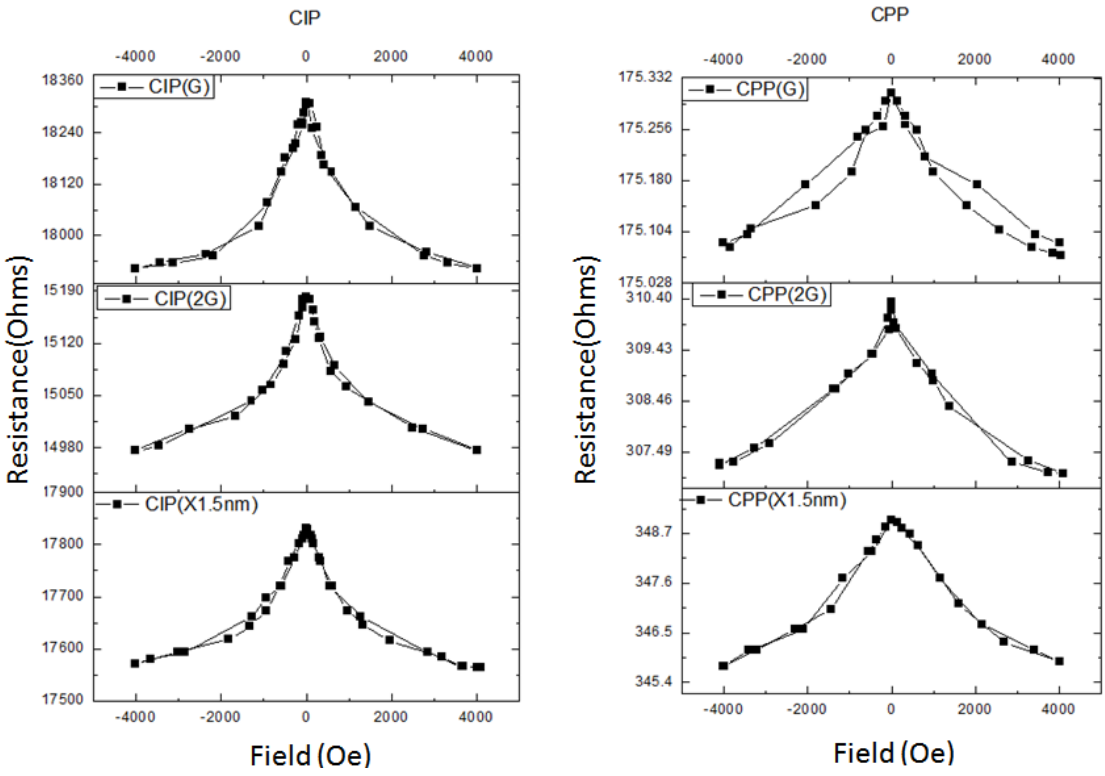

Figure 5.8: CIP and CPP MR curves for samples G, 2G and $X_{1.5nm}$

CPP device : The CPP MR trend in fig. 5.7 shows that that the MR for the CPP structures is lower than that of CIP structures. This is due to the average number of grains traversed by the electrons through the devices [37]. In case of CIP device, the electrons have to tunnel through ~4 μm along the device, whereas in the case of CPP device the electrons have to travel the effective thickness of the device, which is ~55 nm for X_{15nm}. The number of grains in between the electrodes

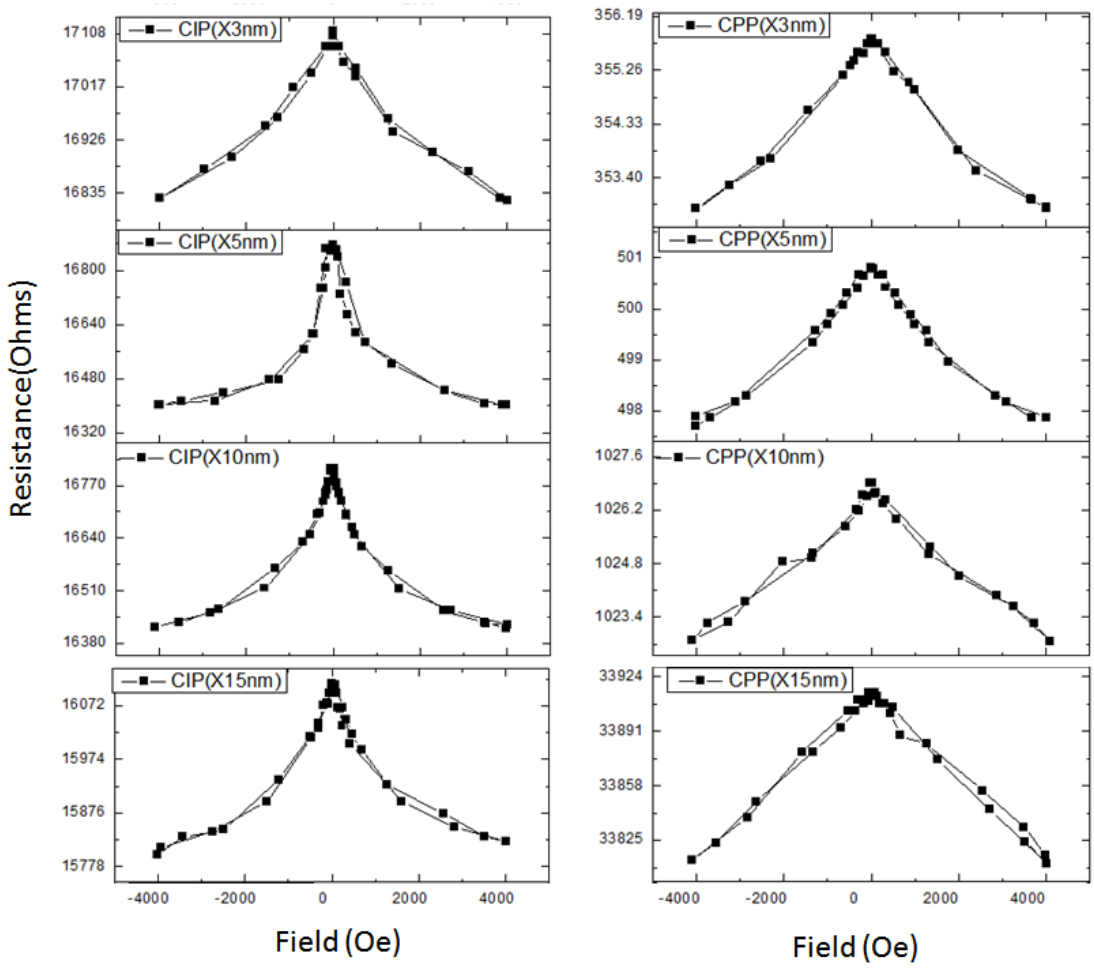

(a)

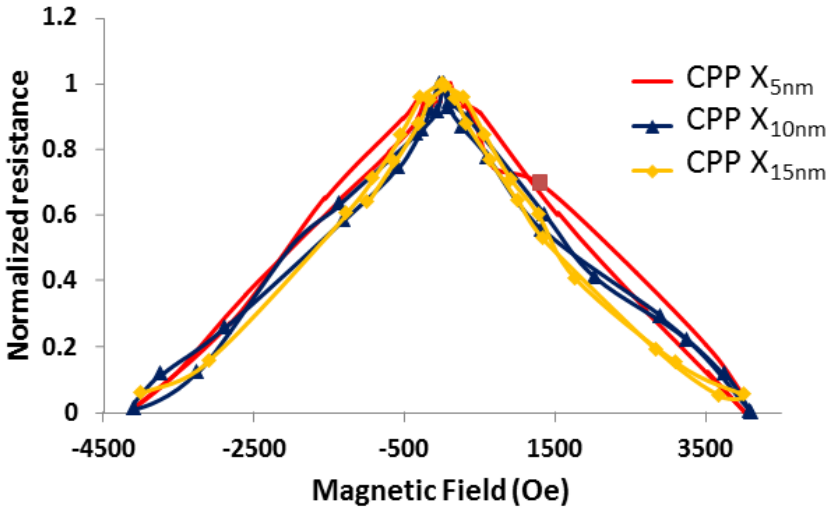

(b)

Figure 5.9: a) CIP and CPP MR curves for X_{3nm} to X_{15nm} (b) Normalized CPP MR graph for X_{5nm}- X_{15nm} showing that M-H loop trend is weakly followed in this configuration

of a CIP device(~1000 grains) is far higher than those in case of CPP device (~10 grains).Hence the number of grains traversed in the CPP case is far lower than CIP leading to the visible difference between the values of MR. The other issue is the effective field experienced by the grains in a CPP device is far higher than that for CIP because of the effective channel length. This leads to high field induced tunneling in CPP devices and hence lower effective MR as this effect is independent of magnetic field [37, 102]. Kakazei et al. observed this effect for discontinuous metal-insulator (DMI) multilayer of $Co_{80}Fe_{20}$ and Al_2O_3. They found the MR ratios to be ~6.5 % and ~2.3 % for CIP and CPP respectively at room temperature and attributed the difference to be due to high electric field regime effect for CPP [37].

In case of sample G and 2G, the films are homogeneous and the since G is thinner than 2G, the conduction path is smaller leading to a lower MR than 2G. The CPP resistances and MR are very similar for the case of 2G, $X_{1.5nm}$ and X_{3nm} as the inserted oxide layer formed is not continuous. But in case of the X_{5nm}, X_{10nm} and X_{15nm} the inserted oxide becomes continuous and hence the obtained MR is different from the rest of the samples. As seen from the fig. 5.5, the resistance and MR component can be broken into three components: top, central and bottom. The top and bottom contributions are from top and bottom granular films respectively whereas the central component refers to the bottleneck tunneling from the top to the bottom layer in the granular film. Then the MR ratio for $X_{n>5nm}$ is given by

$$MR = \frac{\Delta R_1 + \Delta R_2 + \Delta R_3}{R_1 + R_2 + R_3} \tag{5.2}$$

where ΔR_m and R_m are change in resistance and resistance contribution from each of the three layers described in 5.5. From the M-H loop it is known that the saturation magnetic moment at ~ 10 kOe is greater for the $X_{n>5nm}$ structures compared to 2G or G. Since the bottom layer for $X_{n>5nm}$ has same grain size distribution as G, the

top layer contributes more to the magnetic moment as seen from the M-H loop and therefore has comparatively larger grain size than the bottom layer. It is know that the conduction between grains can be expressed by eq. 5.1 where the term θ is the angle between the magnetization of the grains. If the two grains are well oriented along the field θ is small and if the grains are not oriented θ is large. Larger grains will orient themselves much easily along the field and tunneling between them will have lower θ as compared to smaller grains. Therefore conductance is higher for larger grains at a given field as seen from eq. 5.1. From this it can be concluded that $\Delta R_1 > \Delta R_3$ and it is known from the previous section that $R_1 < R_3$. Therefore the effective MR change contribution for the top layer is higher than the bottom layer. This analysis is based only on spin dependent tunneling and does not consider high electric field induced conductivity which is actually magnetic field independent [37] and leads to MR ratio reduction.

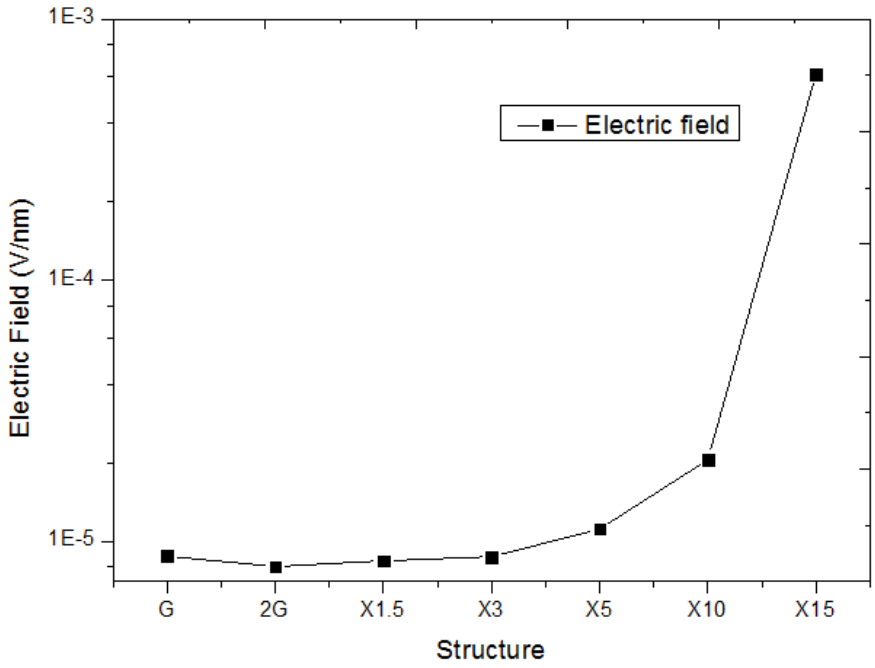

Figure 5.10: Calculation of electric field across the various device structures(G, 2G and $X_{1.5nm}$ to X_{15nm}) by passing a constant current of 1 μA and measuring the resistance

The measurement for the case of the CPP structures is done by passing a constant current of 1 μA and the resistance is measured. From this the approximate electric field across can be calculated and is plotted in fig. 5.10. The electric field across structure G is

8.7 $\mu V/nm$ and it drops to 8 $\mu V/nm$ for structure G. So sample G has not only smaller channel length but also higher electric field leading to a drop in MR. As the thickness of the insert is increased from 1.5 nm to 15 nm, the electric field changes from 8.41 $\mu V/nm$ to 616 $\mu V/nm$. So the effective field across oxide layer increases with thickness of the oxide layer and starts to affect the high field induced tunneling [37] leading to lower MR ratios.

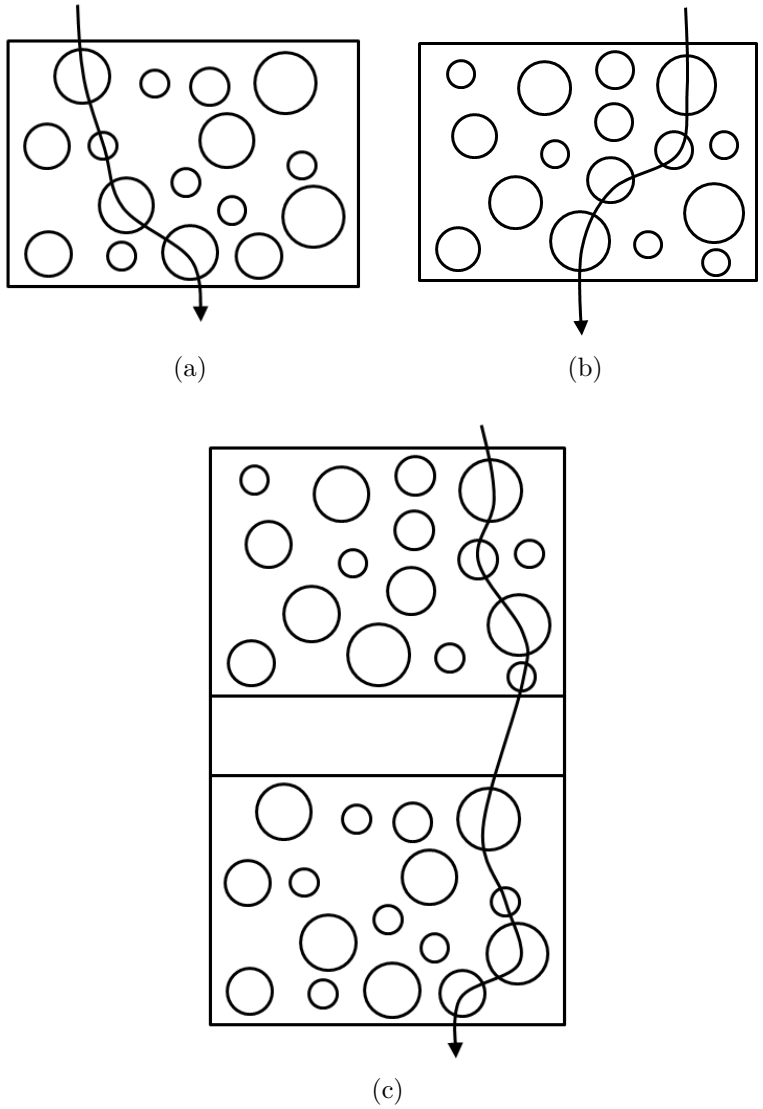

Figure 5.11: Illustration of CPP conduction a) bottom granular film only b) top granular film only c) both top and bottom film in the proposed structure

Other than this, we can do further analysis on the CPP conduction by individually separating the top and bottom granular films layers and understand the conduction. Then the most probable conduction path when the individual films are considered, will be based on grain size and charging energy for that particular layer such that lowest resistance is obtained. This is shown in fig. 5.11(a) & (b). However when both the films are considered as one single device structure along with

the inserted oxide layer, the effective conduction mechanism in each layer becomes interdependent. The inserted oxide layer has its own roughness and it becomes the most crucial factor for conduction. It is already known that the top layer has larger grains compared to the bottom layer. When considered as individual films, the former and latter will have different probable paths for conduction. However when they are part of the same structure the path maybe totally different than in individual films because of the grain location,roughness and thickness of the inserted oxide. In other words, the central tunneling layer between the the top and bottom granular film plays an important role in the choice of tunneling paths. Because of the restriction on the tunneling paths due to this layer, grain sizes involved and the number of grains involved in conduction, the overall MR ratio reduces for the inserted oxide films as compared to sample 2G.

CIP device : As far as the CIP MR is concerned, the MR trends at room temperature are similar to the experimental results discussed in chapter 3. The M-H loops (fig. 5.3) for 2G, $X_{1.5nm}$ and X_{3nm} deviate only by a small margin. Generally, they have similar grain sizes, but their resistances and MR ratios are very different because of the discontinuity of inserted layer which affects the grain morphology and hence causes a change in conduction and MR ratio for CIP devices. The MR variation for the films with continuous inserted layer follows the magnetic moment trend for the same namely, X_{5nm} followed by X_{10nm} , X_{15nm} and 2G gives the best MR ratio. X_{15nm} gives lower MR ratio than G because of reasons explained in section 3.5.5 of chapter 3 based on leakage conductivity.

5.3 Summary

In this chapter, the effect of introduction of different thickness of the inserted oxide was studied for both continuous and discontinuous inserted oxide for CIP and CPP

devices. The CIP conduction is different because the CIP conduction is through the top layer whereas the conduction for CPP devices is through both the layers. The number of grains taking part in the conduction for CIP and CPP devices are different. The effective conduction length (through the granular film) for CIP devices is ~4 μm whereas it is maximum of ~40 nm for CPP devices. Therefore the CIP devices have approximately 1000 Co grains whereas CPP has approximately 10 Co grains along the tunneling path (because of channel length), leading to a higher resistance in the case of CIP devices compared to CPP devices. Also the high electric field tunneling is dominant in CPP structures which is magnetic field independent and hence the MR ratios for CPP devices is lower compared to CIP devices. As observed in the previous chapter amongst the CIP devices, the continuous inserted oxide have a better MR and resistance than the standard structure 2G, indicating the fact that inserting an oxide layer enhances both the resistance and MR ratio by changing the grain size distribution along with the roughness. In the case of CPP, the inserted layer causes a reduction in number of tunneling paths and this coupled with the fact that the length of the conduction channel is smaller (high electric field) than the CIP devices gives a lower MR for all the inserted oxide devices. This shows that as the thickness of the CPP devices without oxide insert is increased it will lead to improved MR ratio.

Chapter 6

CPP devices based on insertion of soft magnetic layer in Co-HfO_2 granular films

Chapter 5 discussed the difference between CIP and CPP devices based on the HfO_2 insert and it was found that CIP MR ratios are always higher than CPP devices. The tunneling between the grains is dependent on magnetic orientation of the grains as well as the charging energy of the grains. However the thermal generation of electrons as well as the high electric field induced tunneling are undesired in such samples. The high electric field induced tunneling being less sensitive to magnetic field causes lower MR in CPP devices. We investigate a method to enhance magnetic field and overcome the high electric field effect in CPP devices.

To enhance magnetic field, soft magnets are used in conjunction with granular films. The most common method is the Granular in gap (GIG) structure described in chapter 1, which consists of a granular film in between a couple of soft magnetic metal films [7]. The large magnetic flux equal to saturation magnetization of the soft magnetic film is generated in the narrow space of the gap even when low ex-

ternal field is applied which leads to enhancement in MR ratio at lower fields. We investigate the effect of soft magnetic inserted in the CPP granular films. Permalloy (Py) is one of most widely researched soft magnet and Py with composition $Ni_{80}Fe_{20}$was used in this study.

6.1 Effect of Py on magnetic field: Finite Element Method Magnetics simulation

The insertion of Py layer in the granular film changes the magnetic flux characteristics of the system and it is essential to understand these changes. For this purpose 2D Finite Element Method Magnetics (FEMM) simulation [117] simulations modeling is made use of to understand the effect of soft magnet on the variation in magnetic flux. It is known from the GIG experiment that the major flux change is introduced by the soft magnet and the granular film does not play such a major role in changing the flux [7]. For the modeling, the constant field of 0.36 T is generated using two NdFeB permanent magnets. Since the experimental MR ratio is measured experimentally at maximum field 0.4 T, the simulation serves as a good basis for comparison. In order to verify the application of the 2D FEMM model, first the simulation is done for the well known CIP based GIG structure and then the other configurations related to the proposed structure are evaluated.

6.1.1 CIP GIG structure

The CIP based GIG structure was fabricated by Kobayashi et al. and it was identified that by using $Fe_{66}Ni_{34}$ as the soft magnetic layer for $Co_{39}Y_{14}O_{47}$ granular films enhanced the MR by 250 times compared to films without the soft magnet [7]. This increment was due to the enhancement in stray flux between the electrodes due to

the soft magnetic layer. The schematic for this configuration is shown in fig. 6.1a.

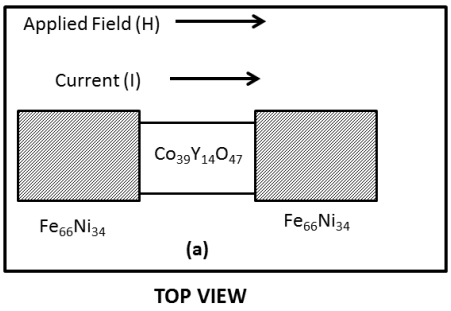

Figure 6.1: Schematic of GIG structure (Top view) : In plane field parallel to current [7]

As discussed earlier, the CIP based GIG structure has been one of the most researched structure for flux improvement and it can be verified from the FEMM simulation shown in fig. 6.2. The simulation is generated by employing two 300(length) x 200(width) nm Py electrode. The applied field is ~0.36T while the field within the Py layer is of the order of 0.9T and in between the two Py electrode is around 0.65T indicating the fact that the field is enhanced. This verifies the observation of Kobayashi et al. [7]

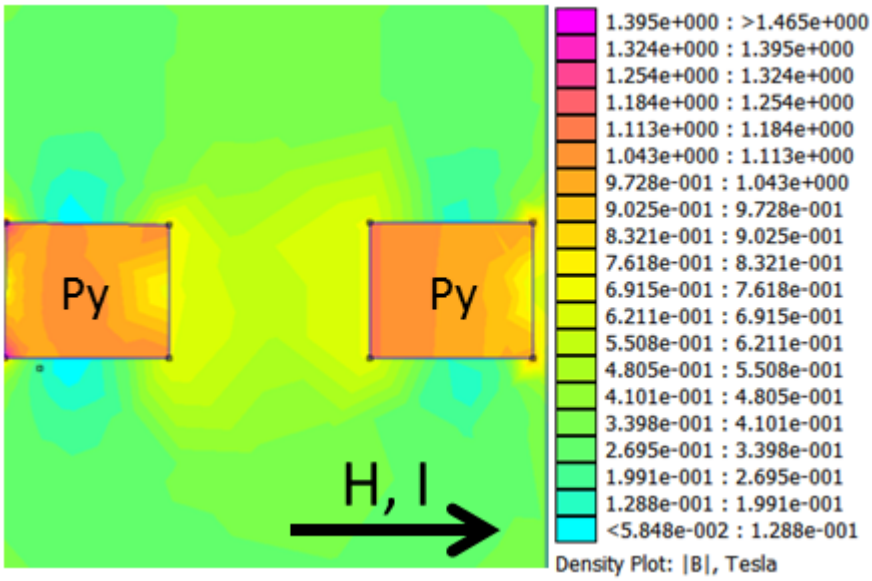

Figure 6.2: FEMM simulation of CIP GIG structure

.

Similarly for CPP structures, we first study the effect of Py films being parallel and perpendicular to the field.

6.1.2 Single Py film parallel and perpendicular to field

The FEMM simulation is implemented for single layer Py with the field application being parallel and perpendicular to the film as seen in fig. 6.3a. The thickness of the Py layer is 20 nm (thickness) x 500 nm (width). It can be seen from fig. 6.3a that when the Py layer is parallel to the field, it draws the flux and there is flux enhancement in the Py layer (~1.4 T) while closer to the edges the field rises to ~0.7 T . The flux in the the central region around the single electrodes reduces to ~0.25 T. For the other configuration where the film plane is perpendicular to the applied field (fig. 6.3b) there seems to be no enhancement and this matches with the observation by Kobayashi et al. [7] for their GIG device. So the field enhancement is achieved only when the field is applied in-plane (Py layer parallel to the applied field).

6.1.3 Thickness limitation of Py layer based on fabrication constraints

Although the fabrication of the CPP device has already been done in the last chapter, it is discussed again for easier reference. Figure 6.4 shows the four photolithography steps involved in the fabrication of CPP devices. Step 1 shows the deposition of the Cr/Au bottom electrode which is approximately 25-30 nm in thickness. Then in the second step, the active device layer is deposited on the electrode followed by oxide insulation in step 3. This oxide layer helps to electrically isolate the top and bottom layer. The active device layer area is ~ 10 μm x 10 μm

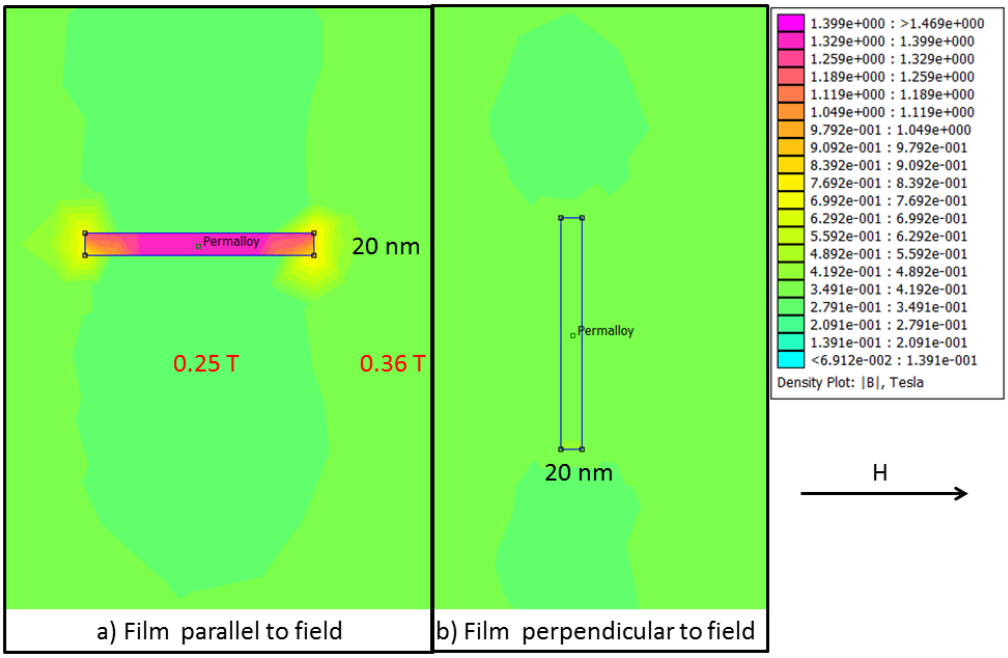

Figure 6.3: FEMM simulation of Py film (a) parallel to applied field (b) perpendicular to applied field

and at that scale the third step namely liftoff of the oxide layer poses a problem. The central hole covered by the resist cannot lift for high thickness of the films. Therefore, thinner oxide layer is preferred which in turn affects the maximum active layer thickness. It was found that up to a thickness 100nm of oxide layer, there are no lift off issues. Since the approximate thickness of the bottom electrode is 25 nm, the thickness of the active device layer can be unto a maximum thickness of ~75 nm. In the previous chapter, it was found that 20 bi-layers of Co and HfO_2 gave the best CPP MR with approximate thickness of Co and HfO_2 being 1 nm. So the effective maximum thickness of the soft magnet used for the experiment can only be around ~35 nm.

The fabrication of CPP based structure with two electrodes is shown in fig. 6.5a. The electrodes are Py with granular films in between. However, due to the restriction on thickness of Py as explained above, a modification is proposed wherein the soft magnetic layer (Py) is inserted between the magnetic film(fig.

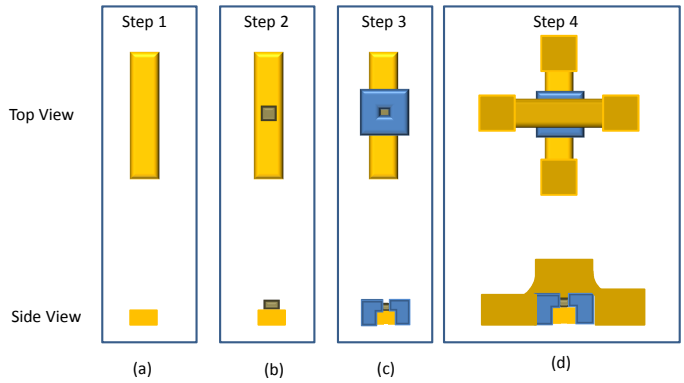

Figure 6.4: Schematic of CPP fabrication based on Py insert

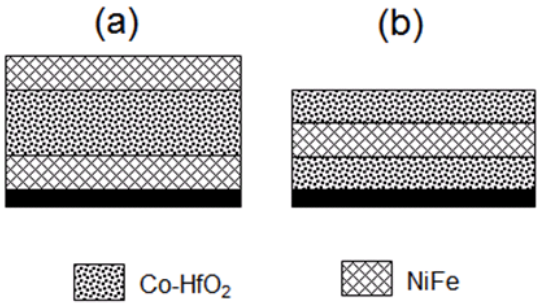

Figure 6.5: Schematic of (a) CPP structure with two Py electrode (b) Proposed modification with single Py layer

6.5b). To understand the variation in magnetic flux because of the insertion, FEMM simulations have been implemented for both these structures.

Fig.6.6 shows the FEMM simulation for two electrode system and single layer Py system.

Two Py electrode: Figs.6.6 a & b represent the two electrode system where the granular film is supposed to be in between the two electrodes as shown in fig. 6.5a. The dimensions of the Py electrode are 20 nm (thickness) x 200 nm (length), while the separation between the electrodes (equal to thickness of the granular film) is 20 nm and 40 nm for the structures in figs.6.6 a and b respectively. The purpose of this simulation is understand the change in magnetic flux when the thickness of the granular film changes. It should be noted that the Py layer shows a maximum

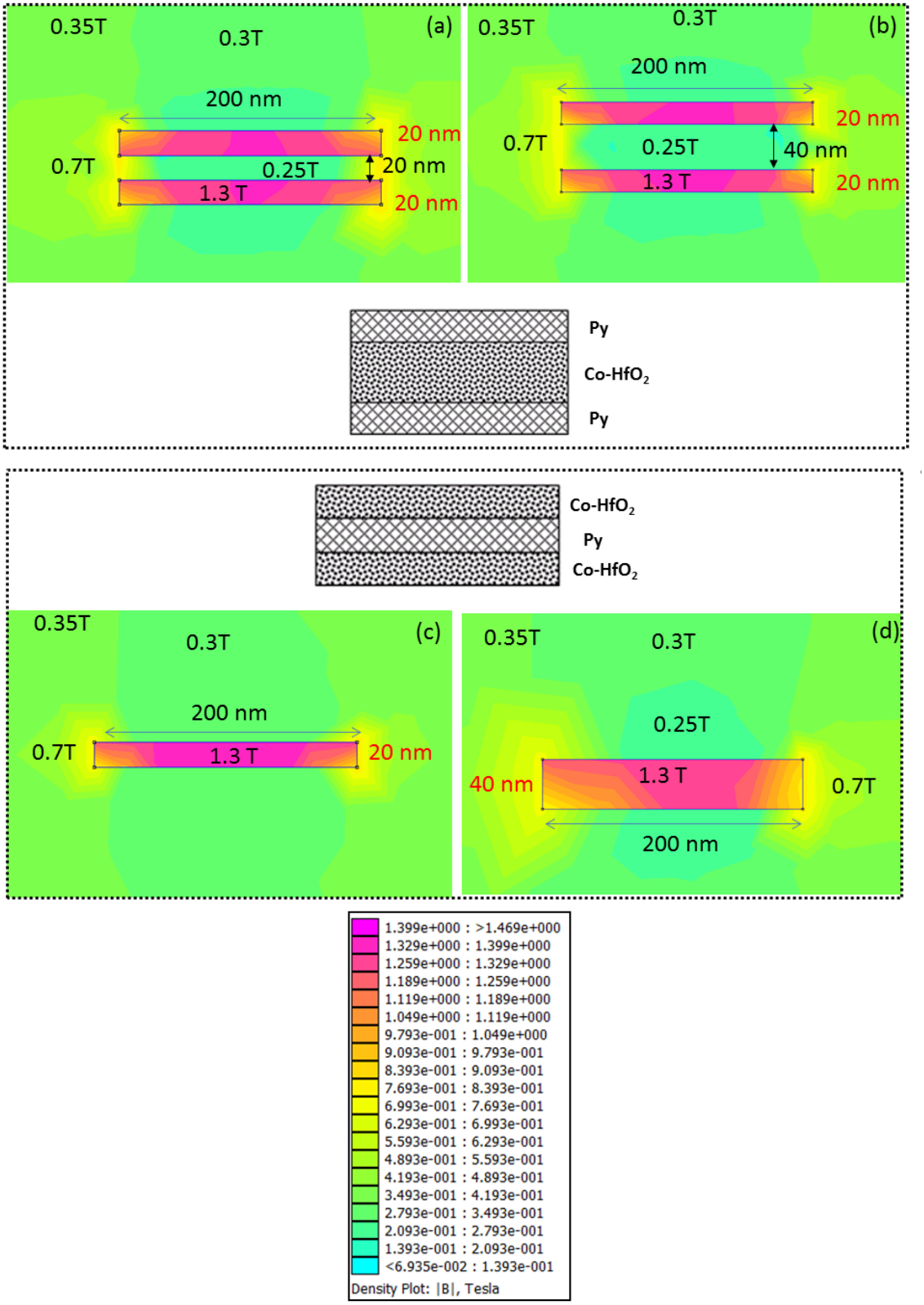

Figure 6.6: FEMM simulation of Py film (in-plane configuration) for two electrodes vs. single Py layer a) two electrodes of length 200 nm and thickness 20 nm separated by 20 nm b) two electrodes of length 200 nm and thickness 20 nm separated by 40 nmc) single electrode of length 200 nm and thickness 20 nm d) Single electrode of length 200 nm and thickness 40 nm

field of 1.4 T at the center of the Py film for both the cases. In the two electrode system in fig. 6.6a magnetic flux as high as 0.7 T (yellow colour) is found at the edges of the configuration. The area of influence is around 20 nm from the edges to the center of the film. However the field drops to 0.25 T in most of the central region between the electrodes. As the separation between the two electrodes increases to 40 nm (fig. 6.6b) the influence of edge field (0.7 T) in terms of area decreases even further and the majority of the region between the two electrode has 0.25 T. So in this configuration the field enhancement effect is reduced as the thickness of the granular film increases.

Single Py layer: Fig.6.6c & d represent the single Py layer inserted in between the granular film as shown in fig. 6.5b. The dimension for the Py layer in figs.6.6c and d are 20 nm (thickness) x 200 nm (length) and 40 nm (thickness) x 200 nm (length) respectively. For both the cases, the Py layer shows a maximum field of 1.4 T at the center of the Py film. The Py layer in fig. 6.6c. shows an increase in magnetic flux at the corners similar to the two electrode system (0.7 T for length of 20 nm from the edges to the center), however the flux in the rest of the region surrounding the Py layer has not fallen below 0.3 T. As the thickness of the Py insert is increased to 40 nm (fig. 6.6d), larger area from the edges to center of the Py layer have 0.7 T field (~40 nm). The central area under the Py electrode has only 0.25 T, which however is a very small area. Thus thicker films single Py layer films seems to have better field enhancement and this combined with the fabrication limitation leads us to focus on the modified structures shown in fig. 6.5b

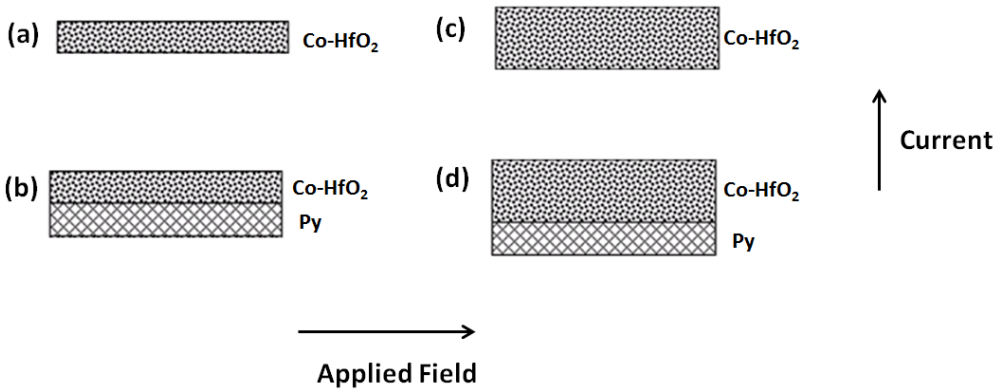

Figure 6.7: Preliminary configuration based on Py insert (a) G (b) G+Py (c) 2G (d) 2G +Py

6.2 Preliminary Experiments : CPP with single Py layer

In order to study the MR response of the systems with inserted with Py layer, we first studied the effect of Py insertion on G and 2G with the Py being one of the electrodes (i.e without the insertion). The experiment was done to understand whether G or 2G was more optimum to be used along with the Py insert. The following structures were fabricated and studied(fig. 6.7).

1. G
2. G+Py
3. 2G
4. 2G+Py

where thickness of the Py layer is chosen to be 5,10 and 15 nm.

fig. 6.8 shows the MR curves for G, G+Py(5 nm), 2G and 2G+Py(5 nm). It can be seen that the MR ratio is the highest for 2G as seen in the previous chapter. However the addition of the Py insert the 2G structure does not seem to show any

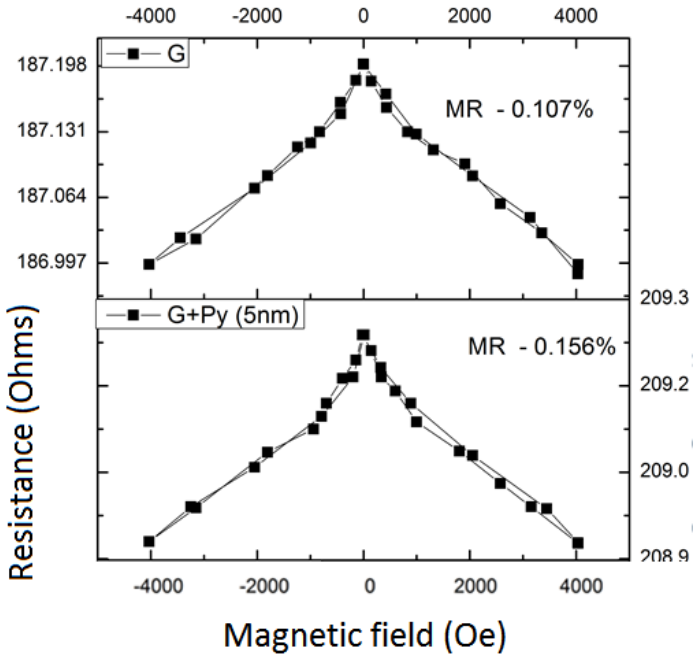

(a)

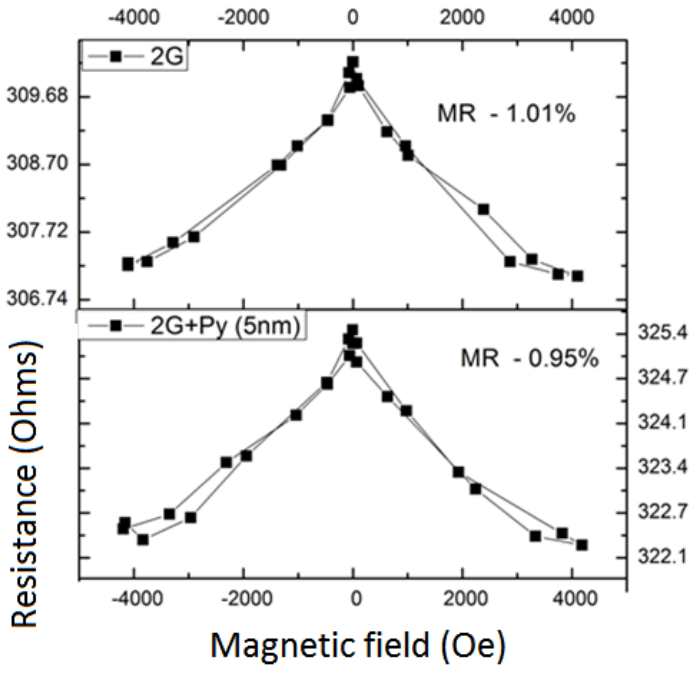

(b)

Figure 6.8: MR curves of granular films a) G and G+Py (5nm) b) 2G and 2G+Py (5nm)

enhancement in MR. Whereas for structures G, the insertion of Py layer (5 nm) increases the MR ratio rises from 0.107% to 0.156%. This is a change of about 50 % in terms of MR ratio at a field of 4 kOe, which is not enough to saturate the granular film. This can be explained based on stray flux enhancement discussed in the previous section. It must be noted that the flux change is significantly higher at the edge of the structure than at the center. Since 2G is twice as thick as G, the flux enhancement is not effective over the entire thickness of 2G resulting in no MR improvement compared to sample G. This was also true for the 10 nm and 15 nm thickness of Py insert suggesting that G is more suitable for the experiment.

Subsequently, the Py layer is inserted at the center of the granular film. Therefore a comparison is drawn for G, G+Py (5 nm) and G+Py (5 nm)+G and the MR response is shown in fig. 6.9a. The structure G+Py has a higher resistance than G which is expected because of the presence of the Py layer. There is also an increase in MR ratio which has been explained earlier due to the enhancement in flux. The G+Py+G structure has higher resistance compared to the aforementioned structures and it can be seen that it has highest MR ratio among the three, indicating the fact that the Py layer help improves the magnetic flux at the edges and enhances both the top and bottom granular film MR. The normalized resistance curves for the three structures are shown in fig. 6.9b. It can be seen that MR curves for G+Py and G+Py+G are steeper than for G, indicating the fact the Py insert improves the response of the structures in addition to improving the overall MR.

Based on these preliminary results, a series of samples are studied where the Py layer is stacked between two granular films of equal thickness (same as G). The Py inserted granular film has the following structure : $[\mathrm{Co}(0.8\ \mathrm{nm}) + \mathrm{HfO_2}(1.1\ \mathrm{nm})]_{10}$ +Py(n)+$[\mathrm{Co}(0.8\ \mathrm{nm}) + \mathrm{HfO_2}(1.1\ \mathrm{nm})]_{10}$ where n takes the value 1.5 nm, 3 nm, 5 nm, 10 nm, 15 nm and 35 nm and the samples are referred to as $\mathrm{N}_{1.5nm}$, N_{3nm} and

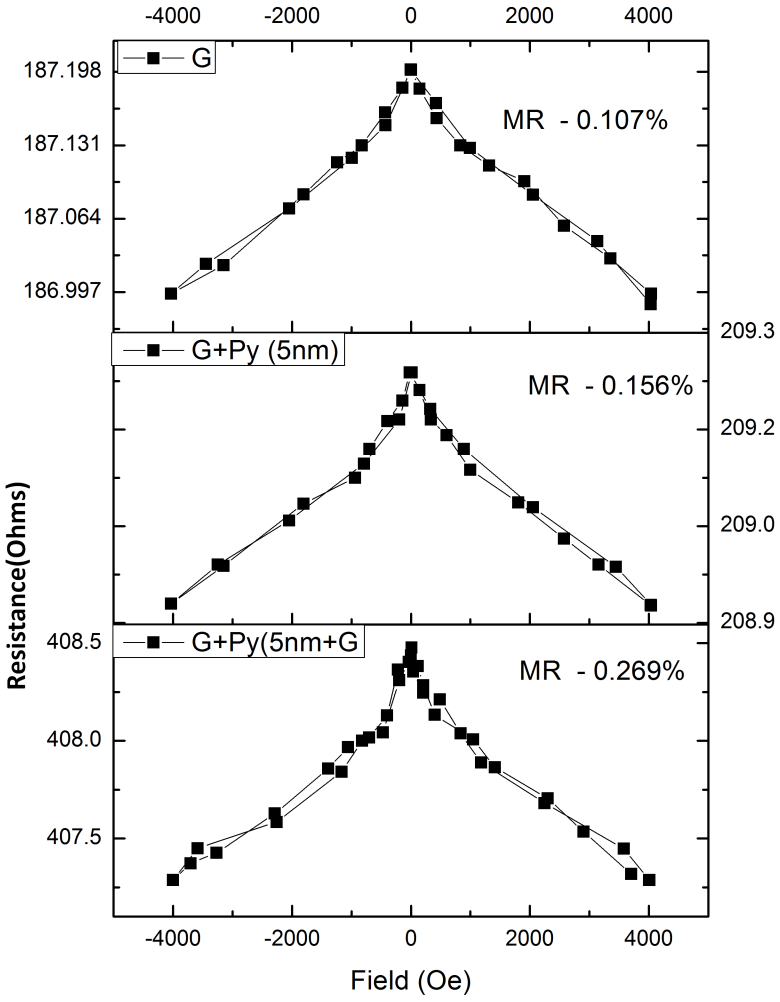

(a)

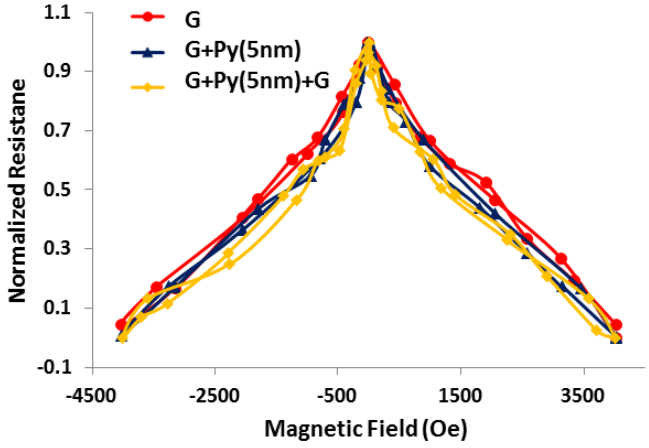

(b)

Figure 6.9: MR curves of Py insert of 5 nm thickness (a) MR for G, G+Py and G+Py+G (b) Normalized resistance for three structures showing improvement in MR response with Py insert

so on. This is analogous to the structures investigated in chapter 4, wherein the HfO_2 is used as the insert.

6.3 Rutherford back Scattering Experiment

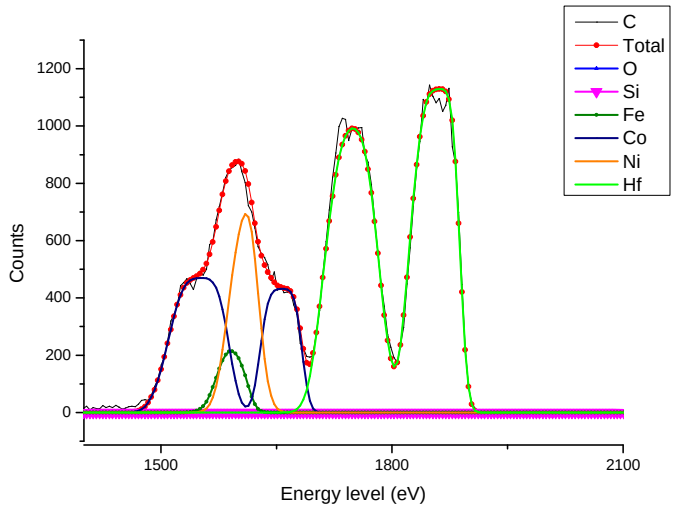

Figure 6.10: RBS of sample N_{35} showing the contribution of various elements. It is difficult to discern the ideal peaks of Co, Fe and Ni because of their close atomic weights

Fig.6.10 shows RBS for sample N_{35nm}. Although the energy level(or channels) for detection for the various elements are different, the atomic weights of Co (Z=27), Ni (Z=28) and Fe (Z=26) are very close to each other and result in a joint peak as seen in the fig. 6.10. Therefore, we can make an assumption that the Py film sputtered on the film has the same stochiometry as the target used ($Ni_{80}Fe_{20}$) and then fit that peaks. On the other hand, the Hf peak is independent of the above assumption and more reliable for analysis of the structure. It shows that the top and bottom layer are well separated from each other by the central layer. The approximate Co volume fraction obtained using this data is found to be 35.5 %.

6.4 Roughness

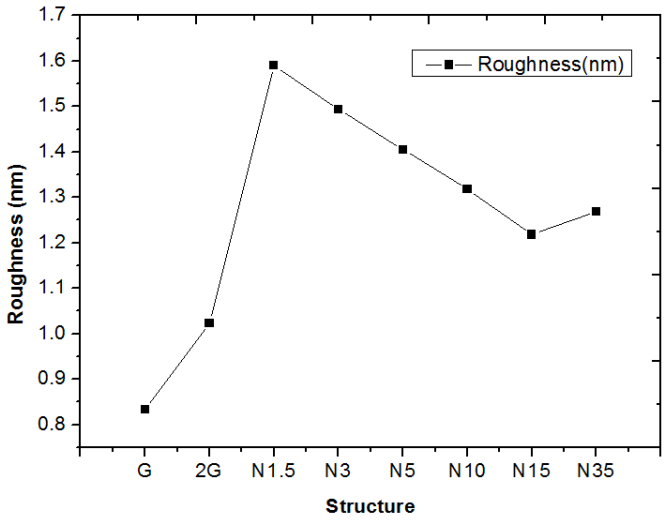

Figure 6.11: RMS roughness trend for the samples

The surface roughness of the films are obtained for all the samples and the trend is presented in fig. 6.11. Insertion of 1.5 nm of Py in 2G causes the roughness to increase from 1.023 nm to 1.591 nm. At such thickness the Py film is assumed to be highly discontinuous and possibly leads to the formation of Py grains in HfO_2. Then as thickness of the inserted Py layer increases, the roughness decreases up to 15 nm of Py insert (1.218 nm) and then increases slightly for Py insert of thickness 35 nm (1.289 nm). Usually on smooth film surfaces discontinuous films cause increase in roughness which is the case for 1.5 nm insert. As the thickness is increased, the Py atoms start to diffuse and fill up the gaps between the films faster than on top of the films. As a result the roughness starts to decrease which is what is observed in our case [118].

It should be noted that the roughness trend obtained by varying Py thickness is same as that obtained using HfO_2. Therefore it can be deduced that the nature of insert will also have similar trend i.e $N_{1.5nm}$ will be discontinuous while N_{3nm} is less discontinuous. For thickness of insert greater than 5 nm the insert is continuous in

nature. Therefore the grain size trend is assumed to follow that of the HfO_2 insert, such that the inserts with Py thickness greater than 5nm will have larger grain size compared to the rest of the samples.

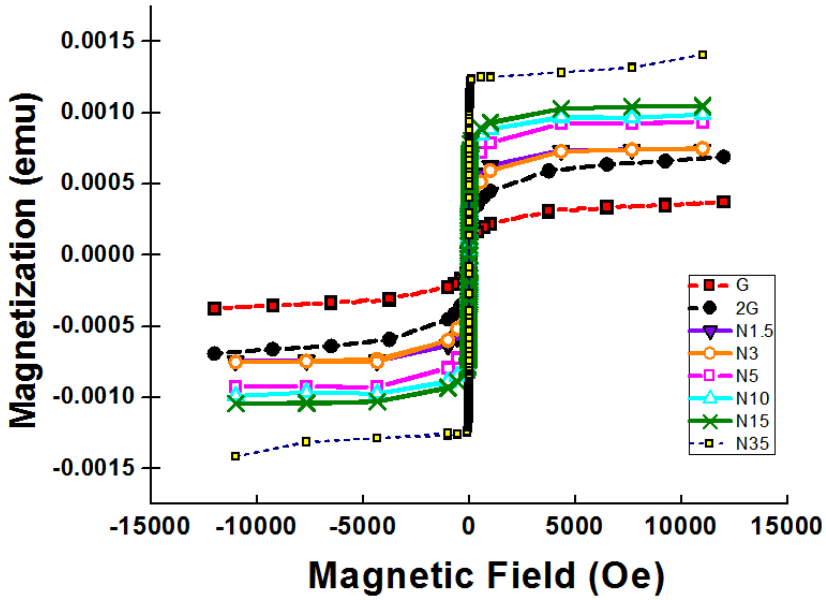

(a)

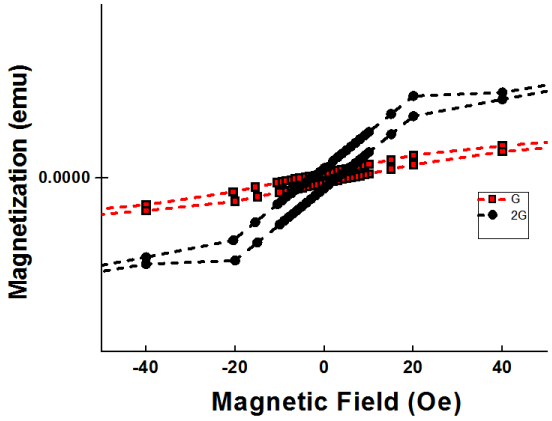

(b) G and 2G

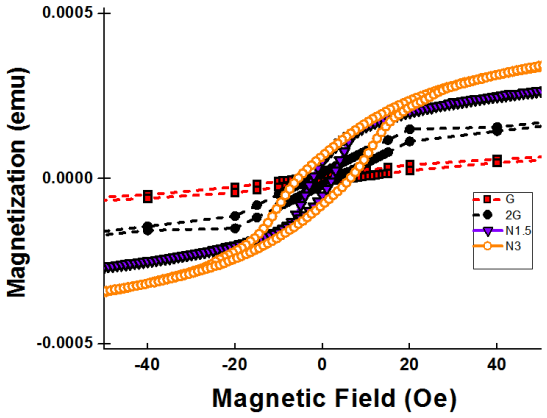

(c) G, 2G, N1.5 and N3

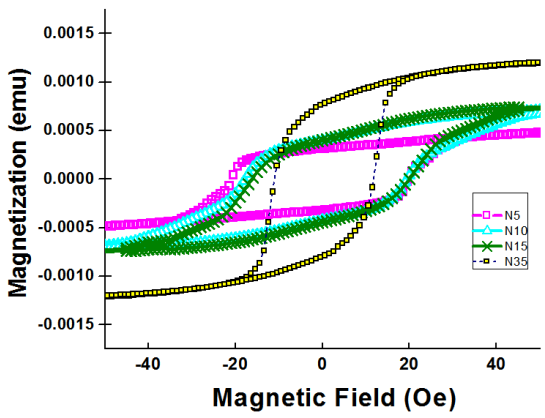

(d) N5-N35

Figure 6.12: M-H loop (a) overall (b) Zoom in view G and 2G (c) Zoom in view for G, 2G, $N_{1.5}$, N_3 and N3 (d) Zoom in view for N_5, N_{10}, N_{15}, and N_{35}

6.5 M-H loop measurement

Figure. 6.12a shows the M-H loops for all the curves and it can be seen that the sample moment increases for samples with higher Py layer thickness. The contribution of magnetization comes from both the Py layer and Co grains in the films. Hence even though the Py has saturated at 12 kOe, the M-H loops slightly curve upwards which is due to the contribution from the granular film.

The granular films ideally should have zero coercivity but in reality they have some coercivity and so does Py, depending on its thickness. The difference in the switching fields of the granular film and Py is expected to be reflected in the M-H loops as well as the MR curves for the samples. Figure. 6.12b shows the zoom in view of the M-H loops between -50 and 50 Oe for samples G and 2G which do not have any Py layer. It can be seen that the samples have a coercivity ~ 5 Oe. Figure. 6.12 c & d shows the zoom in view for samples i) G, 2G, $N_{1.5nm}$, N_{3nm} and ii) N_{5nm}, N_{10nm}, N_{15nm}, N_{35nm} respectively. The effect of change in coercivity of Co and Py is visible as a kink in samples N_{5nm} to N_{15nm}, but not in sample N_{35}. This is because there is a decrease in Py coercivity for the latter and this value being closer to that of Co there is no visible kink.

6.6 Resistance and MR curves

Figure. 6.13 show the MR curves for the samples obtained at room temperature. It can be seen that the MR ratio increases from $N_{1.5nm}$ - N_{35nm}. The zoom in pic of the MR curves is shown in fig. 6.14 and it can be seen that the MR curves for N_5 - N_{15} show kink in approximately the same location as seen in the M-H loop (in figs. 6.12 b, c & d). Fig.6.15 shows the MR ratio and resistance trend for the samples. It can be seen that the resistance increases all the way from G to N_{35nm}. On the

other hand the MR initially drops with the insertion of Py layer and then rises with increasing Py thickness. Figure. 6.13b shows the normalized MR response for samples N_{5nm}- N_{35nm}. It can be seen that the MR response becomes steeper with increasing Py thickness. This is attributed to the flux enhancement of the Py layer which improves with increasing Py thickness.

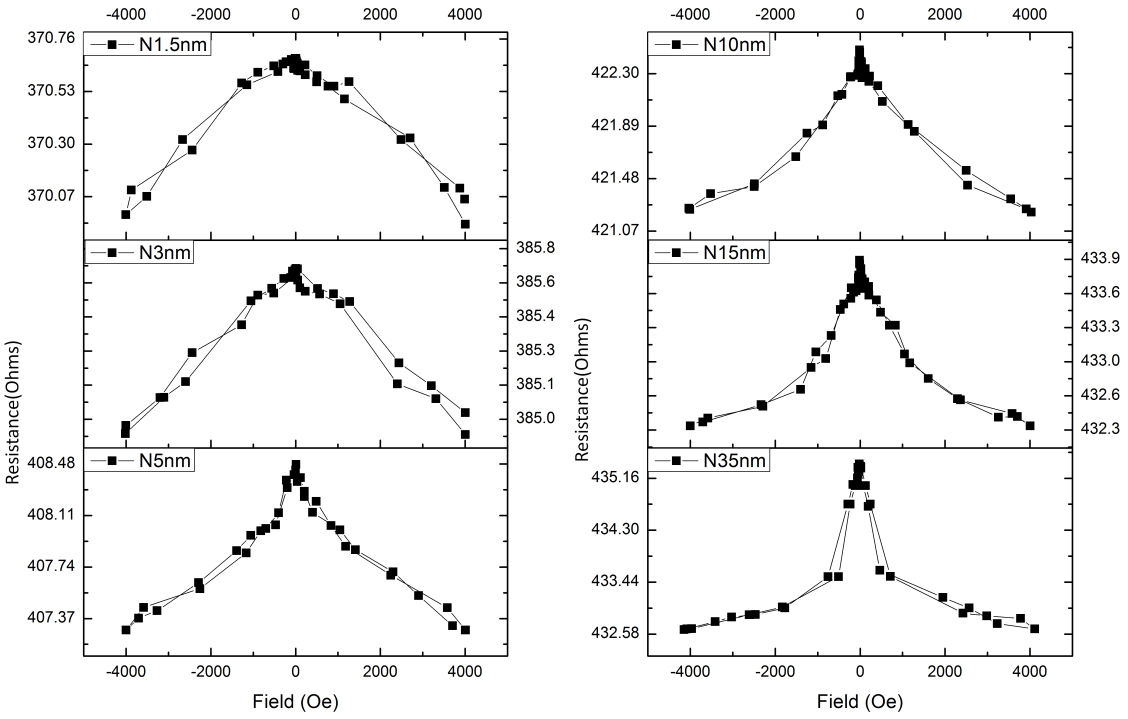

(a)

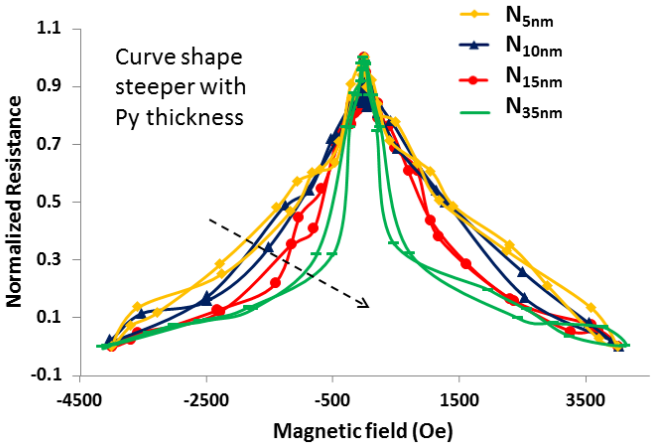

(b)

Figure 6.13: MR curves (a) for the structures with thickness of Py between 1.5nm to 35 nm (b) Normalized resistance graph from N_{5nm}- N_{35nm} showing the improved MR response with increasing Py thickness

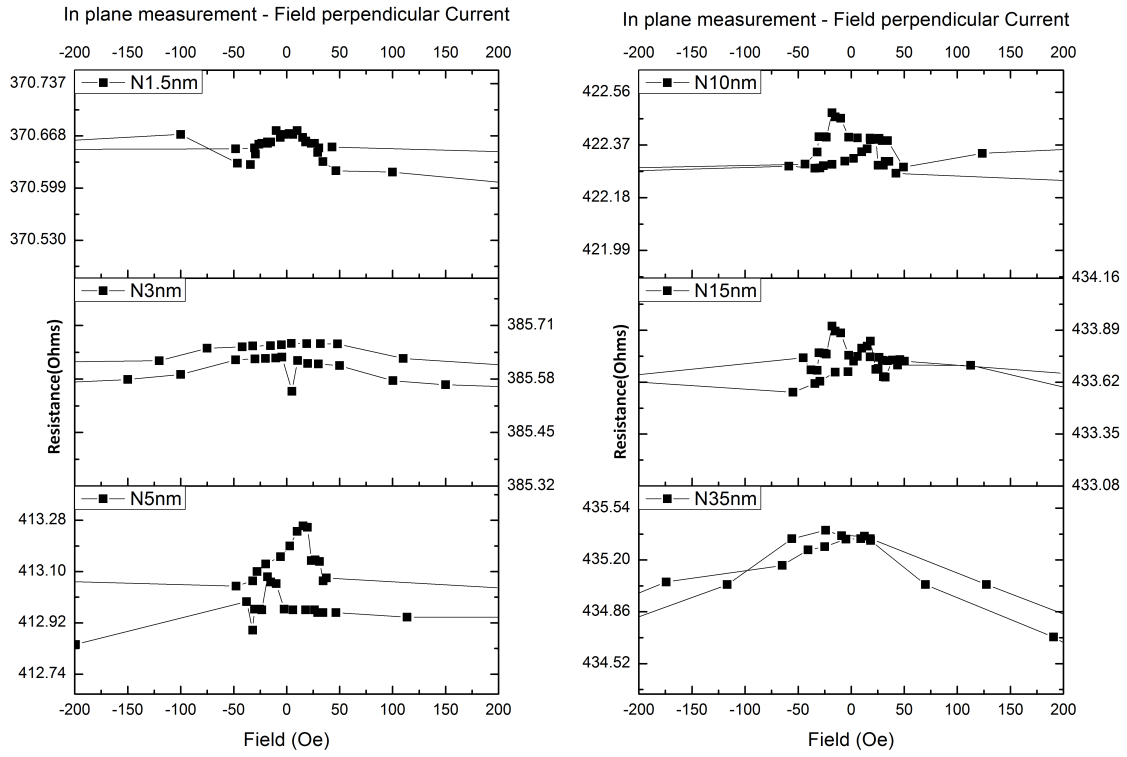

Figure 6.14: Zoom in for the in plane MR measurement for samples $N_{1.5nm}$- N_{35nm}

Resistance: As seen in fig. 6.15, there is a jump in resistance from G to 2G due to the increase in the effective tunneling length across the granular film (discussed in chapter 4). As Py of 1.5 nm is inserted in the granular film, the resistance increases from 2G to $N_{1.5nm}$ due to the additional Py layer. As the thickness of the Py further increases, the resistance also increases monotonically because of increase in Py metallic resistance.

MR: The grain sizes in structures with Py insert greater than 5 nm have larger grains compared to the other structures. Therefore the MR in these structure is due to a) tunneling through larger Co grains in the top layer b) tunneling in the bottom layer c) tunneling between larger Co grains and the Py layer (top layer) d) and tunneling between the Py layer the Co grains (bottom layer). Since the bottom layer are same for these structures, the enhancement in MR seem with increasing

Py thickness is due to larger Co grains in the top layer as well improved tunneling between Py layer and Co grains .

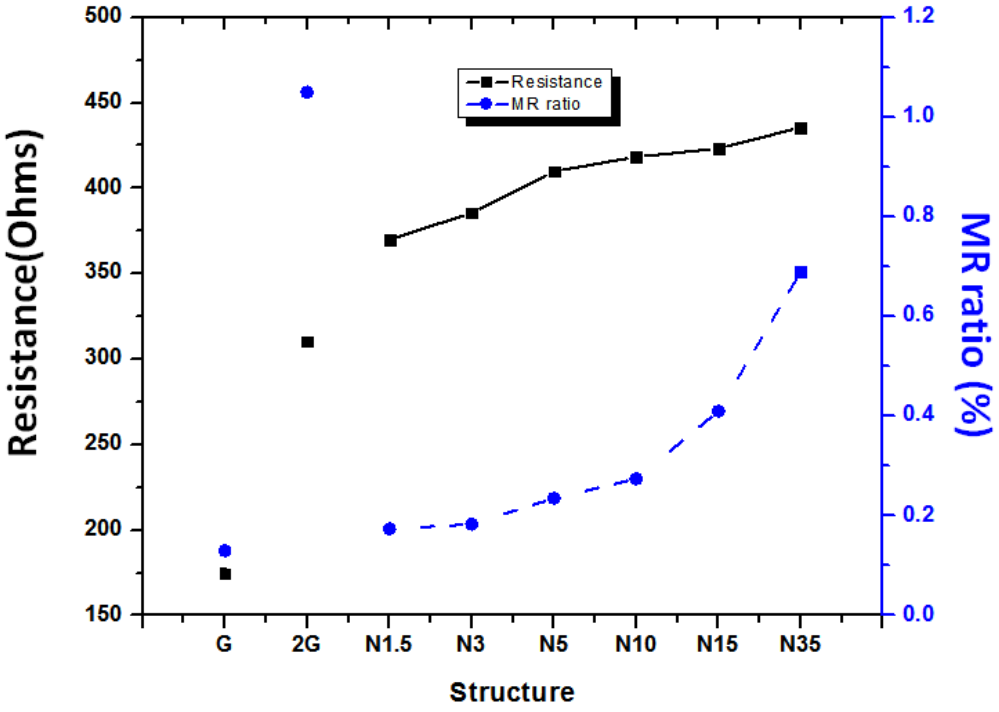

Figure 6.15: Variation of resistance and MR with Py thickness. Both R and MR increase with increasing Py thickness

Compared to 2G, the MR ratio drops with inserted Py layer of 1.5 nm. From the roughness of the insert, it can be deduced that the 1.5 nm Py insert is highly discontinuous in nature. Therefore they form a thin Py-HfO_2 granular film at the center of the film. Therefore if the Py grains behaviour is similar to Co , then the MR ratio should be similar to that of 2G. However the Py grains have different polarization compared to Co and hence there is reduction n MR because of tunneling between Co and Py grains. As the thickness of the Py layer is increased to 3 nm, the film becomes more continuous and it can help in flux enhancement. In general, increase in MR with increasing Py thickness (greater than 3 nm) is expected based on the FEMM simulations and is explained in fig. 6.16. In the absence of the Py

layer, the magnetic field is uniform. When the Py film is introduced, it bends the flux lines and makes them pass through the Py layer (fig. 6.16 b). As the thickness is further increased, this effect becomes more pronounced (fig. 6.16 c). It should be noticed from the FEMM simulations (figs. 6.6 c & d.) that the Co grains closer to the edges of the Py layer experience an enhanced flux(~ 0.7 T) and this area of influence of the enhanced flux increases with thickness of the Py film. So the electrons tunneling through this region will have reduced high field effect tunneling because of the enhanced magnetic field and hence the MR ratio improves.

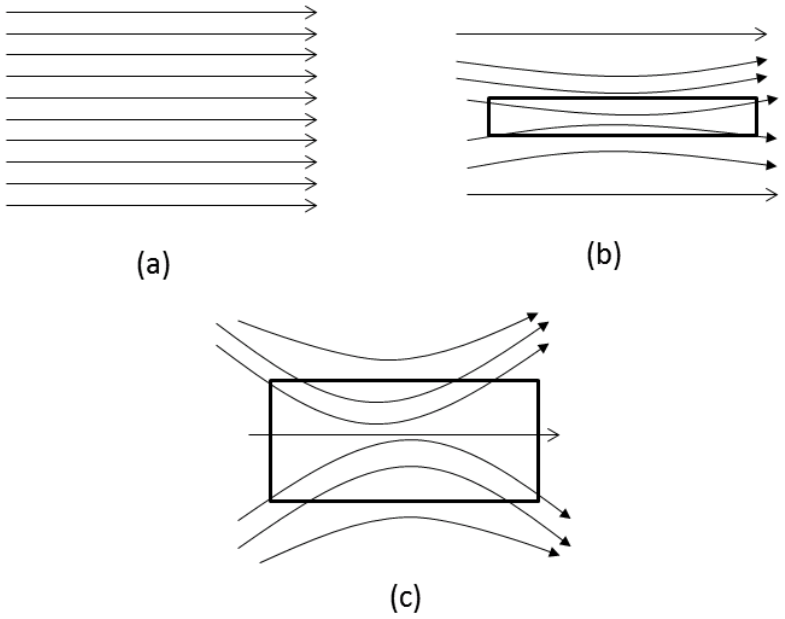

Figure 6.16: Model of magnetic field based on FEMM simulation discussed earlier a) Absence of Py layer b) Presence of thin Py layer c) Presence of thicker Py layer

Structure 2G has the same total thickness of granular film as the inserted structures. It should be noted that MR field response became steeper with increasing Py thickness (fig. 6.13). Therefore we have compared the MR curves for N_{35nm} and 2G to understand the low field response. The MR ratio curves are calculated as $MR(H) = 1 - \frac{R(H)}{R(H=0)}$, where H is the applied field and R the resistance and is shown in fig. 6.17. It can be observed that the structure with Py insert of thickness

35 nm has a steeper rise in MR response compared to sample 2G in the field range of 0 - 700 Oe. Therefore N_{35nm} is more sensitive to the magnetic fields between 0 - 700 Oe compared to 2G and is mainly due to the flux enhancement by the Py layer at such fields.

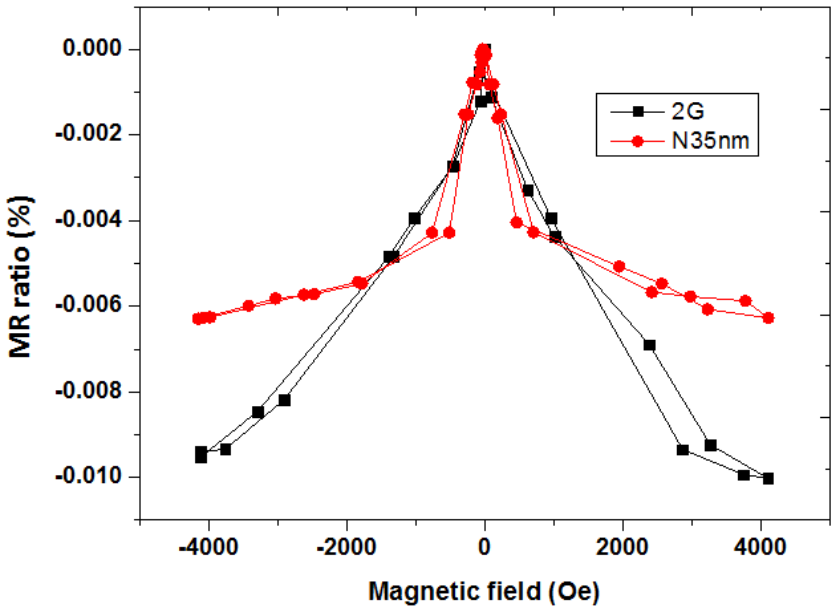

Figure 6.17: The MR ratio curve for sample 2G vs. N35

Overall, the MR trend increases with Py thickness as seen from fig. 6.15a . The maximum thickness that we were able to fabricate was 35 nm because of fabrication limitation explained in section 6.1.3. It is expected that as the thickness of Py layer is increased beyond 35 nm, the MR will further improve because of the stray edge field enhancement explained in figs. 6.6 c & d. Figure. 6.18 shows the flux distribution for 100 nm thick Py film. It can be seen that the flux at the center of the Py film has reduced to 0.75 T (compared to 1.3 T in figs. 6.6c & d) . Even the field at the edges of the film influencing the granular film has reduced to 0.6 T and it decreases from edge to center of the film. However the area of field enhancement from the edge to center is higher for this film (~ 90 nm). It can also be noticed that the enhancement of the flux along the vertical direction has also increased. Hence

thicker granular films can also be used for field enhancement. However there would be a limit to this effect and beyond a particular thickness of Py the MR would start to drop as thicker Py layer will more efficiently channel the flux through itself and the fringe flux enhancement benefits at the edges will reduce as seen from the FEMM simulation.

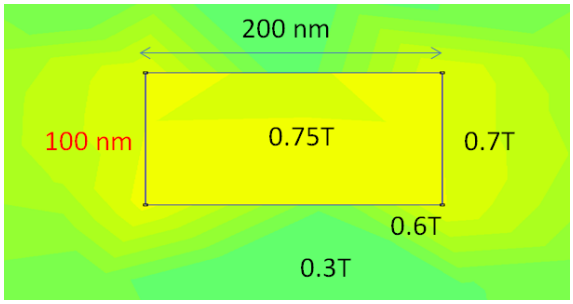

Figure 6.18: FEMM modeling showing flux enhancement for 100 nm thick Py layer

6.6.1 Comparison with Py insert with HfO_2 insert

The inserted Py layer induces roughness change similar to the case of HfO_2 and it becomes important to understand the variation in MR for the two cases. The MR ratio comparison for Py and HfO_2 insert are shown in fig. 6.15b. The MR ratio for the HfO_2 insert drops with increasing insert thickness. This is majorly due to the choice of paths being influenced by the central tunneling barrier, grain size in the top granular film layer and high electric field induced tunneling. This has been discussed in depth the previous chapter. For the Py insert the MR ratio increases with Py thickness and it was found that this effect was induced by the fringe flux enhancement of the Py layer. This effect increases with increasing Py thickness. This shows that effect of the magnetic field is the case of Py is more significant than the grain size increase expected for films with insert thickness greater than 5 nm. The two graphs intersect at a thickness of 13 nm and at this thickness of Py layer, the flux enhancement has started to show improvement by reducing the high-field

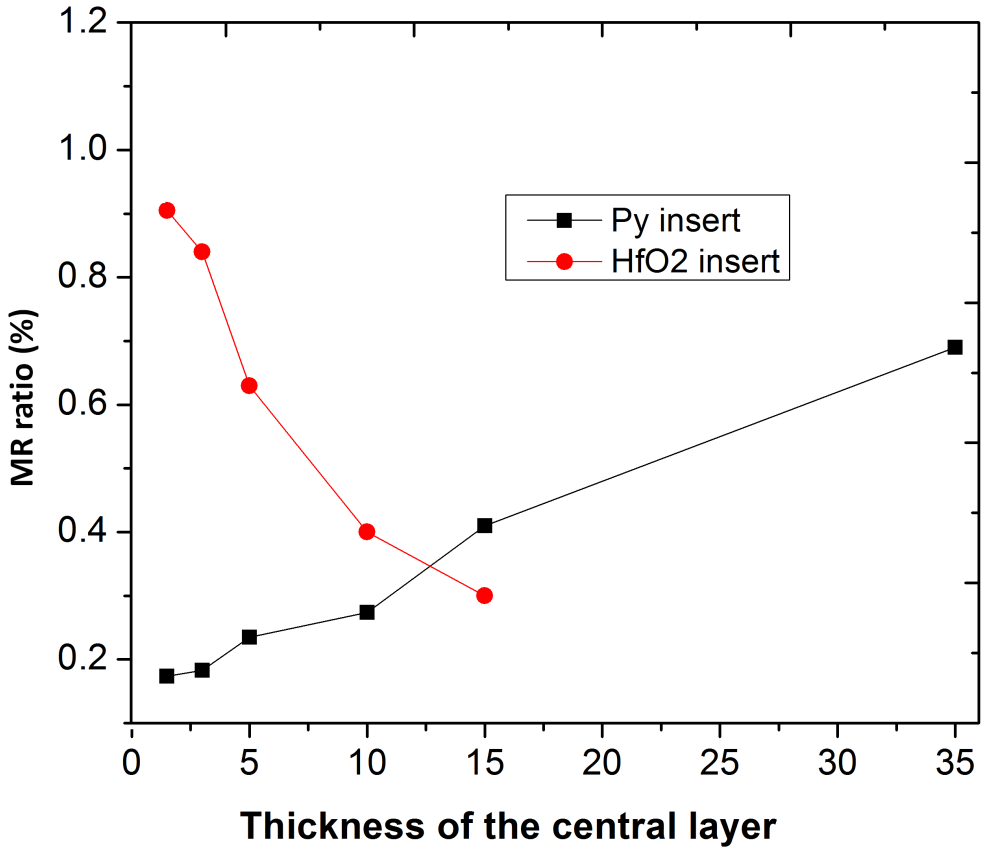

Figure 6.19: Comparison of MR variation for Py and HfO_2insert with varying thickness

induced tunneling. This flux enhancement increases as the thickness of the Py layer is further increased.

6.7 Summary

Kobayashi et al. proposed the GIG structure to improve the low field MR response of $Co_{39}Y_{14}O_{47}$ granular films and they observed a improvement in MR by 250 times using $Fe_{66}Ni_{34}$ soft magnetic layer [7]. The motivation for the CPP based Py inserted structures discussed in this chapter is to help improve the MR response in these structures by reducing the high field induced tunneling which was observed in the

HfO_2 inserted structures. The Py layer was able to generate fringe magnetic field which helped in MR improvement. The thickness of the Py layer was varied and it was noticed that the MR increased with increasing Py layer and this was attributed to the flux enhancement at the edges of the Py layer. Compared to the HfO_2 inserted structures, it was observed that Py thickness of greater than 13 nm was required to reduce the high field induced tunneling an and hence improve MR . Py layer of thickness 35 nm was compared with 2G and it was found to have a improved low field response than 2G in the field range of 0-700 Oe.

Chapter 7

Conclusion and Future Work

In this thesis, the fabrication and characterization of devices based on Co-HfO_2 granular films is reported. The granular films were fabricated using sequential sputtering. The choice of film is justified because of reduction in Co-oxides due to higher bond energy of the Hf-O bond. We first analyzed the properties of the bulk structures G and 2G consisting of 10 and 20 bilayers each of Co and HfO_2 respectively. Sample G was found to be optimum in terms of CIP MR as opposed to sample 2G and together they formed the basis for comparison in this thesis. After understanding the bulk properties, the microdevice properties were analyzed for these films and it was found that the performance of microdevices was better in terms of MR compared to the bulk, at the same time showing a higher resistance compared to bulk films.

The main contribution of this work are summarized below.

1. By controlling the roughness of the insert layer, different types of transport and properties were obtained for the granular films. This was achieved by inserting HfO_2 layer in between granular films and varying the insert thickness from 1.5 nm to 15 nm. The experiment was designed such that the top and bottom films formed were equal in thickness (and number of bilayers) to sample G,

which gave the optimum CIP MR ratio. For thickness of inserted oxide less than 3 nm, it was found to be discontinuous and for films greater than 5 nm it was found to be continuous. The discontinuous films affected the grain size in such a way that, these samples with insert thickness of 1.5 nm and 3 nm showed trends towards Coulomb Blockade. The former was the only sample which showed a visible Coulomb Blockade and higher order tunneling characteristic at 10.2K. Due to higher order tunneling, the MR ratio of the sample jumped from 1.7 % at 20K to 3.84 % at 10.2 K.

2. The continuous oxide films fabricated using the above method induced formation of larger grains in the top granular film layer as compared to the bottom layer and the major conduction was along this top granular film layer as it had a lower resistance compared to the bottom layer. Compared to sample 2G, structures with insert thickness between 5nm and 15 nm showed improved MR ratio. However the structures with 10 nm and 15 nm insert showed lower MR ratio compared to sample G because of the presence of leakage conductivity, which reduced the effective MR ratio. The leakage conductivity was observed to increase with increasing inserted oxide thickness.

3. A simulation model based on Monte Carlo method was implemented to find the CIP transport properties of the proposed structure. The model made use of the experimental M-H loop to find the grain size distribution and generated a grain size matrix with random location in order to simulate the granular film. Then the MR was calculated based on the resistive network mode. The simulator gave comparable results for most structures except for the 10 nm and 15 nm insert. The simulated MR was higher than the experimental MR for these structures and this can be attributed to the fact that experimentally these films are affected by leakage conductivity.

4. CPP structures were fabricated using the proposed structure to understand the difference in transport properties between CIP and CPP devices. The CIP conduction for proposed structure is different from CPP conduction because CIP conduction is through the top layer whereas the conduction for CPP devices is through both the top and bottom layers. However, the number of grains taking part in the conduction for both the CIP and CPP devices are different and the effective conduction length(through the granular film) for CIP devices is ~4 μm whereas it is maximum of ~40 nm for CPP devices. Therefore the CIP devices have approximately 1000 Co grains whereas CPP has approx 10 Co grains along the tunneling path. Other than this, the CPP devices experience high electric field induced tunneling because of their smaller channel length (thickness). This tunneling is independent of the magnetic field and as a results leads to reduction in MR. The resistance for the CPP is lower than that of the CIP devices and it was found that sample 2G had a better CPP MR than the other structures indicating the fact that greater thickness of the granular film without the insert would improved MR and reduce high electric field induced tunneling in CPP devices.

5. A flux enhancement technique was proposed for CPP devices in order to improve their MR ratio. This was achieved by inserting soft magnetic Py layer between the granular film. The thickness of the Py films was varied between 1.5 nm and 15 nm and it was found that MR increased with Py thickness. This was attributed to the flux enhancement capability of Py layer especially at the edges. As the thickness of the Py layer was increased the edge to center field enhancement also improved and as a result, MR improved. So this structure was able to enhance the MR by countering the high electric field effect observed in the case of HfO_2 insert.

7.1 Future work

Hafnium oxide was chosen as the oxide insert to make sure that film was homogenous in terms of the oxide used. However it would be interesting to study the system by changing the central insert oxide e.g. SiO_2, Al_2O_3. It would be interesting to study the difference in properties because of the oxides used.

There have not been many devices showing the interplay of tunneling and scattering in the same device. There have been research study where MTJ based spin valves have been fabricated and tested. But the purpose was for current induced magnetization switching and not the study of interplay of tunneling and scattering [119,120].The research on metallic and insulating granular films have been done separately but there has been no article researching their combined structures. It is well known that insulating granular films are characterized by phenomenon of coulomb blockade and spin dependent tunneling, whereas metallic granular films such as Co-Cu Co-Al, Co-Ag, Co-Au are characterized by spin dependent scattering.The latter properties are very much similar to GMR devices such as spin valves. The metallic granular films can be thought of as layers in spin valves sputtered discontinuously. So it would be interesting to study the joint stack of FM-metallic and insulating granular film structures. The former's MR ratio depends on the scattering phenomenon, whereas the latter's MR ratio depends on tunneling.

Also, there are additional parameters which can be used in the measurement and characterization of granular films. The grains and the insulator in the granular film form a system of series and parallel capacitance. This can be altered by varying the FM volume fraction and the insulator. This capacitance changes with applied field and is referred to as magnetocapacitance [121–124] and could prove a useful tool for analysis of granular film.

Statement of Originality

The author claims the following aspects of this thesis to be original contribution to scientific knowledge.

Conferences

1. Regunathan, S.; Ng, V.; "Novel Granular Thin Film Device Structure", IEEE INTERMAG 2008, Madrid,Spain.

2. Regunathan, S.; Ng, V.; Chan, T.K. & Osipowicz, T.,"Effect of inserting an intermediate oxide layer in Co-HfO_2 granular films" , IEEE INTERMAG 2011, Taipei, Taiwan.

3. Regunathan, S.; Ng, V.; Chan, T.K. & Osipowicz T., "Effect of insertion of Py layer in Co-HfO_2 granular films", MMM 2011,Scottsdale, Arizona, USA

Journals

1. Regunathan, S.; Ng V.; Chadha, M.; Li, S.; Chantrell, R.; Chan, T.K. & Osipowicz, T. "Effect of volume fraction on interactions and grain size formation in Co-HfO_2 granular films" (To be submitted to Journal of Physics D)

2. Regunathan, S.; Ng V.; Chadha, M.; Li, S.; Chantrell, R.; Chan, T.K. & Osipowicz, T. "Effect of inserting an intermediate oxide layer in Co-HfO_2 granular films" (To be submitted to Journal of Applied Physics)

Appendix A

Dielectric constants and Band gap for different insulators

The following table shows the static dielectric constant (K) and experimental barrier for the various dielectrics (taken from ref. 124).

Material	Dielectric constant	Barrier Φ_R (eV)
Si_3N_4	7.8	2.1
Al_2O_3	9	2.8
Y_2O_3	15	2.3
ZrO_2	25	1.4
HfO_2	25	1.5
Ta_2O_5	26	1.1
La_2O_3	28	2.3
TiO_2	80	1.2

Table A.1: Dielectric constant and energy barrier for different dielectrics

References

[1] R. P. Feynman. *The character of physical law.* Cambridge: M.I.T. Press, 1967.

[2] R. Landauer. The future evolution of the computer. *Physics Today*, 23:22–28, 1970.

[3] M.N. Baibich, J.M. Broto, A. Fert, F. Ngguyen Van Dau, F. Petroff, P. Eitienne, G.Creuzet, A. Friederich, and J. Chazelas. Giant magnetoresistance of $(001)Fe/(001)Cr$ magnetic superlattices. *Phys. Rev. Lett.*, 61:2472, 1988.

[4] G. Binasch, P. Grunberg, F. Saurenbach, and W. Zinn. Enhanced magnetoresistance in layered magnetic structures with antiferromagnetic interlayer exchange. *Phys. Rev. B*, 39:4828–4830, 1989.

[5] P.M. Levy. *Giant magnetoresistance in magnetic layered and granular materials*, volume 47 of *Solid State Physics*, pages 367–462. Academic Press, Cambridge, 1994.

[6] S. Honda, T. Okada, M. Nawate, and M. Tokumoto. Tunneling giant magnetoresistance in heterogeneous $Fe - SiO_2$ granular films. *Phys. Rev. B*, 56:14566, 1997.

[7] N. Kobayashi, S. Ohnuma, S. Murakami, T. Masumoto, S. Mitani, and H. Fujimori. Enhancement of low-field-magnetoresistive response of tunnel-type

magnetoresistance in metal-nonmetal granular thin films. *Journal of Magnetism and Magnetic Materials*, 188:30, 1998.

[8] H. Fujimori, S. Mitani, and K. Takanashi. Giant magnetoresistance in insulating granular films and planar tunneling junctions. *Materials Science and Engineering*, A267:184, 1999.

[9] I. S. Beloborodov, A. V. Lopatin, V. M. Vinokur, and K. B. Efetov. Granular electronic systems. *Reviews of Modern Physics*, 79:469, 2007.

[10] Maung Kyaw Min Tun. Fabrication and characterization of co-sputtered $Co_xAl_yO_z$ granular thin films and devices. Master's thesis, Faculty of Engineering, National University of Singapore, 2004.

[11] Xavier Batlle and Amilcar Labarta. Finite-size effects in fine particles:magnetic and transport properties. *J. Phys. D: Appl. Phys.*, 35:R15, 2002.

[12] S Tumanski. *Thin Film Magnetoresistive Sensors*. Institute of Physics, 2001.

[13] K. Krishnan, A. Pakhomov, Y. Bao, P. Blomqvist, Y. Chun, M. Gonzales, K. Griffin, X. Ji, and B. Roberts. Nanomagnetism and spin electronics: materials, microstructure and novel properties. *Journal of Materials Science*, 41:793–815, 2006.

[14] S. Ohnuma, M. Ohnuma, H. Fujimori, and T. Masumoto. Metal-insulator type nano-granular soft magnetic thin films investigations on mechanism and applications. *Journal of Magnetism and Magnetic Materials*, 310:2503, 2007.

[15] K Yakushiji, S Mitani, F Ernult, K Takanashi, and H Fujimori. Spin-dependent tunneling and coulomb blockade in ferromagnetic nanoparticles. *Physics Reports*, 451:1–35, 2007.

[16] Leandro M. Socolovsky, Cristiano L. P. Oliveira, Juliano C. Denardin, Marcelo Knobel, and Iris L. Torriani. Nanostructure of granular $Co - SiO_2$ thin films modified by thermal treatment and its relationship with the giant hall effect. *Phys. Rev. B*, 72:184423, 2005.

[17] M. Julliere. Tunneling between ferromagnetic films. *Physics Letters*, 54A:225, 1975.

[18] Jian-Gang Zhu and Chando Park. Magnetic tunnel junctions. *Materials Today*, 9:36, 2006.

[19] Evgeny Y Tsymbal, Oleg N Mryasov, and Patrick R LeClair. Spin-dependent tunnelling in magnetic tunnel junctions. *J. Phys. Condens. Matter*, 15:R109, 2003.

[20] H. Grabert and M.H. Devoret., editors. *Single charge tunneling Coulomb blockade Phenomena in Nanostructures,*, volume 294 of *NATO ASI series B.* Plenum Press, 1992.

[21] J. I. Gittleman, Y.Goldstein, and S. Bozowski. Magnetic properties of granular nickel films. *Phys. Rev. B*, 5:3609–3621, 1972.

[22] P. Sheng, B. Abeles, and Y. Arie. Hopping conductivity in granular metals. *Phys. Rev. Lett.*, 31:44, 1973.

[23] S Barzilai, Y Goldstein, I balberg, and J S Helman. Magnetic and transport properties of granular cobalt films. *Phys. Rev. B*, 23:1809–1817, 1981.

[24] Ch. Morawe and H. Zabel. Structure and thermal stability of sputtered metal/oxide multilayers: The case of Co/Al_2O_3. *Journal of Applied Physics*, 77:1969–1976, 1995.

[25] J. Inoue and S.Maekawa. Theory of tunneling magnetoresistance in granular magnetic films. *Phys. Rev. B*, 53:R11927, 1996.

[26] J. S. Helman and B. Abeles. Tunneling of spin-polarized electrons and magnetoresistance in granular ni films. *Phys. Rev. Lett.*, 37:1429–1432, 1976.

[27] J.L. Maurice, J. Briatico, J. Carrey, Petroff, F. Schelp, and A. Vaures. Clusters obtained by sputter deposition of cobalt atoms on alumina. *Philosophical magazine A*, 7:2921–2934, 1999.

[28] Yukio Takeno and Yutaka Shimada. Fabrication of $Co - M - O(M = Ti, Al, Si)$ granular thin films with giant magnetoresistance by reactive deposition methodd. *Japan Journal of Applied Physics*, 41:1347–1348, 2002.

[29] S Mitani, H Fujimori, and S Ohnuma. Spin-dependent tunneling phenomena in insulating granular systems. *Journal of Magnetism and Magnetic materials*, 165:141–148, 1997.

[30] S. Mitani, S. Takahashi, K. Takanashi, K. Yakushiji, S. Maekawa, and H. Fujimori. Enhanced magnetoresistance in insulating granular systems:evidence for higher-order tunneling. *Phys. Rev. Lett.*, 81:2799, 1998.

[31] K. Yakushiji, S. Mitani, K. Takanashi, J.G. Ha, and H. Fujimori. Composition dependence of particle size distribution and giant magnetoresistance in co-al-o granular films. *Journal of Magnetism and Magnetic Materials*, 212:75, 2000.

[32] S. Mitani, K. Takanashi, K. Yakushiji, J. Chiba, and H. Fujimori. Study on spin dependent tunneling and coulomb blockade in granular systems with restricted tunneling paths. *Materials Science and Engineering B*, 84:120, 2001.

[33] K Yakushiji, S Mitani, K Takanashi, and H Fujimori. Tunnel magnetoresistance oscillations associated with coulomb staircases in insulating granular systems. *J. Phys. D: Appl. Phys.*, 35:2422, 2002.

[34] K. Yakushiji, S. Mitani, K. Takanashi, and H. Fujimori. Tunnel magnetoresistance oscillations in current perpendicular to plane geometry of coalo granular thin films. *J. Appl. Phys.*, 91:7038, 2002.

[35] K. Asami, S. Mitani, H. Fujimori, S. Ohnuma, and T. Masumoto. Unknown. *Surface and Interface Analysis*, 28:250–253, 1999.

[36] H. Fujimori, S. Mitani, and S. Ohnuma. Tunnel-type gmr in co-al-o insulated granular system - its oxygen-concentration dependence. *Journal of Magnetism and Magnetic Materials*, 156:311, 1996.

[37] G.N. Kakazei, P.P. Freitas, S. Cardoso, A.M.L. Lopes, M.M. Pereira de Azevedo, Yu.G. Pogorelov, and J.B. Sousa. Transport properties of discontinuous $Co_{80}Fe_{20}/Al_2O_3$ multilayers prepared by ion beam sputtering. *IEEE Transactions on Magnetics*, 35:2895, 1999.

[38] J.-G. Kim, J.G. Ha, J.H. Koh, S.M. Lim, and C.W. Kim. Annealing effect of particle size distribution and giant magnetoresistance in insulating granular films. *Thin Solid Films*, 515:2562, 2006.

[39] O. Chayka, L. Krausa, P. Lobotkac, V. Sechovskyb, T. Kocoureka, and M. Jelineka. High field magnetoresistance in $Co - Al - O$ nanogranular films. *Journal of Magnetism and Magnetic Materials*, 300:293, 2006.

[40] Ho Yin Kwong, Man Hon Wong, Yuen Wah Wong, and Kin Hung Wong. Magnetoresistivity of cobalt-ptfe granular composite film produced by pulsed laser deposition technique. *Rev.Adv.Mater.Sci.*, 15:215, 2007.

[41] C. J. Yang. Tunneling magnetoresistance of co granules in $AlN/Co/AlN$ type discontinuous films. *Journal of the Korean Physical Society*, 43:762, 2003.

[42] J. Varalda, W. A. Ortiz, A. J. A. de Oliveira, B. Vodungbo, Y.-L. Zheng, D. Demaille, and M. Marangolo. Tunnel magnetoresistance and coulomb blockade in a planar assembly of cobalt nanoclusters embedded in TiO_2. *J. Appl.Phys.*, 101:014318, 2007.

[43] J.C. Denardin, W.C. Nunes, and M. Knobel. Effects of magnetic interparticle coupling in the blocking temperature of granular *co* multilayers. *Physica B*, 384:290, 2006.

[44] A.L. Brandl, J.C. Denardina, L.M. Socolovskya, M. Knobel, and P. Allia. Study of anhysteretic magnetization loops of $Co_{0.35}(SiO_2)_{0.65}$ granular film. *Journal of Magnetism and Magnetic Materials*, 272-276:1526, 2004.

[45] A.L. Brandl, L.M. Socolovsky, J.C. Denardin, and M. Knobel. Effects of dipolar interactions on magnetic properties of granular solids. *Journal of Magnetism and Magnetic Materials*, 294:127, 2005.

[46] S. Honda, M. Hirata, and M. Ishimaru. Tunneling magnetoresistance of ultrathin $Co - SiO_2$ granular films with narrow current channels. *Journal of Magnetism and Magnetic Materials*, 290-291:1053, 2005.

[47] B. J. Hattink, M. Garcia del Muro, Z. Konstantinovic, X. Batlle, A. Labarta, and M. Varela. Tunneling magnetoresistance in $Co - ZrO_2$ granular thin films. *Phys. Rev. B*, 73:045418, 2006.

[48] G.N. Kakazei, Yu.G. Pogorelov, A.M.L. Lopes, M.A.S. da Silva, J.A.M. Santos, J.B. Sousa, S. Cardoso, P.P. Freitas, and E. Snoeck. Current-in-plane

transport in granular single layers and multilayers of cofe in Al_2O_3. *Journal of Magnetism and Magnetic Materials*, 266:62, 2003.

[49] G. N. Kakazei, Yu. G. Pogorelova, M. D. Costa, V. O. Golub, J. B. Sousa, P. P. Freitas, S. Cardoso, and P. E. Wigen. Interlayer dipolar interactions in multilayered granular films. *J. Appl. Phys.*, 97:10A723, 2005.

[50] J.A.M. Santos, G.N. Kakazei, J.B. Sousa, S. Cardoso, P.P. Freitas, Yu.G. Pogorelov, and E. Snoeck. Peculiar cip transport in $CoFe/Al_2O_3$ granular layered films across a micro-gap. *Journal of Magnetism and Magnetic Materials*, 242-245:485, 2002.

[51] K. Yakushiji, M. Matsuuraa, S. Mitani, K. Takanashi, and H. Fujimori. Coulomb staircase and tunnel magnetoresistance in nanowire-shaped granular films. *Journal of Magnetism and Magnetic Materials*, 303:e355, 2006.

[52] G. N. Kakazei, Yu. G. Pogorelov, A. M. L. Lopes, J. B. Sousa, S. Cardosoc, P. P. Freitas, M. M. Pereira de Azevedod, and E. Snoeck. Tunnel magnetoresistance and magnetic ordering in ion-beam sputtered $Co_{80}Fe_{20} - Al_2O_3$ discontinuous multilayers. *J. Appl.Phys.*, 90:4044, 2001.

[53] L. Kraus, O. Chayka, J. Tous, F. Fendrych, K.R. Pirota, M. Sicha, and L. Jastrabik. Magnetoresistance of fe-ta-o films prepared by rf plasma jet method. *Journal of Magnetism and Magnetic Materials*, 226-230:669, 2001.

[54] S. Sankar, D. Dender, J.A. Borchers, David J. Smith, R.W. Erwin, S.R. Kline, and A.E. Berkowitz. Magnetic correlations in non-percolated $Co - SiO_2$ granular films. *Journal of Magnetism and Magnetic Materials*, 221:1, 2000.

[55] F. Luis, J. M. Torres, L. M. Garcia, J. Bartolome, J. Stankiewicz, F. Petroff, F. Fettar, J.L. Maurice, and A. Vaures. Enhancement of the magnetic

anisotropy of nanometer-sized co clusters: Influence of the surface and of interparticle interactions. *Phys. Rev. B*, 65:094409, 2002.

[56] M. J. M. Pires, J. C. Denardin, E. C. da Silva, and M. Knobel. Ferromagnetic resonance studies in granular $Co - SiO_2$ thin films. *J. Appl.Phys.*, 99:063908, 2006.

[57] T. Furubayashi and I. Nakatani. Giant magnetoresistance in granular $Fe - MgF_2$. *J. Appl. Phys.*, 79:6258, 1996.

[58] M. Ohnuma, K. Hono, E. Abe, H. Onodera, and S. Mitani. Microstructure of co-al- granular thin films. *J. Appl. Phys*, 82:5646, 1997.

[59] T. Zhu and Y. J. Wang. Enhanced tunneling magnetoresistance of $Fe-Al_2O_3$ granular films in the coulomb blockade regime. *Phys. Rev. B*, 60:11918, 1999.

[60] J.G. Lin, C.K. Hsu, R.S. Zhai, and T.J. Chuang. Physical and chemical properties of nanostructured coo-alox granular films. *Journal of Physics and Chemistry of Solids*, 65:1333, 2004.

[61] I. N. Krivorotov, N. C. Emley, J. C. Sankey, S. I. Kiselev, D. C. Ralph, and R. A.Buhrman. Time-domain measurements of nanomagnet dynamics driven by spin-transfer torques,. *Science*, 307:228, 2005.

[62] R. Carey, D. M. Newman, and P. Bouvier. Oxidation effects in granular cobalt films. *IEEE Transactions on Magnetics*, 33:3256, 1997.

[63] D.V. Berkov and S.V. Meshkov. Hysteresis phenomena in ensemble of dipole-interacting particles without intrinsic anisotropie. *IEEE Transactions on Magnetics*, 26 (5):1804, 1990.

[64] P. Allia, M. Coisson, P. Tiberto, F. Vinai, and M. Knobel. Magnetic hysteresis in granular $CuCo$ alloys. *J. Appl.Phys.*, 85:4343, 1999.

[65] D. Kechrakos and K. N. Trohidou. Dipolar interaction effects in the spin-dependent transport in nanoparticle systems. *phys. stat. sol. (a)*, 189:277–280, 2002.

[66] D. Kechrakos and K.N. Trohidou. Spin correlations and electronic transport in magnetic nanoclusters. *Physica B*, 318:360–364, 2002.

[67] Zhongquan Mao, Dihu Chen, and Zhenhui He. Role of interparticle coupling on the tunneling magnetoresistance of granular films in interacting superparamagnetic system. *Journal of Magnetism and Magnetic Materials*, 320:642–645, 2008.

[68] Y Fukumoto, H Jubota, Y Ando, and T Miyazaki. Enhancement of tunnel magnetoresistance effect on junction with co cluster layers in coulomb blockade regime. *Japan Journal of Applied Physics*, 38:L932, 1999.

[69] H. Sukegawa, S. Nakamura, A. Hirohata, N. Tezuka, and K. Inomata. Significant magnetoresistance enhancement due to a cotunneling process in a double tunnel junction with single discontinuous ferromagnetic layer insertion. *Phys. Rev. Lett.*, 94:068304, 2005.

[70] Ludwig Reimer. *Transmission Electron Microscopy: Physics of Image Formation and Microanalysis.* Springer Series in Optical Sciences, 1997.

[71] B. D. Williams and C. B. Carter. *Transmission electron microscopy: a textbook for materials science.* Springer - Newyork, 1996.

[72] B. Yao, Tik Sun, A. Warren, H. Heinrich, K. Barmak, and K. R. Coffey. High contrast hollow-cone dark field transmission electron microscopy for nanocrystalline grain size quantification. *Micron*, 41:177, 2010.

[73] J. C. Denardin, A. L. Brandl, M. Knobel, P. Panissod, A. B. Pakhomov, H. Liu, and X. X. Zhang. Thermoremanence and zero-field-cooled/field-cooled magnetization study of $Co_x(SiO_2)_{1-x}$ granular films. *Phys. Rev. B*, 65:064422, 2002.

[74] Megha Chadha. *Study of* $Co - HfO_2$ *Granular Films Deposited by Sequential Sputtering*. PhD thesis, Department of ECE, National University of Singapore, 2012.

[75] S. Honda, M. Nawate, T. Umemoto, S. Mitsudo, S. Mitani, H. Fujimori, and M. Motokawa. Bias voltage dependence of tunneling giant magnetoresistance in heterogeneous $Fe - SiO_2$ granular films. *IEEE Transactions on Magnetics*, 35:2955–2957, 1999.

[76] O. Glatter and O. Kratky, editors. *Small-angle X-ray Scattering*. Academic Press, London, 1982.

[77] W. C. Nunes, L. M. Socolovsky, J. C. Denardin, F. Cebollada, A. L. Brandl, and M. Knobel. Role of magnetic interparticle coupling on the field dependence of the superparamagnetic relaxation time. *Phys. Rev. B*, 72:212413, 2005.

[78] M. Ohnuma, K. Honol, H. Onoderal, S. Mitani, J.G. Ha, and H. Fujimori. Microstructure change in $Co_{46}Al_{19}O_{35}$ granular thin films by annealing. *Nanostruct. Mater.*, 12:573, 1999.

[79] H. Mamiya, M. Ohnuma, I. Nakatani, and T. Furubayashim. Extraction of blocking temperature distribution from zero-field-cooled and field-cooled magnetization curves. *IEEE Transactions on Magnetics*, 41:3394 – 3396, 2005.

[80] S Regunathan and V Ng. Novel granular thin film device structure. In *INTERMAG(Madrid,Spain)*. IEEE, IEEE Intermag, 2008.

[81] C. L. Platt, B. Dieny, and A. E. Berkowitz. Spin-dependent tunneling in HfO_2 tunnel junctions. *Appl. Phys. Lett.*, 69:2291, 1996.

[82] R. W. Chantrell, N. Walmsley, J. Gore, and M. Maylin. Calculations of the susceptibility of interacting superparamagnetic particles. *Phys. Rev. B*, 63.:024410, 2000.

[83] Y. H. Huang, J. H. Hsu, and J. W. Chen. Thickness dependence of tunneling magneto-resistance effect in granular $Fe - Al_2O_3$ films. *IEEE Transactions on Magnetics*, 33:3556, 1997.

[84] P Allia, M Coisson, Paola Tiberto, Franco Vinai, Marcelo Knobel, M. A. Novak, , and W. C. Nunes. Granular $Cu - Co$ alloys as interacting superparamagnets. *Phys. Rev. B*, 64:144420, 2001.

[85] W. W. Ann Alvin. Fabrication and characterization of granular nanomagnets. Master's thesis, National University of Singapore, 2004.

[86] Masaoki Oku and Yoshito Sato. In-situ x-ray photoelectron spectroscopic study of the reversible phase transition between CoO and Co_3O_4 in oxygen of 10^{-3} pa. *Applied Surface Science*, 55:37 – 41, 1992.

[87] S. Suzer, S. Sayan, M. M. Banaszak Holl, E. Garfunkel, Z. Hussain, and N. M. Hamdan. Soft x-ray photoemission studies of hf oxidation. *Journal of Vacuum Science Technology*, 21:106–109, January 2003.

[88] Nam H. Kim, Jordan Peck, and Jian-Qing Wang. Anomalous magnetic nanostructural evolution in annealed cuco granular thin films. *Appl. Phys. Lett.*, 88:222510, 2006.

[89] *The International Centre for Diffraction Data (ICDD). Newtown Square, PA. International Centre for Diffraction Data (2002).*

[90] Richard C. Jaeger. *Introduction to Microelectronic Fabrication: Volume 5 of Modular Series on Solid State Devices*. Prentice Hall, 2002.

[91] Jaques Perriere. Rutherford backscattering spectrometry. *Vacuum*, 37:429–432, 1987.

[92] *http://home.rzg.mpg.de/ mam/Version6.html - SIMNRA is a Microsoft Windows program for the simulation of backscattering spectra for ion beam analysis with MeV ions.*

[93] *Oxford Instruments- CCC1200 and CCC1204 Operator Handbook.*

[94] S. Mitani, S. Takahashi, K. Takanashi, K. Yakushiji, S. Maekawa, and H. Fujimori. Enhanced magnetoresistance in insulating granular systems: Evidence for higher-order tunneling. *Physical Review Letters*, 81(13):2799–2802, 1998. ISI Document Delivery No.: 123PJ Times Cited: 199 Cited Reference Count: 25 American physical soc College pk.

[95] R. W. Chantrell and E. P. Wohlfarth. Dynamic and static properties of interacting fine ferromagnetic particles. *Journal of Magnetism and Magnetic Materials*, 40:1–11, 1983.

[96] Andre RASSAT. Magnetic properties of nitroxide multiradicals. *Pure & Appl. Chem.*, 62:223–227, 1990.

[97] P. Allia, M. Coisson, J. Moya, P. Tiberto, and F. Vinai. Granular metallic systems as interacting superparamagnets: anhysteretic magnetization and hysteresis loops. *Journal of Magnetism and Magnetic Materials*, 254-255(0):143–148, 2003.

[98] M Chadha and V Ng. Evidence of interactions in $Co - HfO_2$ granular films. *Journal of Physics: Condensed Matter*, 24(12):126001, 2012.

[99] S Regunathan, Ng Vivian, M. Chadha, Shi Li, R. Chantrell, Chan T.K, and T. Osipowicz. Effect of volume fraction on interactions and grain size formation in $Co - HfO_2$ granular films(to be submitted). April 2012.

[100] R. W. Chantrell, N. Walmsley, J. Gore, and M. Maylin. Calculations of the susceptibility of interacting superparamagnetic particles. *Physical Review B*, 63, 2001.

[101] P.P. Freitas, A.A. Gomes, T.R. McGuire, and T.S. Plaskett. Anisotropic magnetoresistance in co films. *Journal of Magnetism and Magnetic Materials*, 83:113, 1990.

[102] F. Fettar, S.F. Lee, F. Petroff, A. Vaures, P. Holody, L. F. Schelp, and A. Fert. Temperature and voltage dependence of the resistance and magnetoresistance in discontinuous double tunnel junctions. *Phys. Rev. B*, 65:174415, 2002.

[103] J.C. Denardin, M. Knobel, L.S. Dorneles, and L.F. Schelp. Structural, magnetic and transport properties of discontinuous granular multi-layers. *Journal of Magnetism and Magnetic Materials*, 294(2):206 – 212, 2005.

[104] Michael Ziese. Spin hopping in a discontinuous $La_0.7Ca_0.3MnO_3$ film. *Appl. Phys. Lett.*, 80:2144–2146, 2002.

[105] N. F. Mott. Conduction in non-crystalline materials. *Phil. Mag.*, 19:835, 1969.

[106] F. Fettar, S.F. Lee, F. Petroff, A. Vaures, P. Holody, L. F. Schelp, and A. Fert. Temperature and voltage dependence of the resistance and magnetoresistance in discontinuous double tunnel junctions. *Phys. Rev. B*, 65:174415, 2002.

[107] Li Xi, Zong-Zhi Zhang, Jian-Bo Wang, Cheng-Xian Li, Fa-Shen Li, Shi-Hui Ge, Tao Xu, and Sheng-Rong Yang. The influence of microstructure on tunnelling magnetoresistance in $Fe - SiO_2$ granular films. *J. Phys. D: Appl. Phys.*, 33:621, 2000.

[108] F. Guinea. Spin-flip scattering in magnetic junctions. *Phys. Rev. B*, 58:9212–9216, Oct 1998.

[109] G. J. Strijkers, H. J. M. Swagten, B. Rulkens, R. H. J. N. Bitter, W. J. M. de Jonge, P. J. H. Bloemen, and K. M. Schep. Temperature dependence of the resistivity and tunneling magnetoresistance of sputtered fehf(si)o cermet films. *Journal of Applied Physics*, 84(5):2749–2753, 1998.

[110] Jing Shi, Kevin Pettit, E. Kita, S. S. P. Parkin, R. Nakatani, and M. B. Salamon. Field-dependent thermoelectric power and thermal conductivity in multilayered and granular giant magnetoresistive systems. *Phys. Rev. B*, 54:15273–15283, 1996.

[111] Li Shi. Simulation of magnetic granular films and structures (final year project), 2011.

[112] H.A Knudsen and S. Fazekas. Robust algorithm for random resistor networks using hierarchical domain structure. *Journal of Computational Physics*, 211:700, 2006.

[113] Minyao Zhou, Ping Sheng, L. Chen, and B. Abeles. Numerical simulation of hopping conductivity in granular metal films. *Philosophical Magazine Part B,*, 65:867–871, 1992.

[114] C.H. Lin and G.Y. Wu. Hopping conduction in granular metals. *Physica B*, 279:341–346, 2000.

[115] Li-Ping Zhou, Sheng Ju, and Zhen-Ya Likharev. Effect of network on tunneling magnetoresistance in a half-metallic granular system. *J. Appl.Phys.*, 95:8041, 2004.

[116] J. Pan, T. W. Jing, and S. M. Lindsay. Tunneling barriers in electrochemical scanning tunneling microscopy. *The Journal of Physical Chemistry*, 98:4205, 1994.

[117] *http://www.femm.info/wiki/HomePage*.

[118] Jijun Yang, Youlan Huang, and Kewei Xu. Effect of substrate on surface morphology evolution of cu thin films deposited by magnetron sputtering. *Surface & Coatings Technology*, 201:5574, 2007.

[119] Hao Meng and Jian-Ping Wang. Spin transfer effect in magnetic tunnel junction with a nano-current-channel layer in free layer. *IEEE Transactions on Magnetics*, 41:2612 – 2614, 2005.

[120] G. D. Fuchs, N. C. Emley, I. N. Krivorotov, P. M. Braganca, E. M. Ryan, S. I. Kiselev, J. C. Sankey, D. C. Ralph, and R. A. Buhrman. Spin-transfer effects in nanoscale magnetic tunnel junctions. *Appl. Phys. Lett.*, 85:1205, 2004.

[121] Ryan P. Rairigh, Guneeta Singh Bhalla, Sefaatin Tongay, Tara Dhakal, Amlan Biswas, and Arthur F. Hebard. Colossal magnetocapacitance and scale-

invariant dielectric response in phase-separated manganites. *Nature Physics*, 3:551, 2007.

[122] G. Catalana. Magnetocapacitance without magnetoelectric coupling. *Appl. Phys. Lett.*, 88:102902, 2006.

[123] T. Kimura, S. Kawamoto, I. Yamada, M. Azuma, M. Takano, and Y. Tokura. Magnetocapacitance effect in multiferroic $BiMnO_3$. *Phys. Rev. B*, 67:180401, 2003.

[124] Hei Wong and Hiroshi Iwai. Modeling and characterization of direct-tunneling current in dual-layer ultrathin-gate dielectric films. *J. Vac. Sci. Technol. B*, 24:1785, 2006.